



40<sup>th</sup> Annual VFS Student Design Competition

# High-Speed Vertical Takeoff and Landing (HSVTOL) Aircraft

*Sponsored by Sikorsky*



UNIVERSITY OF  
MARYLAND

Alfred Gessow Rotorcraft Center  
Department of Aerospace Engineering  
University of Maryland  
College Park, MD 20742 U.S.A.



Alfred Gessow Rotorcraft Center  
Department of Aerospace Engineering  
University of Maryland  
College Park, MD 20742

---

Nathan O'Brien  
*Graduate Student (Team Lead)*  
nobrien2@umd.edu

---

Brendan Egan  
*Graduate Student/(V-22 Pilot)*  
began91@umd.edu

---

Noam Kaplan  
*Graduate Student*  
nkaplan1@umd.edu

---

Nicholas Paternostro  
*Graduate Student*  
npatern@umd.edu

---

Xavier Delgado  
*Graduate Student*  
delgadx2@umd.edu

---

Ray-Shimry Garatsa  
*Graduate Student*  
rgaratsa@umd.edu

---

Dr. Inderjit Chopra  
*Faculty Advisor*  
chopra@umd.edu

---

Dr. Vengalatore Nagaraj  
*Faculty Advisor*  
vnagaraj@umd.edu

---

Dr. Anubhav Datta  
*Faculty Advisor*  
datta@umd.edu

---

Academic Course:  
ENAE634: Helicopter Design (3 credits)

## ACKNOWLEDGEMENTS

The design team wishes to acknowledge the following people for their invaluable discussion, guidance, and support throughout the course of this project.

### **Industry Professionals**

*Jeff Nissen* — Senior Manager Advanced Technology at Bell Flight

*Dr. Brent Mills* — Aerospace Engineer at Army Research Lab

*Dr. Seyhan Gul* — Aerospace Engineer at U.S. Army Moffett Field

### **University of Maryland Faculty**

*Prof. James D. Baeder* — Samuel Langley Professor, Department of Aerospace Engineering

*Prof. Umberto Saetti* — Assistant Professor, Department of Aerospace Engineering

*Dr. Mrinalgouda Patil* — Postdoctoral Research Associate, Department of Aerospace Engineering

*Dr. Bumseok Lee* — Postdoctoral Research Associate, Department of Aerospace Engineering

### **Alfred Gessow Rotocraft Research Center Graduate Students**

Spencer Fishman (US Navy Pilot)

Akinola Akinwale

Eric Greenbaum

Matt Arace

Paulo Arias

Dilhara Jayasundara

### **Logo Artist**

Maria L. Delgado



**Alfred Gessow Rotorcraft Center**  
Department of Aerospace Engineering  
University of Maryland  
College Park, MD 20742 U.S.A.

To the Vertical Flight Society:

The members of the University of Maryland Graduate Student Design Team hereby grant VFS full permission to distribute the enclosed Executive Summary and Final Proposal for the 40th Annual Design Competition as they see fit.

Thank you,  
The UMD Graduate Design Team

# Contents

<b>1</b>	<b>Introduction</b>	<b>1</b>
<b>2</b>	<b>Concept of Operations</b>	<b>2</b>
<b>3</b>	<b>Configuration Selection</b>	<b>4</b>
3.1	Selection Methodology . . . . .	4
3.2	Mission Capability Analysis . . . . .	5
3.2.1	Vehicle Considerations . . . . .	5
3.2.2	Vehicles Considered Incapable of meeting RFP requirements . . . . .	5
3.2.3	Capable of meeting RFP requirements, with major complexities . . . . .	6
3.2.4	Capable of achieving the RFP, with moderate complexities . . . . .	7
3.3	Key Design Drivers . . . . .	9
3.3.1	Analytic Hierarchy Process (AHP) . . . . .	10
3.3.2	Tiltrotor Vs. Tiltwing . . . . .	12
3.3.3	Two-speed Tiltrotor Vs. Variable Diameter Tiltrotor . . . . .	12
<b>4</b>	<b>Preliminary Vehicle Sizing and Final Configuration Selection</b>	<b>13</b>
4.1	Sizing Methodology . . . . .	13
4.1.1	Mission Profile . . . . .	13
4.1.2	Sizing Algorithm . . . . .	14
4.2	Initial Sizing Comparison . . . . .	16
<b>5</b>	<b>Detailed Rotor and Vehicle Sizing</b>	<b>18</b>
5.1	Refined Sizing Methodology . . . . .	18
5.2	Qualitative Analysis . . . . .	18
5.2.1	Blade Loading . . . . .	18
5.2.2	RPM Reduction . . . . .	19
5.2.3	Blade Airfoil . . . . .	20
5.2.4	Blade Twist Setting . . . . .	23
5.2.5	Disk Loading . . . . .	24
5.3	Aerodynamic Trade Studies . . . . .	25
5.3.1	Hover and Cruise Tip Speeds . . . . .	25
5.3.2	Blade Airfoil Transition . . . . .	26
5.3.3	Blade Sweep . . . . .	27
5.3.4	Blade Taper . . . . .	27
5.3.5	Blade Twist . . . . .	28
5.4	Rotor Sizing . . . . .	29
5.5	Wing Sizing . . . . .	29
5.6	Powerplant Sizing . . . . .	30
5.7	Final Tabulated Design Parameters . . . . .	30
<b>6</b>	<b>Blade Structural Design</b>	<b>30</b>
6.1	Blade Internal Structure . . . . .	30
6.2	Rotor Blade Sectional Properties . . . . .	33
6.3	Blade Manufacturing . . . . .	34
6.4	Aeroelastic Stability Analysis . . . . .	34
6.4.1	Ground Resonance . . . . .	35
6.4.2	Whirl Flutter . . . . .	36

6.5	3-D Stress Analysis . . . . .	37
<b>7</b>	<b>Hub Design</b>	<b>38</b>
7.1	Hub Selection . . . . .	38
7.2	Hub Assembly . . . . .	38
7.3	Swashplate Design . . . . .	39
<b>8</b>	<b>Wing and Pylon Design</b>	<b>40</b>
8.1	Wing Aerodynamic Design . . . . .	40
8.1.1	Lift Requirements . . . . .	40
8.1.2	Wing Airfoil Selection . . . . .	41
8.1.3	Wing Geometric Parameters . . . . .	41
8.2	Wing Structural Design . . . . .	43
8.2.1	Wing Structural Design . . . . .	43
8.2.2	Wing Jump Take-off Loads . . . . .	44
8.2.3	Wing Structure . . . . .	44
8.2.4	Wing Material Selection . . . . .	44
8.2.5	Wing Fuselage Connection . . . . .	45
8.3	Pylon Structure . . . . .	46
<b>9</b>	<b>Airframe Design</b>	<b>47</b>
9.1	Fuselage Design . . . . .	47
9.2	Landing Gear . . . . .	49
9.2.1	Configuration Trade Study . . . . .	49
9.2.2	Tire Selection . . . . .	49
9.2.3	Modeling Landing Gear Dynamics . . . . .	49
9.2.4	Strut Sizing . . . . .	50
9.2.5	Gear Position and Packaging . . . . .	51
9.3	Cargo Bay and Ramp . . . . .	51
<b>10</b>	<b>Transmission Design</b>	<b>52</b>
10.1	Investigation of Two-Speed Transmissions . . . . .	52
10.2	Selection of a Two-Speed Transmission . . . . .	54
10.3	Placement of Powertrain Components . . . . .	55
10.4	Design of Transmission Components . . . . .	56
10.5	Novel Terp Two-Speed Transmission Clutch System . . . . .	57
<b>11</b>	<b>Propulsion System</b>	<b>60</b>
11.1	Propulsion Selection Overview . . . . .	60
11.2	Turbofan & Turboshaft Sizing . . . . .	60
11.3	Engine Material Selection . . . . .	61
11.4	Engine Performance Data . . . . .	62
<b>12</b>	<b>Vehicle Aerodynamic Design</b>	<b>62</b>
12.1	Fuselage . . . . .	62
12.2	Rotor Pylon . . . . .	66
12.3	Cruise Operating Conditions . . . . .	67
<b>13</b>	<b>Vehicle Performance</b>	<b>68</b>
13.1	High-Fidelity Drag Estimation . . . . .	68

13.2	Vehicle Download . . . . .	69
13.3	Hover Performance . . . . .	70
13.4	Performance in Airplane Mode . . . . .	72
13.5	Conversion Sequence . . . . .	77
13.6	Flight Envelope . . . . .	79
13.7	Mission Performance Data . . . . .	79
<b>14</b>	<b>Weight and Balance</b>	<b>81</b>
14.1	Influence of CG Location . . . . .	81
<b>15</b>	<b>Flight Dynamics and Controls</b>	<b>82</b>
15.1	Control Strategy Overview . . . . .	82
15.2	Cockpit Controls . . . . .	82
15.3	Control Mixing . . . . .	84
15.4	Aircraft Stability . . . . .	85
15.4.1	Unaugmented Stability . . . . .	85
15.4.2	Augmented Stability . . . . .	86
15.4.3	Stability Augmentation System - Control Loop . . . . .	87
15.4.4	Automatic Flight Control System - Navigation Loop . . . . .	88
15.4.5	Engine and Rotor Governing . . . . .	89
15.5	Flight Simulation . . . . .	89
<b>16</b>	<b>Avionics System</b>	<b>90</b>
16.1	Guidance, Navigation, and Control . . . . .	91
16.1.1	Navigation . . . . .	91
16.1.2	Landing Zone Situational Awareness, Guidance, and Evaluation . . . . .	92
16.1.3	Cockpit Interface . . . . .	93
16.1.4	Guidance and Control . . . . .	93
16.2	Communication . . . . .	94
16.3	Mission Management . . . . .	94
16.4	Health and Usage Monitoring System . . . . .	94
<b>17</b>	<b>Manufacturing &amp; Cost Analysis</b>	<b>95</b>
17.1	Aircraft Purchase Price . . . . .	95
17.2	Maintenance Cost . . . . .	95
17.3	Operational Cost . . . . .	95
<b>18</b>	<b>Multi-Mission Capabilities</b>	<b>95</b>
18.1	Non-Combat Transport and Logistics . . . . .	96
18.2	Search and Rescue . . . . .	96
18.3	Airborne Command and Control . . . . .	97
<b>19</b>	<b>Summary</b>	<b>97</b>

# List of Figures

1.1	Tested VTOL Configurations Grouped by Top Speeds . . . . .	1
4.1	Mission Profile . . . . .	14
4.2	Flowchart for the configuration sizing procedure . . . . .	15
4.3	Predicted Gross Take-off Weight versus propulsive efficiency for folding and jet-assist tiltrotor	16
4.4	Turboshaft and turbofan weights required to overcome drag of a vehicle with a flat plate area of 11.5 $ft^2$ . . . . .	17
5.1	Vehicle Sizing and Aerodynamic Design Process . . . . .	18
5.2	Effect of blade loading on hover and cruise performance . . . . .	19
5.3	L/D vs velocity for modified XV-15 with test data (conceptual study) . . . . .	19
5.4	Mach and Re Number variation with span and tip speed . . . . .	20
5.6	In-house CFD predicted performance of airfoils in the transition region . . . . .	22
5.5	In-house UMD 16005 Airfoil . . . . .	22
5.7	In-house CFD predicted Characteristics of best aerodynamic performance airfoils . . . . .	23
5.8	In-house CFD predicted Characteristics of best aerodynamic performance airfoils . . . . .	23
5.9	Inflow angle ( $\phi$ ) versus radial station ( $r/R$ ). Left shows effect of varying inflow ratio and right shows twist profile achieved . . . . .	24
5.10	Gross takeoff weight [lb] variation with hover and cruise tip speeds . . . . .	25
5.11	Variation of airfoil transition locations with efficiency and gross weight . . . . .	26
5.12	Outboard airfoil transition (7% - 5% t/c) . . . . .	26
5.13	Scimitar sweep profile characteristics effect on vehicle design . . . . .	27
5.14	Linear taper characteristics effect on vehicle design . . . . .	28
5.15	Blade bilinear twist selection . . . . .	28
5.16	Rotor parameter selection . . . . .	29
5.17	Wing parameter selection . . . . .	29
5.18	Cruise propulsive efficiency variation with turboshaft power installed. Colors indicate the resulting design GTOW. . . . .	29
5.19	Final blade aerodynamics design . . . . .	30
6.1	Blade internal anatomy with materials . . . . .	32
6.2	Rotor Blade Sectional Properties . . . . .	33
6.3	Fan plots showing first five rotor frequencies at hover and cruise RPM . . . . .	34
6.4	Flap-lag flutter boundaries at $\theta_{tw} = -21^\circ$ with increasing blade loading . . . . .	35
6.5	Flap-lag and pitch-flap stability margins . . . . .	35
6.6	Whirl flutter stability analysis of coupled modes at 2000 ft . . . . .	36
6.7	Whirl flutter stability analysis of coupled modes at 27,000 ft . . . . .	36
6.8	Axial stress distribution of <i>Arion</i> blade in hover, $C_T/\sigma = 0.12$ . . . . .	37
7.1	Hub assembly . . . . .	39
7.2	In-depth component details of the hub and swashplate assemblies . . . . .	40
8.1	Airfoil Performance Curves calculated using in-house 2D CFD solver . . . . .	41
8.2	$C_d$ vs $C_l$ at cruise speed with $11^\circ$ sweep . . . . .	42
8.3	Stall Speed Varying with Flap Deflection at Different Altitudes and ISA conditions . . . . .	42
8.4	Main wing pressure distribution with wing-tip vortices and flowlines at $-0.4^\circ$ and $5^\circ$ AOA . . . . .	43
8.5	The primary load-bearing structure of the wing (shown without flaps / flaperons) . . . . .	45
8.6	Finite element analysis of the wing-fuselage connection . . . . .	45
8.7	Pylon Interior shown in Axial Flight . . . . .	46
9.1	Semi-monocoque architecture for metal and composite primary airframe structure showing the basic load-bearing elements. . . . .	47
9.2	Geodesic fuselage geometry and design . . . . .	48

9.3	Finite element displacement for each of the fuselage designs. From left to right the conventional aluminum fuselage, conventional composite fuselage and geodesic fuselage . . . . .	48
9.4	Landing Gear Analysis . . . . .	50
9.5	Rear cargo ramp open for loading cargo, vehicles, or personnel . . . . .	52
10.1	Simplified diagram of the NASA offset compound gear in hover mode. . . . .	53
10.2	Simplified diagram of the NASA offset compound gear in cruise mode. . . . .	54
10.3	Final powertrain layout. . . . .	55
10.4	Transmission Drawings . . . . .	58
10.5	Internal view of the Terp Two-Speed Transmission clutch system when <i>Arion</i> is in hover mode. . . . .	58
10.6	Internal view of the Terp Two-speed Transmission clutch system when <i>Arion</i> is in cruise mode. . . . .	59
11.1	Turbofan engine sizing . . . . .	61
11.2	Turboshaft engine sizing . . . . .	61
11.3	Fuel flow rate for turbofan and turboshaft engine vs. throttle setting . . . . .	62
12.1	Fuselage Version 1.0 Pressure Distribution . . . . .	63
12.2	Initial Ramp Design . . . . .	64
12.3	Improved Ramp Design . . . . .	64
12.4	Pressure and Skin Friction Contour of Fuselage Version 1.0 . . . . .	64
12.5	Comparing Pressure and Skin Friction Drag for Different Nose Geometries . . . . .	65
12.6	Comparing Pressure Distribution for Different Rotor Pylon Configurations . . . . .	66
12.7	Fuselage pressure distribution and flowlines for different body pitch angles . . . . .	67
12.8	Fuselage skin friction coefficient distribution in ramp region for different body pitch angles . . . . .	67
13.1	Hover download as a percentage of gross weight for various flap configurations in hover . . . . .	70
13.2	HOGE performance curves at 2000 ft MSL and 85°F. . . . .	71
13.3	HOGE power required (blue) and power available (red) for various ISA conditions . . . . .	71
13.4	Maximum HOGE altitude vs. GTOW for various of ISA conditions . . . . .	72
13.6	$L/D$ vs. Velocity. ISA conditions within RFP requirement of 20k ft (6,096 m) or greater (blue), 10k ft (3,048 m), ISA (black), and 2k/85°F (red) are displayed. Flight test data from XV15 along with the analytical model, and LCTR analytical predictions are also shown [1] . . . . .	73
13.5	Turbofan Thrust 450 kt cruise. . . . .	73
13.7	$\eta_p$ versus propeller advance ratio . . . . .	74
13.8	Range Performance of <i>Arion</i> . . . . .	74
13.9	Endurance Performance of <i>Arion</i> . . . . .	75
13.10	Climb Performance of <i>Arion</i> . . . . .	76
13.11	Descent Performance of <i>Arion</i> . . . . .	76
13.12	Power profile versus airspeed . . . . .	77
13.13	Rotor Lift-to-drag ratio ( $L/D_e$ ) variation with advance ratio. Flight beyond an advance ratio $\mu = 0.275$ is restricted by the VMS to prevent shocks over the rotor blade . . . . .	78
13.14	Conversion corridor for the <i>Arion</i> with full flaps and without flaps . . . . .	78
13.15	Full operation envelope . . . . .	80
14.1	Allowable range of payload CG relative to the cargo bay center based on CG analysis with zero fuel weight. . . . .	81
14.2	Aircraft CG variation within the allowable range due to payload weight (left is 5,000 lb and right is 2,500 lb), payload CG location within cargo bay (sub-axis abscissa), and aircraft fuel level (sub-axis ordinate). . . . .	82
15.1	Cockpit controls including active side stick, split-power thrust control lever, and foot pedals. . . . .	84

15.2 Unaugmented Hover Stability Modes. Red symbols are the longitudinal modes, and blue symbols are the lateral-directional modes. Squares reflect CG shifting forward up to 7.5 inches (19 cm) from the rotor shaft. Circles reflect the CG shifting aft up to 20 inches (51 cm) from the rotor shaft. . . . . 86

15.3 Hover Stability Modes with Pitch, Roll, and Yaw Rate Electronic Feedback Damping. Red symbols are the longitudinal modes, and blue symbols are the lateral-directional modes. Squares reflect CG shifting forward up to 7.5 inches (19 cm) from the rotor shaft. Circles reflect the CG shifting aft up to 20 inches (51 cm) from the rotor shaft. . . . . 87

15.4 Example of TRC DI Inversion for Lateral Stick Inputs in a Hover . . . . . 90

16.1 Avionics architecture of *Arion* . . . . . 91

16.2 Cockpit Instrument Panel Overview . . . . . 93

## List of Tables

3.1	Analytic Hierarchy Process (AHP) Matrix . . . . .	11
3.2	Pugh Martrix . . . . .	13
4.1	Parameters for Jet-Assist vs. Folding Tiltrotor Sizing Comparison . . . . .	16
5.1	Airfoils considered for Rotor Blade . . . . .	21
5.2	Design Parameters . . . . .	31
6.1	Hover RPM natural frequencies . . . . .	34
6.2	Cruise RPM natural frequencies . . . . .	34
9.1	Table summarizing the landing gear configuration study. . . . .	49
9.2	Various tires considered for tire selection. <i>*Chosen tire.</i> . . . .	50
9.3	Summary of Landing Gear Sizing . . . . .	51
10.1	Summary of key transmission characteristics in hover. . . . .	57
10.2	Summary of key transmission characteristics in cruise. . . . .	58
12.1	Fuselage Drag . . . . .	66
12.2	Rotor Pylon Drag . . . . .	66
12.3	Fuselage Angle of Incidence Comparison . . . . .	68
13.1	Drag breakdown . . . . .	69
13.2	Vertical Drag breakdown . . . . .	70
13.3	<i>Arion</i> V-Speeds . . . . .	77
13.4	Edgewise Performance Equivalent Rotor Drag Buildup for a Single Rotor . . . . .	79
13.5	Mission Performance Data . . . . .	80
14.1	Aircraft center of gravity with measurements made from the center of the nose. . . . .	83
15.1	Unaugmented Control Mixing Strategy . . . . .	84

<b>RFP Deliverable</b>	<b>Source</b>	<b>Section/Figure</b>
Trade Studies	RFP 2.4.1	4, 5
Vehicle Description	RFP 2.4.2	2
Propulsion system Data Fuel Flow vs. Power Setting	RFP 2.4.3	11 11.3
Hover Performance Data Power required vs. GTOW FM vs. GTOW Download Factor Calculation	RFP 2.4.4	13.3 13.2(b) 13.2(a) 13.1
Forward Flight Performance Data Power required vs. Airspeed	RFP 2.4.5	13.4 13.12
Mission Performance Data	RFP 2.4.6	Tbl. 13.5
Air Vehicle and Subsystem Drawing General Arrangement Inboard Profile Structural Arrangement Subsystem Functional Schematics	RFP 2.4.7	Provided Throughout
Aerodynamic Data: Main Rotor Performance Figure of Merit vs. $C_T/\sigma$ $L/D_e$ vs. Advance Ratio $\mu$ with corresponding table $\eta_p$ vs $J$ ( $\frac{V}{nD}$ )	RFP 2.4.8	5,13, Tbl. 5.2 5.2(a) 13.13,13.4 13.7
Aerodynamic Data: Airframe Airframe Aerodynamic Data Component Drag Buildup and Equivalent Flat Plate Areas Component Drag Buildup and Equivalent Flat Plate Area	RFP 2.4.8	12, Tbl. 12.3 13.1, Tbl. 13.1 13.1, Tbl. 13.2
Loads and Criteria Data Limit load factor structural and aerodynamic envelope V-Nz Diagram Component Design Loads	RFP 2.4.9	13.6 13.15
Mass Properties Data Empty Weight Derivation Mission Weight Buildup SAWE RP8A Part I Group Weight Statement Center of Gravity Analysis	RFP 2.4.10	14, Tbl 14.1 13.5 Tbl. 14.1 14.2,15.2
Manufacturing and Cost Data	RFP 2.4.11	17
Simulation and Flight Control Laws Development Flight Control Laws Integration into X-Plane	RFP 2.5 (grad only)	15 15.4.2 15.5
Stress Analysis and Fatigue Substantiation Blade Stresses Airframe Stresses Landing Gear Stresses	RFP 2.5 (grad only)	9 6.5 9 9.2
Aerodynamic Design Substantiation Rotor Aerodynamic Model Rotor Performance Fuselage Downforce and Drag Reduction Study	RFP 2.5 (grad only)	5,6 13, Tbl. 5.2 12
Propulsion system Details	RFP 2.5 (grad only)	11

[pages=2, width=16in, height=10in, offset=13.66cm -1.7cm]Images/Akinola/Subsystem $D$ Diagram.pdf

# 1 Introduction

The ability to takeoff and land vertically is imperative for modern, dynamic airborne military operations, which often occur in confined environments. This capability comes at the cost of speed and cruise efficiency seen in fixed-wing aircraft. As a result, Vertical Takeoff and Landing (VTOL) aircraft consistently carry less cargo, travel shorter distances, require more fuel, and are limited to slower speeds when compared to conventional fixed-wing aircraft. Today, speed is deemed equally imperative for future operation.

Rotorcraft engineers devote their time to pushing these envelopes in support of the warfighter whose very survival is at stake. High-speed VTOL (HSVTOL) aircraft have the potential to dramatically expand mission capabilities, save many more lives, and ultimately provide the United States and allies with a crucial advantage in national defense.

Recent military helicopters have only marginally expanded the speed and payload envelope. Heavy lift helicopters like the H-53 and H-47 have adopted a bigger is better approach, scaling up the transmission, turbine, and rotor system for a minor increase in speed. Figure 1.1 highlights the limited number of configurations that have exceeded 275 knots, with the directed thrust vehicles being the only ones having exceeded 450 knots. High-speed fighters have incorporated directed thrust to provide some VTOL capability, such as the AV-8B and F-35B. Directed thrust modifies the traditional tactical jet to hover by directing jet thrust as in the AV-8B or coupling the engine to a shaft driven lifting fan as in the F35B. These HSTOVL aircraft possess the speed and versatility desired, but they are not capable of significant payloads using those lifting methods. Additionally, the power loading of these vehicles is very poor and they produce extremely high downwash during takeoff and landing along with deafening noise that, even with protection, is harmful to the deck crew. This precludes long periods of hover, vertical landing on unprepared surfaces, and search and rescue operations where the safety of people or property on the ground is paramount.



Figure 1.1: Tested VTOL Configurations Grouped by Top Speeds

In a quest for the best of both worlds, tiltrotor aircraft were developed and refined, demonstrating efficiency

in both hover and cruise while compromising some payload fraction. The rotor-borne lift in hover allows a sizable payload to be lifted vertically, while the transition to wing-borne lift in forward flight increases range and speed capabilities. The compromise twist due to the lack of rotor speed reduction in cruise and the heavy pylon transition mechanism cut into the useful load.

Tiltrotors have been a mainstay of marine/naval aviation and most recently, adopted as the configuration of choice for the U.S. Army Future Long-Range Assault Aircraft. While tiltrotor technology is improving, the current state of the art is still far from achieving the goal of 450 kt cruise which is almost twice than what can currently be achieved. In 1991, NASA created an RFP based on technology needs for high-speed rotorcraft [2]. The mission profile of NASA's RFP starts with vertical takeoff at sea level followed by cruise at a speed of 450 knots for 350 nm and ending with descent to sea level and a 15 minute hover segment. Immediately, the similarities between the 1991 RFP and VFS 2023 RFP can be noted. Bell, Boeing, Sikorsky, and McDonald Douglass each submitted proposals to fulfill the requirements of the mission. These studies offered a bounty of configurations, each evaluated based on their ability to complete the mission. While most of the industry efforts were only conceptual, these reports were used as guidelines for preliminary decision making and ranking of each configuration. However, these were formulated thirty years ago. The advent of modern computational tools open the world to new innovations today. Materials and drive technologies and CFD and CSD tools have grown and matured since then that allow for advanced design and realistic reassessment of these creative ideas. More recently, NASA had completed an investigation in the design and technology requirements for heavy lift rotorcraft [3]. Speed was also crucial in this investigation, but at a lower cruise speed of 350 kts at 30,000 ft altitude with a range of 1200 nm. Extension to 450 knots is achievable but technological leaps in drive, structures, aeroelasticity, and propulsion are necessary. Although such advancements are significant, they need not come at great technical risk. Creative integration of modern technologies with a few key innovations can make a 450 kt HSVTOL a reality by 2035.

This was the challenge proposed in the RFP, and the University of Maryland Graduate Team's response is the *Arion*. The *Arion* is a mixed-power tiltrotor aircraft, utilizing both a prop-rotor and a turbofan for thrust in forward flight. This novel design configuration has a solid foundation in well-developed technologies that combine to provide the medium lift HSVTOL capability to a 450 kt aircraft. From afar, *Arion* looks and operates like a tiltrotor aircraft, but the augmented thrust and two-speed transmission enable it to reach new limits that neither the current tiltrotor nor a propeller aircraft can achieve alone. In Greek mythology, *Arion* is the winged horse of the hero Heracles. He rode the strongest and the fastest horse during many of his expeditions. *Arion* later saved the life of Adrastus, King of Argos, from the battlefield at Thebes. The capability to deliver cargo into and out of battle safely with massive power and lightning speed inspired our design.

## 2 Concept of Operations

### Aircraft Description

*Arion* is a four engine, mixed-power tiltrotor configured with two turboshaft engines driving its two main proprotors and two turbofan engines to augment thrust at high-speed cruise of 450 kts. The large cargo bay is capable of carrying 6000 lbs of equipment, or approximately 20 combat loaded troops. *Arion* is crewed by two pilots and a minimum of one aircrew. Its versatility enables a variety of mission sets to be conducted within the modular cabin.

The aircraft is configured with retractable landing gear, counter-rotating proprotors, twin turboshaft engines mounted in the mid-fuselage, and two turbofan engines mounted on top of the rear fuselage. The proprotors are capable of tilting from full forward at  $0^\circ$  in cruise to  $85^\circ$   $95^\circ$  in low-speed helicopter mode.



## General Operations

*Arion* incorporates two major technology advances over a current generation tiltrotor. First is the addition of an automated two-speed transmission. The second is the mixed-power configuration. The two-speed transmission allows for high efficiency in high-speed cruise. Shifting of the two-speed transmission is automatic when directed by the pilot. Turbofans mounted on top of the rear fuselage augments the aircraft thrust to provide quicker acceleration profiles and faster top speeds. The management of the augmented thrust is largely automated with the ability to override that automation if an alternate profile is desired. When *Arion* Vehicle Management System (VMS) is allowed to automate the turbofans, the only noticeable difference to the pilot will be a perceived boost to forward flight transition and cruise performance.

## Cargo Loading

*Arion's* spacious cargo bay is loaded primarily through a ramp on the rear side of the fuselage. With all the engines located at or above the top of the fuselage, personnel and equipment can transit the rear cargo bay ramp with all engines operating, permitting expeditious relaunch after loading or unloading operations. The cargo bay is equipped with optional cargo rollers and quick-lock pallet braces compatible with standard 463L pallets. A cargo winch at the front of the cabin and strategically placed pulleys make cargo handling quick and easy. Plentiful tie down points are also available for non-palletized cargo to be secured. If personnel are being carried, the cargo rollers quickly stow away, and 20 additional seats fold down from the interior bulkheads. Alternatively, scaffolding can be installed in the cabin to support 12 medical litters with seats available for 6 medical attendants. The cabin is outfitted with electrical outlets to power modular mission systems such as airborne command and control stations or mobile medical equipment. Additionally, internal fuel transfer receptacles allow auxiliary fuel tanks to be loaded into the cabin to extend endurance and range.

## Startup and Launch

During startup, the rotors face straight up, ready for vertical lift. The rotor shaft angle is modulated by a thumb switch on the pilot thrust control lever (TCL). An auxiliary power unit (APU) is started with battery or external power, and it provides electrical, hydraulic, and pneumatic power required to start the other engines. All engine start cycles are initiated and monitored automatically with the press of the respective engine start button on the overhead console. The turbofan engine is started on deck and sits at idle until commanded by the VMS on the transition to forward flight. If required for the mission, the pilots may also elect to keep the turbofan off, starting the engines in flight or completing the entire mission under turboshaft power.

To hover, the pilot simply centers the rotor shaft angle using the TCL thumb switch and advances the TCL. The fully fly-by-wire (FBW) control system and Full Authority Digital Engine Control (FADEC) increase thrust with collective inputs while maintaining constant rotor RPM. Traditional longitudinal and lateral rotor cyclic rotor inputs are utilized as well to maintain aircraft position in a hover. If flight conditions do not permit hover, a short rolling takeoff can be performed by tilting the rotor shafts forward at 60° to 80° while utilizing the turbofan thrust. Tilting the rotor shafts forward provides some forward thrust from the proprotors and also activates the VMS logic to command the turbofan engines to produce thrust. Since the turbofan thrust is a fraction of lift, jet noise is not an issue unlike directed thrust. The proprotors and turbofan engines provide quick acceleration, and the aircraft can lift off similar to conventional fixed wing aircraft once forward airspeed is sufficient.

## Transition to Forward Flight

During hover in or out of ground effect, the pilot uses the TCL thumb switch to initiate the transition to forward flight. Since the turbofan engines produce thrust purely in the longitudinal direction, the acceleration profile can occur more quickly. The proprotors continue to provide mostly vertical lift for the aircraft while the turbofan engines provide most of the accelerating thrust. The augmented thrust



ultimately widens the conversion corridor, giving the pilot increased safety and flexibility and allowing for transition without adjusting fuselage pitch angle. As the wings provide more lift with increasing speed, upward lift from the rotor shafts is reduced as they are tilted forward to provide forward thrust. Once the rotor shafts are tilted fully forward, the two-speed transmission is engaged by the pilot to reduce the proprotor rotational speed, allowing higher speed flight without experiencing adverse helical tip Mach effects on the rotors.

### Climb, Cruise, and Descent

The pilot has many options for configuring the aircraft during transit. While the aircraft can continue to fly in slower flight regimes with the rotor shaft tilted upward, most flights will tilt the rotor shafts fully forward and operate in airplane mode. In airplane mode, the aircraft operates like most conventional fixed wing aircraft. The VMS will automatically schedule the distribution of power between the engines based on the TCL position. The selection of aircraft power and attitude will determine the flight path. *Arion's* flight director can also be used to further reduce pilot workload and guide the aircraft throughout the flight profile on autopilot.

### Approach, Hover, and Landing

The process for converting to hover mode is largely the reverse of the transition to forward flight. From cruise, the aircraft is slowed by simply reducing the TCL. While slowing, the pilot initiates the automated two-speed transmission shift with the TCL thumb switch to accelerate the rotor. The acceleration is initiated aerodynamically by reducing the proprotor collective pitch angle while the turbofan continues to provide thrust to counter the increased rotor drag. The two-speed transmission is re-engaged at the faster speed once with a dog clutch once the speeds are approximately equal.

As airspeed continues to decrease, flaps are automatically extended to reduce the stall speed and widen the conversion corridor. The rotor shafts are tilted aft using the TCL thumb switch. The VMS will schedule the turbofan thrust during the conversion to assist the pilot in maintaining the aircraft in the conversion corridor to avoid stalling the wing or increasing structural load limits; however, the pilot may elect to manually control the turbofan thrust if desired. As the proprotor thrust is directed vertically, there is less requirement for the wing to produce lift and the aircraft can continue to slow smoothly to a hover. Landing can be accomplished vertically from a hover, or a rolling landing can be conducted if flight conditions do not permit hover.

To handle loss of power safely, the turboshaft engines are cross shafted and sized for one engine inoperative (OEI) condition. In cruise, in the case of turbofan engine failure, *Arion* can rely on power provided by turboshafts to safely glide or cruise at 250 – 300 kts.

## 3 Configuration Selection

### 3.1 Selection Methodology

The RFP called for a vehicle that is capable of “meeting critical military needs in a highly-contested environment”. It must carry a payload of 5,000 lb plus another 1000 lb of mission equipment in a 6.5 ft high, 8 ft wide, and 30 ft long cargo bay. Furthermore, disk loading must be kept low enough to limit downwash (and outwash) velocity for search and rescue operations and landing on unprepared surfaces. The vehicle cruise speed must be 450 kts with a cruise altitude of at least 20000 ft MSL in ISA conditions, and the Radius of Action (ROA) must be at least 500 nm.

The 450 kt cruise requirement along with low downwash in hover forced a unique approach to the configuration selection process. This is an extremely high speed that no current VTOL configuration can successfully accomplish. Therefore, prior to any Analytical Hierarchy Process (AHP) many configurations



had to be eliminated upfront.

A total of 13 different vehicle configurations were initially considered. These configurations were qualitatively assessed on their ability to achieve 450 kts cruise with limited downwash, reasonable complexity and acceptable Technology Readiness Levels (TRL). No vehicle has ever been flight tested that could meet the RFP requirements. Directed thrust vehicles can meet this speed, but have very high downwash and nowhere near the payload capability while tiltrotors and helicopters have suitable downwash and payload but nowhere near the cruise speed. Therefore emphasis was put on novel design concepts for consideration.

## 3.2 Mission Capability Analysis

### 3.2.1 Vehicle Considerations

A wide range of design options were considered for each vehicle configuration including unusual excursions. For example, electric propulsion or slowed rotor technologies were considered excursions around all configurations as novel design concepts.

In the end, three labels could be assigned. These were 1) Incapable of meeting the RFP, 2) Capable of meeting the RFP, with **extreme** complexities and many unverified technologies, 3) Capable of meeting the RFP, with moderate challenges and some novel technology.

### 3.2.2 Vehicles Considered Incapable of meeting RFP requirements



(a) Single Main Rotor



(b) Tandem



(c) Directed Thrust

1. **Single Main Rotor (SMR):** The single main rotor utilizes one large main rotor for lift, propulsion, pitch and roll control. The SMR utilizes a tail rotor for counter torque and yaw control. While this vehicle is dependable, extensively studied, and has been very successful on the battlefield and in the civilian sphere, no amount of careful design could make it fly at 450 kts. High hub drag, advancing blade compressibility, and loss of propulsive force make this vehicle perform very poorly at 450 kts if it flies at all. Furthermore, to keep the advancing blade tip from reaching supersonic flow, a slowed rotor would be necessary with extremely high advance ratios ( $\mu > 3.5$ ) in forward flight. These advance ratios are intolerable for a single main rotor helicopter due to retreating blade stall/reverse flow, loss of rotor lift, roll moment, severe rotor aeroelastic instability, and impossible vibrations.
2. **Tandem (two longitudinally offset counter-rotating rotors):** The tandem rotor system is another highly successful and proven aircraft. Its counter-rotating rotors allow the vehicle to do away with the tail rotor and use all its power to generate lift and propulsive thrust. It also has excellent longitudinal CG travel making it ideal for complex lifting missions. The counter-rotating rotors also alleviate roll moment at higher advance ratios due to retreating blade lift reduction and yaw control is easy with lateral tilt. Despite the benefits, the tandem helicopter has drags of two hubs. Furthermore, although the roll moment is balanced at high advance ratios, this design suffers from the same loss of lift, advancing blade compressibility, and rotor dynamics challenges as the single main rotor at high advance ratios. The NASA heavy lift tandem could be designed for cruise at 350 kts but beyond that speed, its L/D dropped drastically (at 450 kts it was 5 [1]).



3. **Directed Thrust (Turbofan exhaust directed downward):** Directed thrust configurations were analyzed due to their efficient and high-speed forward flight. Variations of this configuration were considered including pure directed thrust as seen on the Harrier and a combination of directed thrust with a lift fan as seen in the F-35B. While the forward flight capabilities are excellent, the heavy vehicle and small fan/direction thrust nozzle cause severe downwash speeds. This along with its resulting deafening noise would make the vehicle untenable for unprepared surfaces and unsafe for conducting search and rescue operations. These capabilities are integral to the needs of a VTOL-capable transport aircraft since combat zone missions often require operating from unprepared surfaces.

### 3.2.3 Capable of meeting RFP requirements, with major complexities



(a) Compound



(b) Co-axial with Thrust



(c) Stopped Rotor



(d) Fan-in-Wing



(e) Ducted Tiltrotor

1. **Winged Compound with & without Augmented Thrust:** A compound helicopter is similar to an SMR, however one wing can be added to balance the roll moment at high advance ratio flight, or two wings to provide the lift needed to compensate for a very slow main rotor. These innovations allow for higher forward flight speeds than the SMR and Tandem configuration. Optional thrust compounding with a pusher propeller or turbofan was also considered as seen on the Airbus RACER. Although the loss of lift at high advance ratios and roll moment are lesser concerns, rotor dynamics of a slowed edgewise rotor at extremely high advance ratios remain unknown. Drag was also a primary concern with this design. At high advance ratios, the rotor would provide minimal lift but contribute greatly to drag due to compressibility effects. The main rotor hub is also a great contributor to drag. Although the issues present in this configuration could be mitigated with careful design and novel technologies, every aspect of the design including aeroelasticity, loads, dynamics, and tail rotor design was riddled with serious challenges due to the edgewise flight condition. Modern Mach-scaled tests at the University of Maryland compound rig have exposed these challenges even at half the speed required by this RFP and they remain in the basic research phase [4–7]. This configuration possessed **extreme complexities and challenges** associated with the edgewise rotor system.
2. **Coaxial Compound Rotorcraft(& Inter-Meshing Rotor)** Coaxial helicopters consist of two stacked counter rotating rotors. This allows improved lifting performance over an SMR and eliminates the need for an anti-torque system. Utilized in a compound configuration for increased propulsive thrust, coaxial compound rotorcraft can achieve high speed without needing a wing because the counter-rotating rotors balance the roll moment at high advance ratios. This propulsion system is seen in the Sikorsky X2 technology and is proven and effective, however 450 kts is well beyond the current limits of the compound coaxial design. At such high speeds, rotors will need to be slowed drastically with advance ratios exceeding 3 to avoid supersonic flow at the advancing blade tip.



These conditions will lead to a significant reduction in lift leading back to the wing-based compound design discussed above. Even if wings could somehow be avoided, the hub drag would be very high at a cruise Mach number of 0.75 (450 kts at 25,000 feet ISA). The pusher prop needed would be impractical in cruise or if a turbofan would be used, it would ingest the rotor wake. Furthermore, hub loads would be enormous. Ultimately, like the wing-based compound configuration, the coaxial rotor-based design was deemed to have **extreme complexities and challenges**.

3. **Stopped Rotor(s) with Augmented Thrust:** A stopped rotor configuration was considered with many augmentations, taking inspiration from the Sikorsky S-72 X-Wing. Stopping the rotor allows for the vehicle to act like a standard fixed wing, where all of the thrust is coming from turbofans or propellers. But in wing mode, the rotor leading edge will be the trailing edge of the wing on the retreating side, so an elliptical airfoil with symmetry in all 3 axes is necessary which is poor aerodynamically at almost all speeds. Such an airfoil eliminates the Kutta condition and breaks down the very basis of lift generation. There are many resonance and mechanical challenges associated with stopping the rotor. Wing size and shape also compete with rotor size and shape requirements. Stowing the rotor was considered, but there is no room for stowing without a significant drag penalty, and the complexity was unmanageable. With the addition of powerful turbofans, this configuration was deemed **capable** of meeting the RFP requirements on paper, however many untested technologies would be required and it would possess **extreme** challenges.
4. **Fan-in-Wing/Body:** A ducted fan resides in the wing or body of the aircraft providing hover capabilities, while additional turbofans provide forward thrust capabilities. In cruise, the fans in the wing are covered to make a smooth lifting surface for the wing. The primary issues for this design are rotor size requirements for acceptable downwash, and rotor control. Installing a swashplate in the wing would require a very thick wing but without a swashplate control authority in hover is compromised. Theoretically, if each wing has its own fan, roll control can be achieved with thrust vectoring and a small pitch control nozzle could redirect air from the turbofans to provide pitch stability. The primary problem for this design is the lack of space. To provide space for the cargo bay, fuel tanks, proper wing structure, and large wing fans, this vehicle would become extremely large and hard to close the design in order to still meet the RFP requirements for downwash. Therefore, this configuration was deemed possibly **capable** of meeting the RFP requirements, but with **extreme** challenges.
5. **Ducted Tiltrotor/Tiltwing:** This configuration is similar to a tiltrotor and tiltwing, except the propellers/proprotors have ducting over them. This analysis varied designs similar to the flight-tested Bell X-22 to the conceptual XV-24 Lightning Strike. The ducting would be heavy and add even more weight to the hydraulic tilting system. It also would produce high drag in forward flight and severe pitch-up moments from duct lip flow. The blade flapping needed would not allow the ultra-small separation needed at the rotor tip (less than 1%R). The distributed propulsion tiltwing system similar to the Aurora was discarded for its impractical complexity, and lack of sensible space inside the fuselage. It was an experimental rig for hybrid electric flight not meant to be a practical aircraft.

### 3.2.4 Capable of achieving the RFP, with moderate complexities

1. **Tiltrotor:** Tiltrotors can take off vertically and hover like a helicopter. They can then convert to fixed-wing flight by rotating the rotor system forward like a propeller. There are several tiltrotor vehicles flying today and they have a good track record and are capable of achieving higher speeds and longer range than edgewise rotor configurations. Tiltrotors typically have L/D twice that of any helicopter above 120 kts reaching speeds above 250 kts, albeit with some price to pay in the payload. The drop in hover efficiency is due to rotor wake download on the wing and the need for





(a) Tiltrotor



(b) Tiltwing



(c) Variable Diameter



(d) Folding Tiltrotor

a smaller-sized rotor which would decrease power loading. Although tiltrotors can fly faster than helicopters, their speed is limited by wing-rotor instabilities, particularly whirl flutter. Principal challenges for 450 kt were expected to be whirl flutter mitigation, transonic drag reduction, running out of blade pitch, and achieving the power required in cruise using the turboshaft engines alone. A two-speed transmission, hingeless hub, judiciously selected tip speeds, and power augmentation with turbofan engines were considered to resolve these issues. CFD-based aerodynamic optimization of the fuselage, pylon, wing, and rotor blades would improve performance. The tiltrotor configuration was deemed **capable** of meeting the RFP requirements with **moderate** challenges that could be met with modern technologies and design tools.

2. **Tiltwing:** The key difference of tiltwing is that the entire wing rotates, not just the rotor system/nacelle as seen on tiltrotors. This rotation removes the wing from the rotor downwash in hover. The downside are structural weight needed to tilt the wing and very poor gust tolerance, since the wings act as sails, catching even small gusts. Furthermore, conversion is a challenge in tiltwings because of exorbitant weight overhead and the separation of flow at high wing angles, leading to buffeting and loss of lift. Whirl flutter and achieving power required for very high-speed cruise are aggravated due to lower wing root stiffness. Solutions to resolve these issues are similar to those for a tiltrotor, with an added structural and gust tolerance challenge. This configuration was deemed **capable** of meeting the RFP requirements with **moderate** challenges, however with more disadvantages than the tiltrotor.
3. **Variable Diameter Tiltrotor:** The Variable Diameter Tiltrotor (VDTR) operates like a tiltrotor, however its rotor blades telescope inwards during forward flight. The motivation for this design is to allow large rotors providing low disk loading to convert into small propellers in forward flight. This can help improve propulsive efficiency in forward flight when much less thrust is needed, and can also help mitigate whirl flutter. Short stiff propeller blades are already installed on fixed-wing aircraft flying above 450 kts without whirl flutter, hence converting rotors to propellers in forward flight is one option to resolve high-speed axial rotor aeroelastic instabilities. This technology has been wind tunnel tested by Sikorsky in 1994 [8] and has shown potential for feasibility. Still, the TRL for this technology is very low. For the same tip speed variable diameter leads to a higher blade loading (scaled by  $R^3$  not  $\Omega^2$ ) and the pilot will typically run out of collective at high cruise speeds. Thus, in addition to shrinking the diameter in cruise, a reduction in rpm is also required. This configuration has not yet been flight tested, and its design presents very significant structural and mechanical challenges. Therefore this design was viewed a complicated and unproven design although with significant potential. This vehicle was deemed **capable** of meeting the RFP requirements with



**moderate** challenges associated with blade structures and the retraction mechanism.

4. **Folding Tiltrotor with Turbofan Thrust:** In a folding tiltrotor the rotor folds back onto the nacelle during cruise and thrust is provided solely by turbofan engines. One very attractive technology for this vehicle are convertible engines. These are turbine-based engines which can be coupled to a shaft for turboshaft mode, or provide high pressure exhaust for turbofan mode. With convertible engines, the folding tiltrotor could use the same engines in hover, conversion, and high-speed cruise. Even though this is a dream solution, the TRL level for convertible engines was deemed too low for this RFP. The folding mechanism for this vehicle involves declutching the rotors, feathering them with collective to bring the RPM below 10, and finally locking and folding the rotors so they are stowed in a streamlined position along the nacelle. This design allows a helicopter to be converted to a jet aircraft, avoiding whirl flutter and powered by turbofan engines which provide high power at high altitude and speed. The complexity of this design is significant. Turbofan and turboshaft engines are required. Furthermore, while the folding mechanism has been proven in a wind tunnel test [9], it has never been flight tested and the technology remains somewhat nascent. This configuration was deemed **capable** of meeting RFP requirements, with **moderate challenges**.
5. **Tiltrotor with Jet Assist:** This design would operate exactly as a tiltrotor, however it would be augmented with a turbofan for forward thrust. Achieving sufficient power for very high-speed flight with turboshaft engines is a primary challenge for tiltrotors and would require large and heavy engines and drivetrain. Turbofans can be added to assist in providing thrust, mitigating this concern. The rotor will not run out of pitch. The rotor speed can be reduced dramatically which would increase /rev frequencies of the wing-pylon and alleviate whirl flutter. Like the tiltrotor, this configuration was deemed **capable** of meeting RFP requirements, with **moderate challenges**.

From this analysis, three configurations were discarded for inability to achieve a 450-kt cruise speed at 20,000 ft or above with 6000 lbs of cargo. Five configurations were deemed possible but involved excessive complexities and unproven designs with poor performance. Five configurations remained that required greater analysis: Tiltrotor, Tiltwing, VDTR, Folding Tiltrotor, and Tiltrotor with Jet Assist.

### 3.3 Key Design Drivers

Further qualitative comparison of these configurations was done to narrow the design choice to 3 options. Key design drivers, both requested explicitly by the RFP and foreseen measures of performance based upon operating requirements Section 2, were identified and used for the evaluation of the remaining aircraft. These drivers are listed below along with their importance based upon the RFP.

1. **Empty Weight Fraction/GTOW:** This driver acts a metric of the lifting capabilities of a configuration. A more efficient design would be one with a low empty weight fraction, meaning less weight is taken up by vehicle structure and more weight is utilized on “useful” weight.
2. **Disk Loading/Downwash:** The RFP states “the vehicle design shall include features to mitigate the severity of the outwash/downwash environment”. Low disk loading is desired to minimize outwash speeds, thus preventing toppling moments in hover, as shown in Figure 2 of the RFP. Additionally, the RFP offers another figure highlighting the disk loading associated with different vehicles as well as how various surfaces begin to degrade in the presence of rotor downwash. After further investigation of the RFP, a payload of 5,000 lbs corresponds to roughly 20 soldiers being transported, therefore low disk loading is desired in the case of troop transport.
3. **Top Speed:** Faster speed that exceeds the RFP requirement offers the capability to shorten the time duration of the mission, increasing the probability of threat avoidance.
4. **Cruise Efficiency:** The cruise efficiency is based upon vehicle L/D and propeller efficiency of the



rotors in airplane mode. The cruise and high-speed penetration segments are the longest segments of the mission profile, thus these segments dictate the power installed. Cruise operates in the region of drag divergence. Methods for achieving cruise of 450 knots in while minimizing drag include incorporating multiple types of engines, reducing radius or rpm of the rotor, and removing additional components that would contribute to profile losses such as the rotor's blades.

5. **Hover Efficiency:** Although hover is only a small portion of the overall mission profile, low power consumption is still important to add to the multi-mission capability of this design. Additionally, the fuel consumed during the hover segment can be lowered with more efficient hover.
6. **Aeroelastic Stability:** Hover and Cruise both present opportunities for configurations to become unstable. In hover, vehicles must tolerate small longitudinal and lateral shifts in the center of gravity due to potential gusts. In cruise, other instability phenomena may arise depending upon the configuration. Whirl flutter, for example, is a common occurrence of configurations with rotor, pylon, wing systems.
7. **Maneuverability:** The vehicle must withstand a 3.5g load factor as stated in the RFP.
8. **Acoustics:** For threat avoidance during hover, low acoustic signature is desired. While acoustic signature is not limited by regulations in a hostile environment, noise will inform enemies of an approaching vehicle.
9. **Survivability:** For most operating military operating conditions, foreign object debris can prove to be detrimental to the propulsion system of any aircraft. A configuration that can “minimize the susceptibility of the propulsion system to Foreign Object Debris (FOD) ingestion during takeoff and landing operations” will be ranked higher. Additionally, the capability to withstand gunfire is considered.
10. **Safety during loading/unloading:** The exposure of rotating components and hot exhaust near ground personnel during landing zones is a primary concern for vehicle selection. Additional consideration to other moving parts, such as a wing, during landing is also considered.
11. **Lifecycle Cost:** Minimizing cost is always a a priority in design. Lifecycle cost accounts for the cost of development, production, operation, and maintenance costs. Rotorcraft maintenance costs are notoriously high, this this driver also captures complexity of the vehicle design.
12. **Pilot Workload:** Although the pilot must be attentive in ny hostile environment, the pilot workload should be reduced as much as possible for such long trips. Since a group member is a current V-22 pilot, cockpit layout and workload during cruise and hover operations were noted based on their preferences.
13. **Technology Readiness Level:** A configuration with technology readiness level of 2023 is an existing aircraft that has been designed, manufactured, and flown. Due to the complexity of components to achieve the design mission, detailed components that may not currently exist are required for the operation of some configurations. Inherent problems arise during the development of new products, thus adding to the cost and timeline to first flight.
14. **Autorotation/Crashworthiness:** Due to the nature of the operating environment, methods of safe landing are considered in the form of autorotation and/or gliding. Cross shafting is necessary in the case of tiltrotors to satisfy one engine inoperable condition.

### 3.3.1 Analytic Hierarchy Process (AHP)

Design drivers were used for final vehicle selection. Each design driver was assigned a weight, representing the rank of importance relative to other drivers. The Analytic Hierarchy Process(AHP) was used to



determine the importance of each design driver. To remove bias, each group member constructed an AHP matrix with weights they deemed appropriate based on the RFP and mission profile. Each group member complied with a consistency index to ensure weights were not assigned randomly. Then, the mean values for the weights were calculated while ensuring a low standard deviation.

The AHP matrix, Table 3.1, is a summary of the rating of each design driver relative to each other as decided by averaging the group members individual AHP matrices. Each design driver (horizontal row) was evaluated against all other design drivers (vertical columns). The range of scores vary from 1/10 to 10 with scores <1.0 indicating the row criteria is less important than the column criteria and >1.0 indicating the row criteria is more important than the column criteria.

Table 3.1: Analytic Hierarchy Process (AHP) Matrix

	Empty Weight Fraction/ GOW	Disk Loading/ Downwash	Top Speed	Cruise Efficiency	Hover Efficiency	Stability	Maneuverability	Acoustics	Survivability	Ground Crew Safety	Cost/Complexity	Pilot Workload	TRL	Autorotation/ Crashworthiness	Normal Priority
Empty Weight Fraction/ GOW	1.00	2.00	9.00	0.80	4.00	3.00	4.50	9.00	3.00	6.00	5.00	7.00	4.00	3.00	0.19165
Disk Loading/ Downwash	0.50	1.00	4.50	0.40	2.00	1.50	2.25	4.50	1.50	3.00	2.50	3.50	2.00	1.50	0.09582
Top Speed	0.11	0.22	1.00	0.11	0.44	0.33	0.50	1.00	0.33	0.67	0.56	0.78	0.44	0.33	0.02159
Cruise Efficiency	1.25	2.50	9.52	1.00	5.00	3.75	8.88	9.52	3.75	7.50	6.25	8.75	5.00	3.75	0.24301
Hover Efficiency	0.25	0.50	2.25	0.20	1.00	0.75	1.13	2.25	0.75	1.50	1.25	1.75	1.00	0.75	0.0479
Stability	0.33	0.67	3.00	0.27	1.33	1.00	1.50	3.00	1.00	2.00	1.67	2.33	1.33	1.00	0.06387
Maneuverability	0.22	0.44	2.00	0.11	0.89	0.67	1.00	2.00	0.67	1.33	1.11	1.56	0.89	0.67	0.04137
Acoustics	0.11	0.22	1.00	0.11	0.44	0.33	0.50	1.00	0.33	0.67	0.56	0.78	0.44	0.33	0.02159
Survivability	0.33	0.67	3.00	0.27	1.33	1.00	1.50	3.00	1.00	2.00	1.67	2.33	1.33	1.00	0.06387
Ground Crew Safety	0.17	0.33	1.50	0.13	0.67	0.50	0.75	1.50	0.50	1.00	0.83	1.17	0.67	0.50	0.03193
Cost/Complexity	0.20	0.40	1.80	0.16	0.80	0.60	0.90	1.80	0.60	1.20	1.00	1.40	0.80	0.60	0.03832
Pilot Workload	0.14	0.29	1.29	0.11	0.57	0.43	0.64	1.29	0.43	0.86	0.71	1.00	0.57	0.43	0.02737
TRL	0.25	0.50	2.25	0.20	1.00	0.75	1.13	2.25	0.75	1.50	1.25	1.75	1.00	0.75	0.0479
Autorotation/ Crashworthiness	0.33	0.67	3.00	0.27	1.33	1.00	1.50	3.00	1.00	2.00	1.67	2.33	1.33	1.00	0.06387

Table 3.1 highlights the normalized priority of each design driver. Cruise efficiency is considered the most important design driver because it is expected to have a dramatic effect on vehicle sizing due to the domination of the cruise segments according to the mission profile. The second most important driver is empty weight fraction as a measure of volumetric efficiency. The third highest priority design driver is disk loading/downwash which is important for minimizing induced power in hover as well as allowing for safe working conditions for ground crew. Low disk loadings support multi-mission capability, a trait desirable based on supplemental material given by the sponsor. All drivers considered and corresponding weights are based on inputs from pilots, industry professionals, and the demands of the RFP. The weights given by the AHP matrix are used for configuration selection as shown in Table 3.2.



### 3.3.2 Tiltrotor Vs. Tiltwing

The tiltwing has structural challenges with tilting the entire wing in flight and also suffers from serious control authority and handling challenges in hover. The tiltwing also presents challenges in the conversion sequence, although this can be mitigated with control law development and pilot training. The primary benefit provided by the tiltwing is lower thrust required in hover due to the reduction in hover download on the wing from the downwash. This mission is not primarily a hover, thus the reduction in hover thrust for tiltwings are not a primary benefit for this mission. Meanwhile maintaining hover control authority and handling qualities in gusty conditions may be very important for a combat zone or search and rescue mission, so the tiltwing loses to the tiltrotor in hover comparison. Another benefit of tiltwings is the potential for installing several propulsors providing redundancy and reducing the wing tip weight. This design also would eliminate the need for cross shafting which adds weight and complexity to a tiltrotor design. However, disk loading with this design would be increased, leading to higher downwash, and longer wings would be required to compensate, which eliminates any weight and complexity improvement from this design.

### 3.3.3 Two-speed Tiltrotor Vs. Variable Diameter Tiltrotor

There are two primary reasons to reduce rotor radius in flight. The first is to attain sufficient blade loading in forward flight and the second is to reduce the tip speed. The drag in cruise can be as low as 10% of the weight (thrust in hover) so a corresponding 90% drop in  $\rho\pi\Omega^2 R^4$  is desired. Dropping tip velocity below 350-400 ft/s is undesirable (due to high propeller inflow/advance ratio). Fortunately, the increase in blade loading is proportional to  $R^4$  while tip speed is only proportional to  $R$  so a small reduction in blade radius can provide the large increase in blade loading required for cruise with low thrust. The corresponding reduction in tip speed reduces compressibility effects without causing an overly high propeller inflow ratio. This makes variable radius a slightly more attractive option for performance than a two-speed transmission since the increase in blade loading is only proportional to  $\Omega^2$ . Furthermore, the variable radius design might delay the onset of whirl flutter somewhat.

Despite the attractive design aerodynamically, a variable radius blade is very low TRL. It has never been tested in flight, and adds significant structural challenges, particularly for a twisted blade. The dynamic benefits of this design for whirl flutter are outweighed by the structural issues and mechanism weight. Centrifugal loading also is a challenge when decreasing rotor radius. Although the variable radius rotor provided some aerodynamic benefit over other designs, this design would likely not fly by 2035, so it was eliminated due to low TRL.

A summary of the configurations ranking is shown in Table 3.2. The Pugh matrix utilizes design drivers and corresponding weights as decided in Figure 3.1 to assign ranking to each configuration. Using a standard tiltrotor as a baseline configuration, grades ranging from -4 (much worse) to +4 (much better) were used to compare each configuration relative to the baseline.

Although the tiltwing has improvements in hover efficiency compared to other configurations, hover is only for six minutes total and the reduction in other metrics is enough to eliminate the tilt wing from consideration. Additionally, a variable diameter tiltrotor was eliminated due to its mechanical complexity and its low TRL. The three remaining configurations rank: (1) Tiltrotor with Jet Assist, (2) Folding Tiltrotor with Jet Assist, and the (3) Tiltrotor. For a more detailed analysis on these three configurations a detailed in-house sizing algorithm was used. Performance measures and other metrics amongst the three configurations are compared in Section 4.



Table 3.2: Pugh Martrix

	Weight	Tiltrotor	Tiltwing	Variable Diameter TR	Folding TR with Jet Assisst	TR with Jet Assist
Empty Weight Fraction/ GTOW	0.19	0.00	-3.00	-2.00	2.00	3.00
Disk Loading/ Downwash	0.10	0.00	-2.00	0.00	0.00	0.00
Top Speed	0.02	0.00	0.00	1.00	4.00	2.00
Cruise Efficiency	0.24	0.00	0.00	3.00	1.00	2.00
Hover Efficiency	0.05	0.00	2.00	-3.00	0.00	0.00
Stability	0.06	0.00	-4.00	2.00	1.00	-1.00
Manueverability	0.04	0.00	-3.00	2.00	2.00	-3.00
Acoustics	0.02	0.00	1.00	2.00	4.00	-1.00
Survivability	0.06	0.00	-3.00	-2.00	-3.00	-1.00
Ground Crew Safety	0.03	0.00	-2.00	0.00	-1.00	-1.00
Cost/Complexity	0.04	0.00	-4.00	-4.00	-5.00	-2.00
Pilot Workload	0.03	0.00	-4.00	-3.00	-4.00	-1.00
TRL	0.05	0.00	-1.00	-5.00	-4.00	-2.00
Autorotator/ Crashworthiness	0.06	0.00	-4.00	-1.00	-3.00	0.00
Total Weighted Score		0.000	-1.850	-0.189	0.038	0.599

## 4 Preliminary Vehicle Sizing and Final Configuration Selection

### 4.1 Sizing Methodology

To decide between the tiltrotor with jet assist, folding tiltrotor with jet assist, and standard tiltrotor, detailed analysis was carried out. These configurations were sized using an in-house developed sizing code. The sizing code allows trade studies comparing vehicles and design parameters by calculating vehicle weights and sizes for a given mission and set of design attributes.

#### 4.1.1 Mission Profile

The sizing mission (Figure 4.1) is from the RFP. It is a two-legged mission where each leg consists of:

1. 10-minute flight idle
2. Two-minute HIGE at 2,000 ft pressure altitude at 85°F (29.4°C) outside air temperature.
3. Cruise-climb to an altitude of at least 20,000 ft MSL; range credit given for distance covered
4. Cruise at 450 kts for the remainder of the 450 nm mission
5. Descent with no range credit given
6. 50 nm low altitude high-speed penetration at 2k/85°F (2,000 ft MSL, 85°F (29.4°C))
7. Two-minute Hover Out of Ground effect (HOGE) at 2k/85°F



8. A two-minute landing is performed after the second leg HOGE segment.

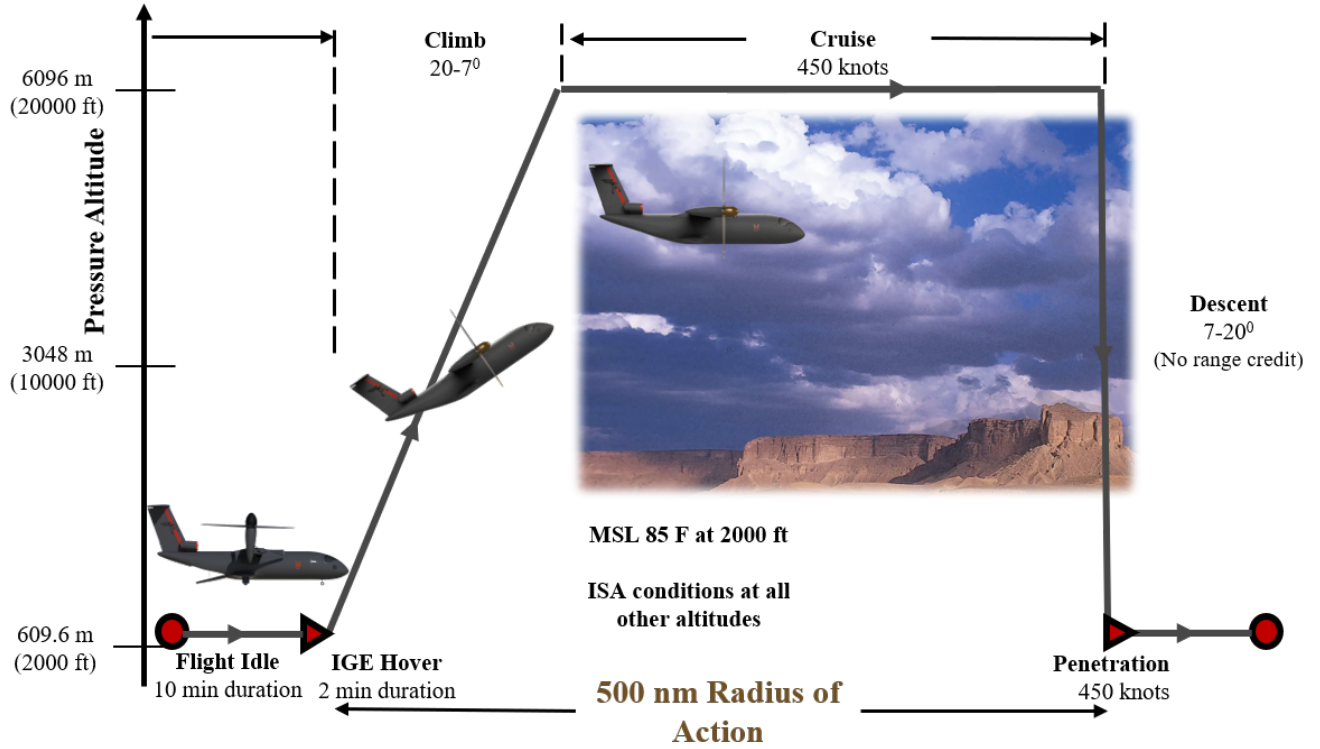


Figure 4.1: Mission Profile

According to the RFP, the takeoff and HOGE may not be conducted above a maximum of 90% engine maximum rated power (MRP), and 100% transmission maximum rated torque. The sizing code also limits the cruise power to maximum continuous power (MCP). Within the sizing algorithm, the intermittent rated power (IRP) was used in hover conditions, with a HOGE assumption in all hover cases; this condition sized the turboshafts in both the folding tiltrotor, and jet assist tiltrotor. The hover IRP requirement was considered 90% of MRP, while maximum continuous power was 76.2% of installed horsepower. Different lapse rates were used for both MCP and IRP conditions as well to account for density changes as altitude and temperature change. An unusual aspect of this design was the higher requirement of power in cruise than in hover. To ensure that there was sufficient design space for the hover ceiling, the installed turboshaft engines were sized for greater (10% extra) than the required power to ensure the HOGE not above 90% MRP specified in the RFP was met. This also allows *Arion* to have an expanded hover ceiling and hover loiter time, thus ensuring its ability to “meet critical military needs in highly-contested environments” that may require to hover above 2k/85°F and/or longer hover times for search and rescue operations.

#### 4.1.2 Sizing Algorithm

An in-house Blade Element Momentum Theory (BEMT)-based sizing code was developed for the calculations. The fixed input parameters are those that are specified by the mission, like payload, cruise speed, and technology inputs like engine specific fuel consumption (sfc). The varying inputs are the variables that characterize blade and wing geometry, such as disk loading, aspect ratio, wing loading, and performance metrics like the Figure of Merit and propulsive efficiency. Figure 4.1.2 shows the sizing flow chart. The iterative procedure starts with an estimate for gross takeoff weight and requires multiple iterations to



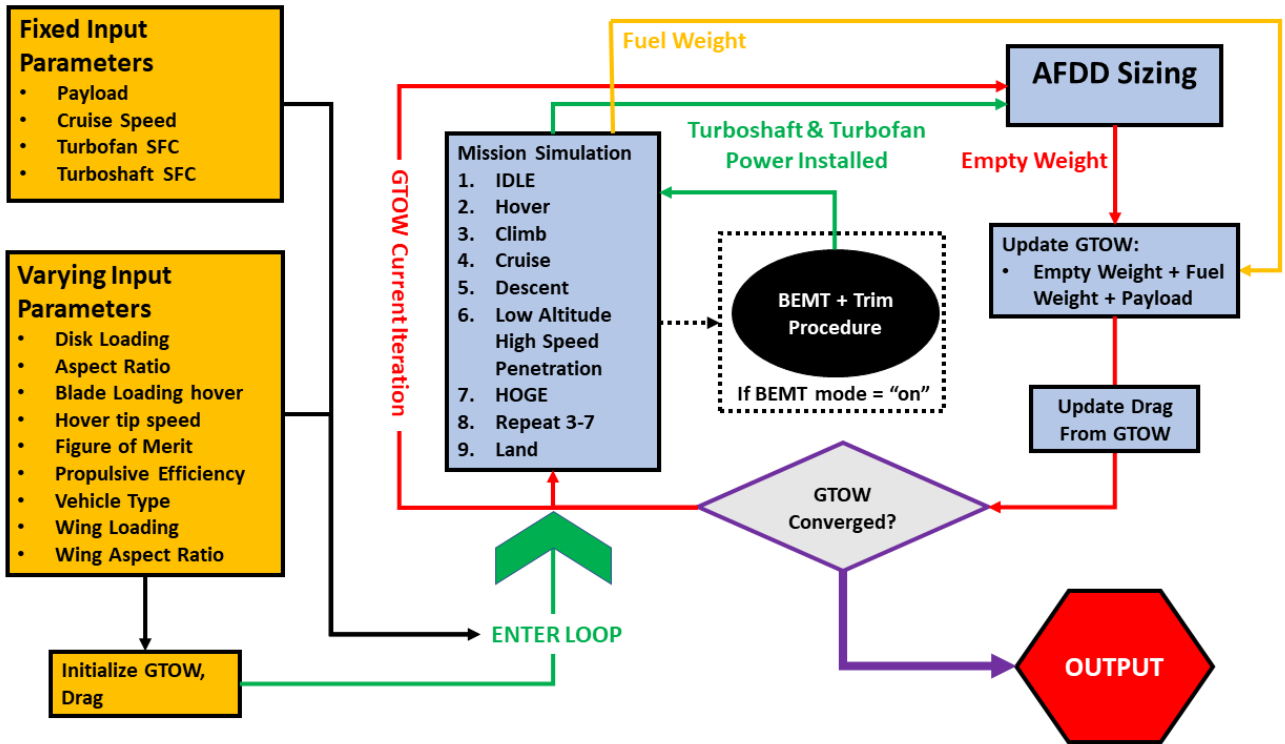


Figure 4.2: Flowchart for the configuration sizing procedure

converge. For a given takeoff weight, the vehicle drag is estimated using the modified Harris drag equation:

$$F = f \left( \frac{W_{lb}}{1000} \right)^{0.73} ft^2 \quad (1)$$

The exponent penalty was increased from the original  $2/3$  to  $0.73$  based on UMD wind tunnel test experience and in deference to the unprecedented speed and configuration type. The variable  $f$  is the Harris drag factor. Typically  $f = 1.5$  for tiltrotors, split into  $0.9$  for the fuselage and  $0.6$  for the wing and rotors.

The empty weights are estimated using standard U.S. Army Aeroflightdynamics Directorate (AFDD) models [10]. The AFDD equations do not provide estimates for non-conventional components such as turbofans, two-speed transmissions, or in-flight rotor locking and folding mechanisms. Hence, realistic assumptions were made based on published information to calculate these weights. For the in-flight rotor locking mechanism, according to [2], the folding mechanism resulted in a 20% increase of the total rotor system weight. This was incorporated in the sizing algorithm for folding tiltrotor cases. For the gearbox in tiltrotor and jet assist tiltrotor configurations, a step-up factor of 1.1 of the total gearbox weight was used based on [11]. The turbofan was sized based off Elodie Roux's work [12], where the weight of the engine is a function of thrust.

A low bypass ratio turbine was chosen for the initial sizing models due to their efficiency in the transonic regime over high bypass ratio turbines which have much greater power-to-weight ratio. It was initially found that the weight savings from fuel was worth the heavier of the two bypass ratio turbofan weights. A technology factor empty weight reduction of 15% was also incorporated to account for a broad spectrum of material and weight improvements that have taken place over the past 20 years, for all vehicle configuration choices. This allowed the individual designers of each component of the *Arion* to strive for empty weight fraction improvements during the design process, and was deemed acceptable due to initial calculations of weights utilizing composites and modern turbines.



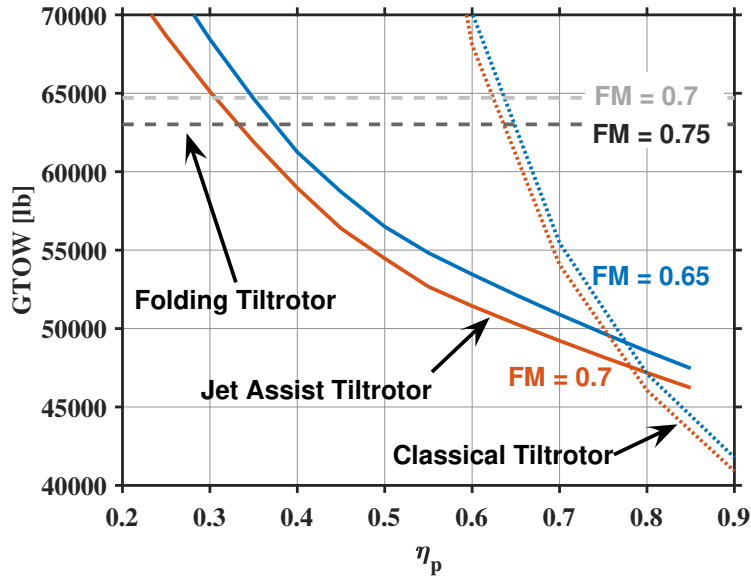


Figure 4.3: Predicted Gross Take-off Weight versus propulsive efficiency for folding and jet-assist tiltrotor

The overall empty weight is then added to the fuel and payload weight to give a new estimate for gross takeoff weight. This process is repeated till the gross takeoff weight is converged.

## 4.2 Initial Sizing Comparison

Parameter	Folding Tiltrotor 1	Folding Tiltrotor 2	Jet-Assist Tiltrotor 1	Jet-Assist Tiltrotor 2	Classical Tiltrotor 1	Classical Tiltrotor 2
Figure of Merit	0.7	0.75	0.65	0.7	0.65	0.7
Disk Loading [ $lb/ft^2$ ]	20	20	20	20	20	20
Number of Blades	3	3	5	5	5	5
Hover Tip Speed [ft/s]	700	700	800	800	800	800
Hover $C_T/\sigma$	0.138	0.138	0.138	0.138	0.138	0.138
Wing Aspect Ratio	6	6	6	6	6	6
Wing Loading [ $lb/ft^2$ ]	100	100	100	100	100	100
Harris Factor	1.64	1.64	1.59	1.59	1.59	1.59

Table 4.1: Parameters for Jet-Assist vs. Folding Tiltrotor Sizing Comparison

To select a final vehicle configuration, folding, jet assist and classical tiltrotors were compared (Table 4.1). A reasonable tiltrotor disk loading of  $20 lb/ft^2$  was chosen for all cases. Figure of Merit was assumed to be slightly higher for the folding tiltrotor since the rotor could be optimized for hover, hence 0.7 and 0.75 were considered whereas values of 0.65 and 0.7 were considered for the jet-assist and classical tiltrotors. The folding tiltrotor was limited to 3 blades to ensure sufficient space on the nacelle for the folded blades to be stowed in flight, whereas the jet-assist and classical tiltrotors had five blades. A hingeless hub negates the need for a specific  $-\delta_3$  setting by keeping the flap and lag frequencies well separated by design, thereby allowing space on the hub for more than three blades. A wing aspect ratio of 6 was used for all aircraft. A tip speed of 700 ft/s was set for the folding tiltrotor since that is considered standard for helicopters. The jet assist and classical tiltrotors require an RPM reduction, however tip speed in cruise must not drop below one-third of the cruise velocity. This leads to very high inflow ratios and impossible pitch controls so the hover RPM was raised to 800 ft/s for these configurations. Finally, a 3% increase in vehicle



form drag was added for the folding tiltrotor in cruise due to skin friction drag on the folded rotors and increased nacelle frontal area. This number was calculated using Prouty's drag build-up formulation [13] using XV-15 reference parameters.

Figure 4.3 shows the predicted gross takeoff weights for the vehicles from Table 4.1 as a function of propulsive efficiency. The folding tiltrotor does not have a rotor propulsive efficiency in cruise so folding tiltrotor weights are horizontal lines. The curve shows the jet assist tiltrotor is significantly lighter than the folding tiltrotor despite lower Figure of Merit as long as a propulsive efficiency of greater than 40% can be achieved. Initial BEMT calculations using blade and airfoil characteristics from the initial qualitative blade characteristics discussed in Section 5.2.3 showed propulsive efficiencies above 50% are possible in a 450 kt cruise so long as significant RPM reductions from hover are permitted. Furthermore, the technology for folding and stowing rotors in flight has only been tested in a wind tunnel but not in flight. Meanwhile, two-speed transmission designs have been flight tested as early as the 1950s and recently implemented in the Hummingbird A160 [14]. Therefore, the technology readiness level (TRL) of the folding tiltrotor design was assessed to be the lowest of the three configurations considered.

The classical tiltrotor was significantly heavier than the jet-assist tiltrotor for propulsive efficiencies below 75%. Additionally, the classical tiltrotor is very sensitive to propulsive efficiency shown by the sharp increase in weight below  $\eta_p = 0.7$ . For the classical tiltrotor, low thrust cannot be compensated for so reducing propulsive efficiency causes heavy engines, driving other system weights to increase as well. Another downside of relying solely on turboshaft engines is low power-to-weight ratios in high-speed flight. Turboshafts are limited by power available and high speeds require more power. Turbofans, however, can provide consistently high thrust at high flight speeds. Although turboshaft engines are slightly more fuel efficient, achieving power necessary using only turboshaft engines will require enormous engines, contributing tremendous weight, size and complexity. Figure 4.4 shows the weight of a rubber turbofan based on the CFM LEAP engine, and a rubber turboshaft (drivetrain weight included) based on the T700 engine to overcome the drag of an aircraft with a flat plate area of  $11.5 \text{ ft}^2$ . At 450 kts, the turboshaft weighs twice the turbofan. Turboshaft placement is also less flexible than turbofan. If placed inboard, this will increase fuselage and driveshaft size but if placed on the wing tips, wing weight and pylon drag will increase.

One significant concern with any tiltrotor is whirl flutter. Although this has been the primary impediment to high-speed tiltrotor flight in the past, improvements in hingeless rotor technology and careful blade, hub, and wing structural design allow for delaying the onset of whirl flutter significantly. At the University of Maryland, wind tunnel tests were conducted on a Froude-scaled three-bladed rotor in August 2022 up to 200 kts (458 kts full-scale) demonstrating a hingeless hub increases damping in whirl flutter. Due to in-house expertise in whirl flutter and advanced, validated whirl flutter and rotor stability analysis using the University of Maryland Advanced Rotorcraft Code (UMARC-II) [15–17], the team was confident that whirl flutter could be analyzed properly and designed for. Therefore, the jet-assist tiltrotor was selected as it offered the lowest weight for minimal added complexity and drag penalty with confidence that high-speed aeroelastic stability can be achieved.

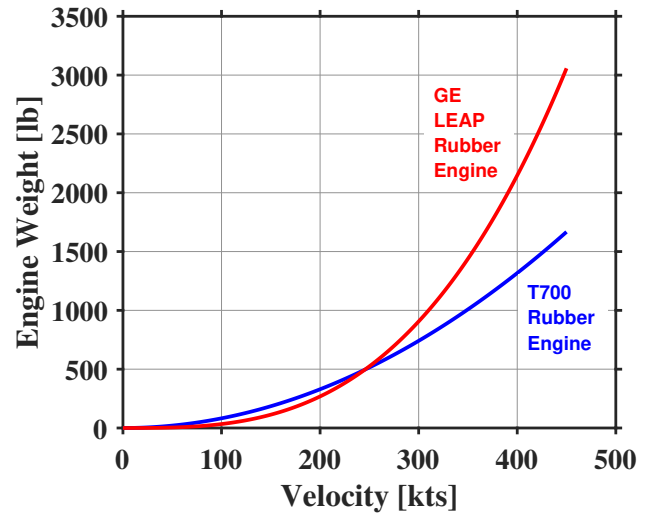


Figure 4.4: Turboshaft and turbofan weights required to overcome drag of a vehicle with a flat plate area of  $11.5 \text{ ft}^2$



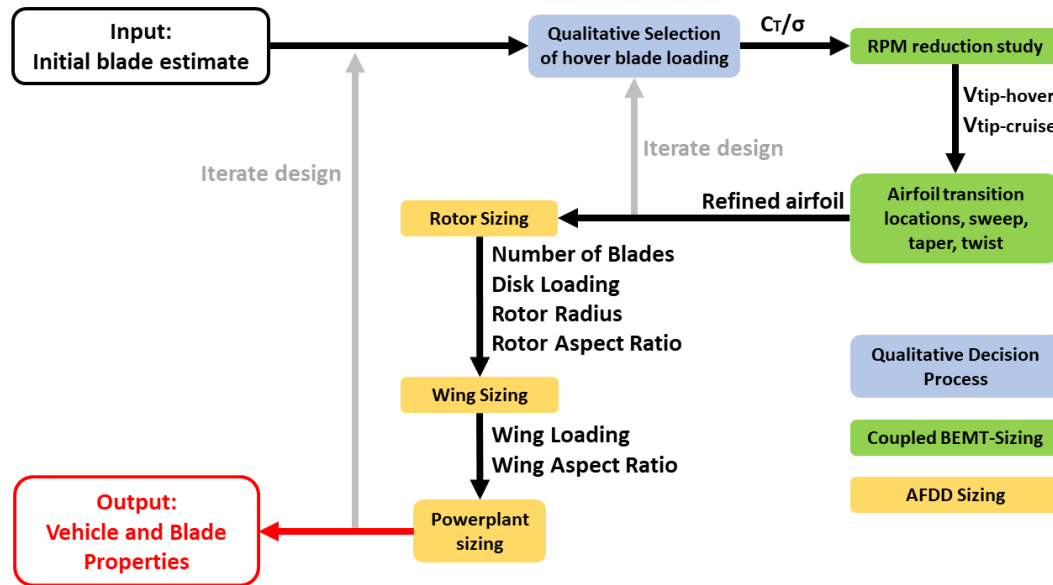


Figure 5.1: Vehicle Sizing and Aerodynamic Design Process

## 5 Detailed Rotor and Vehicle Sizing

### 5.1 Refined Sizing Methodology

The refined sizing and aerodynamic design process is an iterative process and is described in Figure 5.1. Prior to conducting trade studies, qualitative assumptions and design choices were made to select an initial blade design and hover blade loading target. A Blade Element Momentum Theory (BEMT) based rotor trim code was developed in-house to perform trade studies on aerodynamic parameters. This code was used to conduct trade studies of several parameters – cruise RPM reduction, blade twist profile, airfoil transition locations, sweep, and taper, on the Figure of Merit and propulsive efficiency of the rotor. The sizing code described in Section 4.1.2 was coupled with this BEMT. This process is iterative, as shown in Figure 5.1. Once the final blade aerodynamic properties were determined, propulsive efficiency and Figure of Merit were set in the sizing code, and trade studies on rotor and wing sizing power were conducted.

### 5.2 Qualitative Analysis

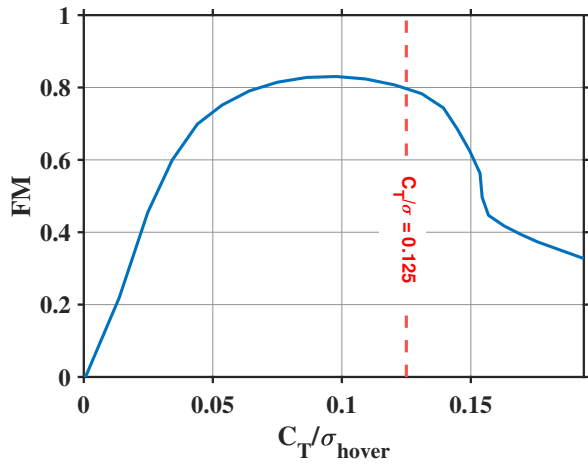
Before conducting trade studies, qualitative analysis was performed to get a preliminary design. Since the sizing process is highly coupled, these first estimates were used as baseline values to begin trade studies.

#### 5.2.1 Blade Loading

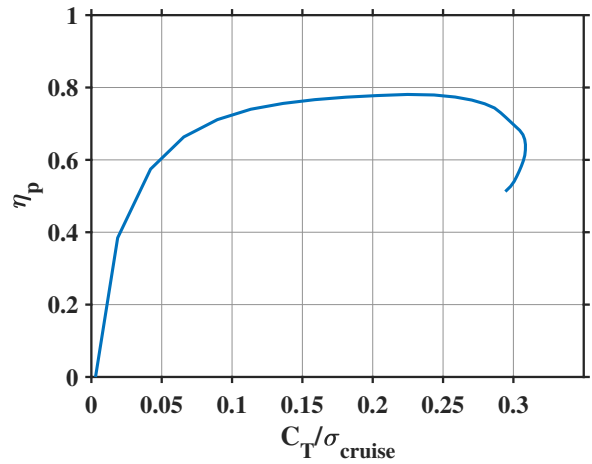
Blade loading ( $C_T/\sigma$ ) is one of the primary drivers of performance and one of the competing parameters between hover and cruise. In hover, lower blade loading is preferred, to avoid low stall margins and improve hovering performance, however in cruise low solidity is preferred. Figure 5.2 shows the variation of the Figure of Merit and cruise propulsive efficiency as a function of blade loading. When operating at maximum continuous turboshaft power,  $C_T/\sigma$  in cruise is related to  $C_T/\sigma$  in hover through equation

$$\frac{C_T}{\sigma}_{cruise} = \frac{P_{avail-cruise} \eta_p}{WV_{cruise}} \left( \frac{\rho_{hov}}{\rho_{cruise}} \right) \left( \frac{V_{tip-hov}}{V_{tip-cruise}} \right)^2 \frac{C_T}{\sigma}_{hover} \quad (2)$$





(a) Figure of Merit vs. Hover Blade Loading



(b) Propulsive Efficiency vs. Cruise Blade Loading

Figure 5.2: Effect of blade loading on hover and cruise performance

At high speed, the denominator  $WV_{cruise}$  is very high, causing cruise  $C_T/\sigma$  to be much lower than hover  $C_T/\sigma$ . Very low  $C_T/\sigma$  in cruise leads to a drop in propulsive efficiency as shown Figure 5.2(b). To increase cruise  $C_T/\sigma$ , the highest hover blade loading was chosen within acceptable stall margin limits. Figure 5.2(a) shows the Figure of Merit vs. hover blade loading  $C_T/\sigma_{hover}$ . A blade loading in hover of 0.125 was chosen. The stall margin is necessary to stay far from the blade stall in hover but also in edgewise flight. In edgewise flight, the stall  $C_T/\sigma$  decreases with increasing speed. At higher speeds, the wing offloads the rotors; hence the required  $C_T/\sigma$  is reduced as compared to hover.

### 5.2.2 RPM Reduction

Equation 2 shows that  $C_T/\sigma$  in cruise increases proportionally to the square of the RPM reduction ratio. Cruising at a higher altitude to increase density ratio does not increase cruise  $C_T/\sigma$  significantly, because the lapse rate effect leads to a corresponding drop in turboshaft power available in cruise. Therefore, dropping tip speed is the only way to maintain adequate performance for the rotor at high speeds. Simple hand calculations and prior analyses [3] make it obvious that this drop in RPM should be in the range of 50-70% for performance at 450 kts. Figure 5.3 shows the effect of drag reduction and RPM reduction on a simple BEMT model for the XV15. Reducing drag to a harris factor of 1.5 helps achieve more efficient flight but does not allow flight at very high speeds due to blade compressibility. Reducing the RPM to 60% of its hover value allows an XV15 modified for reduced form drag to achieve an L/D of 4 at 450 kts.

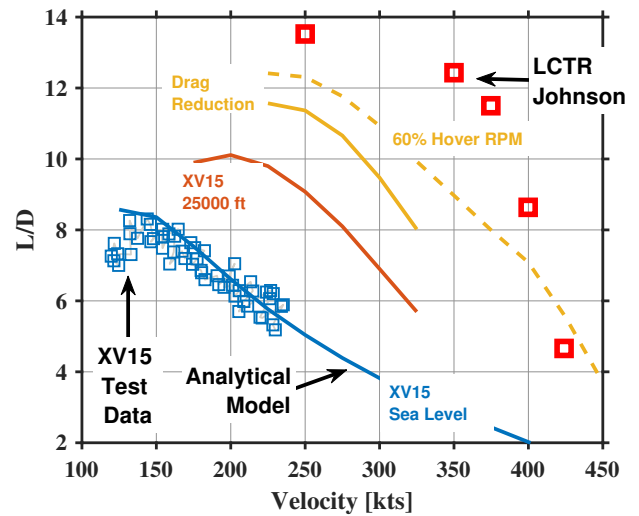


Figure 5.3: L/D vs velocity for modified XV-15 with test data (conceptual study)

Unlike the modified XV15 model, the jet assist tiltrotor has small turboshafts which do not provide all



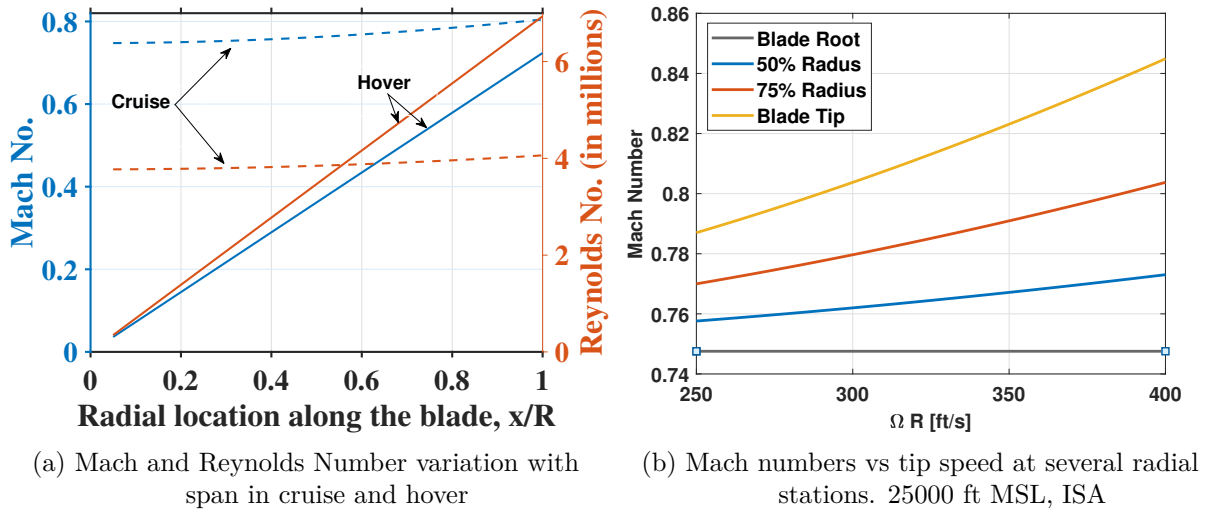


Figure 5.4: Mach and Re Number variation with span and tip speed

the thrust for cruise. Therefore,  $C_T/\sigma$  in cruise will be significantly lower than the modified XV15 model, and require an RPM reduction of greater than 40%. In order to achieve such high RPM reductions, high hover tip speeds up to 875 ft/s were considered to allow for RPM reduction while also keeping cruise tip speed sufficiently high. The minimum tip speed in cruise considered was 250 ft/s since that corresponds to an inflow ratio  $\lambda_c = 3$ . Propellers operate extremely poorly above  $\lambda_c = 3$  because the inflow angle at the tip is  $71.6^\circ$  and even higher moving inboard. At such high inflow angles, the airfoil lift and drag vectors are tilted so that airfoil lift contributes very little rotor thrust and requires high engine torque, while airfoil drag contributes negative rotor thrust. The price to pay is a very high blade pitch. Hence, the final RPM reduction of 63.4% was determined by considering blade pitch limits and propulsive efficiency  $\eta_p$  maximization. These trade studies are discussed in Section 5.3.1.

### 5.2.3 Blade Airfoil

At 450 kts and an altitude of 25,000 ft, the entire rotor blade experiences Mach numbers greater than 0.75. A special tip airfoil had to be designed for such transonic speeds using modern in-house CFD solvers – the UMD 16005.

Airfoil selection began with determining the Mach and Reynolds number distributions in hover and cruise, shown in Figure 5.4(a). This distribution profile was made using a cruise tip speed  $\Omega R_{cruise}$  of 303 ft/s and hover tip speed  $\Omega R_{hover}$  of 828 ft/s. Other properties used to generate this plot are in Table 5.2.

In hover, flow velocity over the blade varies from zero at the root to the  $\Omega R_{hover}$  at the tip. In cruise, the high cruise speed (450 kts) and RPM reduction reduces the spanwise velocity variation. Mach number is higher in cruise due to the very high cruise speed, while the Reynolds number is higher in hover due to a higher density at 2,000 ft MSL in 2k/85°F atmospheric conditions. Compressibility effects in cruise drive airfoil selection and blade design. Nearly the entire rotor disk experiences turbulent flow ( $Re > 10^6$ ) past the root cutout in both hover and cruise, so transition was not a factor and the same airfoil tables (generated using 2D RANS CFD) were retained for hover and cruise.

The helical tip Mach number variation with tip speed for several radial stations is shown in Figure 5.4(b). This together with high pitch angles will lead to transonic flow and enormous drag. Since the entire blade will be operating at Mach numbers between 0.75 and 0.85, thin and transonic airfoils are required to mitigate compressibility effects. Structural considerations in hover, however, require a thicker root section.



Blade Section	Airfoil	Thickness (t/c)
Tip section (Low Drag)	SSC-A07	7.0%
	NACA 16006	6.0%
	UMD 16005 Airfoil	5.0%
Section 3 (Best L/D)	NPL-9510	11.1%
	V23010-1.58	10.2%
	SC1095	9.5%
	NACA 16009	9.0%
	SSC-A07	7.0%
Section 2 (Transition)	VR-7	12.0%
	NPL9510	11.1%
	V23010-1.58	10.2%
Inboard (Struct. Support)	NACA64(A)-015	15.0%

Table 5.1: Airfoils considered for Rotor Blade

Therefore, the blade was divided into four distinct radial sections, along with a 12% root cutout, each with its own purpose and evaluation standards:

1. Root Cutout: A large spinner with a carefully shaped pylon will be used to cover the root cutout. The spinner drag is lower than the transonic drag penalty of a thick airfoil at the root. Instead, the spinner hides cylindrical blade root needed for strength.
2. Thick Root Section: The inboard blade airfoils of 15% t/c was selected to provide sufficient bending strength in hover. This is a thinner-than-usual airfoil for the root section, chosen to prevent transonic drag. So, the root stresses were verified using 3-D finite element analysis X3D 6.5. This code is validated with 1/4-scale V22 test data from the DNW wind tunnel.
3. Transition Section: The airfoils that provide excellent aerodynamic performance at high Mach numbers are usually very thin; hence, a transition region is used between the thick root and thin outboard sections to allow a smooth transition.
4. Lifting Section: This region is selected for best aerodynamic performance in cruise. It should provide excellent lift and low drag at high Mach numbers.
5. Thin Tip Section: The blade tip experiences high Mach numbers, around 0.8 or greater, so it is susceptible to high compressibility effects; therefore, an airfoil with low drag characteristics at high Mach numbers is desired.

The airfoils considered for each section are summarized in Table 5.1. Research airfoils from Boeing Vertol, VR-7 and V23010-1.58, have been used on the CH-47 and AH-64. The SC1095 and SSC-A07 airfoils are second-generation airfoils developed by Sikorsky with low thickness, well suited for transonic flow. The NPL9510 airfoil is a supercritical airfoil developed by British National Physics Laboratory. NACA 16 series airfoils are well researched propeller airfoils which can be utilized for the outboard region of the blade. Additionally, a 5% thick symmetric airfoil was invented in-house specifically for the blade tip. The airfoil geometry is shown in Figure 5.5.

In the transition section of the blade, airfoils ranging from 10-12% thick are considered. These thicknesses were chosen because they are approximately halfway in between the thick 15% root airfoil, and the thinner outboard section airfoils. Because the first structural root section takes up the first 50% of the blade, the transition section begins at 50% radial location where it will experience Mach numbers ranging from 0.76 to 0.775 in cruise depending on the exact radial station and final cruise  $\Omega R$  selected, as shown in Figure



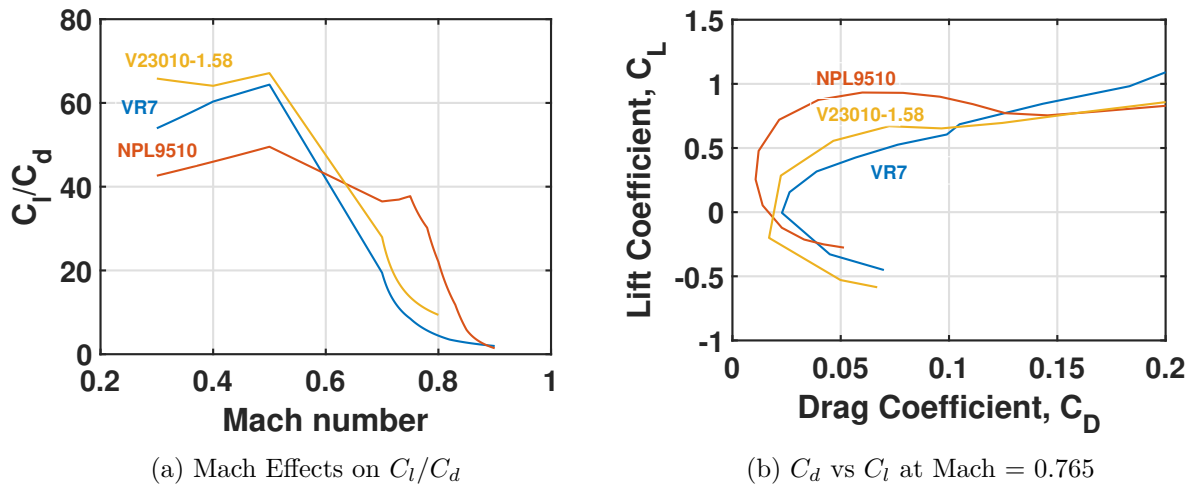


Figure 5.6: In-house CFD predicted performance of airfoils in the transition region

5.4(b). In Figure 5.6(a)  $c_l/c_d$  is plotted against Mach numbers for the three airfoils considered, showing that compressibility effects are delayed to the highest Mach number by the NPL9510 airfoil. The airfoil drag buckets at a Mach number of 0.765 as shown in Figure 5.6(a). Figure 5.6(b) shows that the NPL9510 airfoil provides the highest lift with the lowest drag out of the airfoils considered. Hence, the NPL9510 airfoil was selected for the transition region.

In the lifting section of the blade, obtaining the highest lift-to-drag ratio was desired at the operating angles of attack in cruise. Typically, thicker airfoils provide high lift but have low drag divergence Mach number, while thinner airfoils provide less lift but delay compressibility effects. A range of airfoils from 7-11%  $t/c$  with a variety of rotorcraft, symmetric, and supercritical airfoils were evaluated. The outboard blade section (denoted as the lifting section above) begins right after the transition region at around the 60% radial location and ends near the tip around the 90-95% radial station. This section experiences Mach numbers between 0.76 to 0.81 as illustrated in Figure 5.4(b). Figure 5.7(a) shows  $c_l/c_d$  vs Mach number for the airfoils considered at an angle of attack of 2 degrees. Out of the five airfoils considered, the NPL9510, NACA 16009, and SSC-A07 stand out due to their ability to delay compressibility effects with the SSC-A07 performing the best beyond a Mach number of 0.8. The drag buckets for all five airfoils considered is shown in Figure 5.7(b) at a Mach number of 0.785. The NPL9510 and SSC-A07 stand out in this figure. The NPL9510 provides the best lift for drag coefficients between 0.02 and 0.06 but has a significantly higher minimum drag coefficient than the SSC-A07 and a lower maximum lift coefficient. Hence, the SSC-A07 airfoil was selected for this region.

Lastly, the blade tip airfoil was designed to minimize transonic drag. The farthest outboard section of the blade will typically experience tip loss, thus providing less lift than the remainder of the blade, while experiencing significant compressibility effects. At a radial station beyond 90% the Mach number will range from 0.79 to 0.84, as shown in Figure 5.4(b). At this Mach number, even the thinner transonic and supercritical airfoils considered for the outboard section of the blade will experience severe Mach effects as

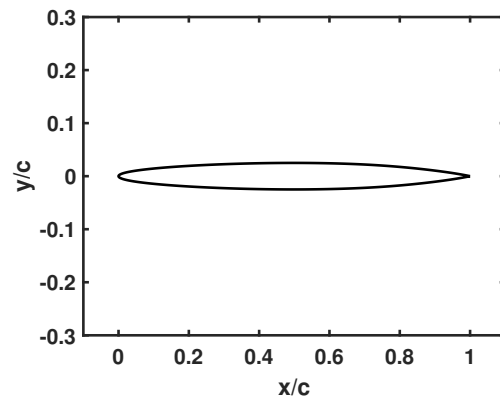


Figure 5.5: In-house UMD 16005 Airfoil



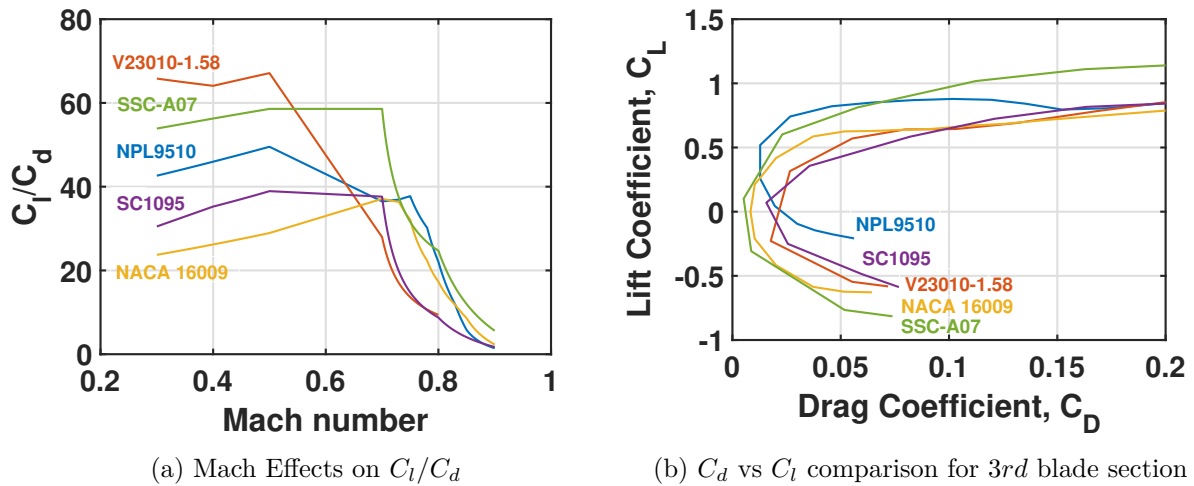


Figure 5.7: In-house CFD predicted Characteristics of best aerodynamic performance airfoils

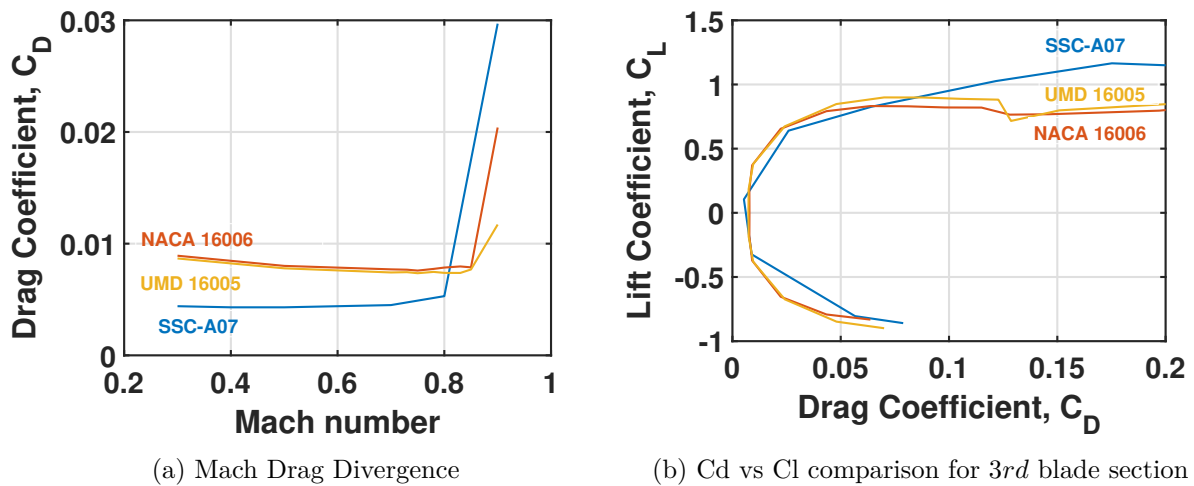


Figure 5.8: In-house CFD predicted Characteristics of best aerodynamic performance airfoils

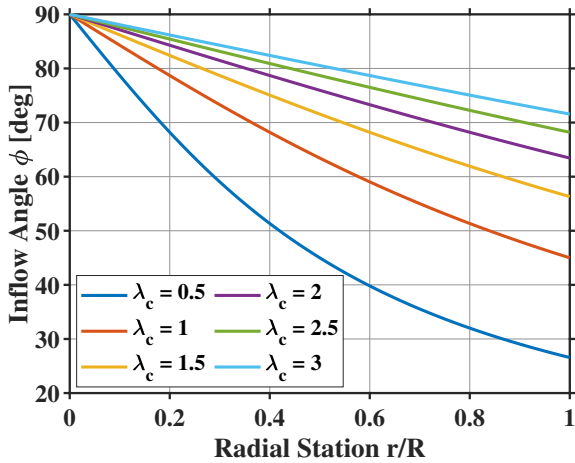
can be seen in Figure 5.7(a). Therefore very thin airfoils (5 - 7% thick) were considered – both symmetric and supercritical. Ultimately, a unique 5% thick airfoil was designed in-house. Figure 5.8(a) shows the drag coefficient vs. Mach number at zero angle of attack for the three airfoils considered. The 5% airfoil developed in-house delays drag divergence showing only a slight increase up to Mach 0.9. The drag bucket for the airfoils considered for this section is shown in Figure 5.8(b) at a Mach number of 0.8, showing that all airfoils considered perform very similarly at this Mach number with the 5% thick airfoil being the best of all. Hence the 5% thick airfoil was selected for the blade tip. These types of thin airfoils were suggested and studied by Harris in NASA CR-196702 [18] but not needed in the U.S. government heavy lift studies for 350 kt cruise. They become essential for 450 kts.

### 5.2.4 Blade Twist Setting

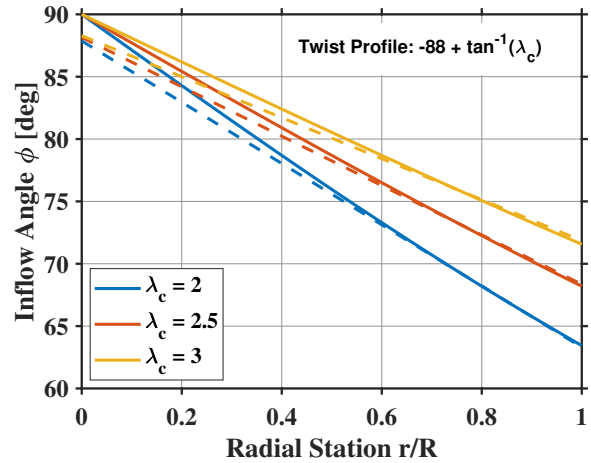
Traditionally there is a design compromise between twist for best hover performance and twist for best cruise performance, but the compromise diminishes at lower tip speeds due to high  $\lambda$  or high inflow angle  $\phi$ . The induced inflow is approximately zero for high-speed cruise (although it is included in the analysis). For



prop-rotor inflows around  $\lambda_c = 1$ ,  $\phi$  at the tip of the rotor blade is  $45^\circ$ , therefore to keep a constant angle of attack over the blade, mean blade twist should be around  $45^\circ$ . Such a high twist is very undesirable for edgewise flight. At very high inflow ratios however, this trade-off is less pronounced. Figure 5.9(a) shows a plot of inflow angle  $\phi$  versus radial station.



(a) Inflow angle ( $\phi$ ) versus radial station ( $r/R$ ) for different inflow ratios ( $\lambda_c$ )



(b) Inflow angle ( $\phi$ ) versus radial station ( $r/R$ ); (a) effect of varying inflow ratio, and (b) blade twist profile achieved

Figure 5.9: Inflow angle ( $\phi$ ) versus radial station ( $r/R$ ). Left shows effect of varying inflow ratio and right shows twist profile achieved

At high inflow ratios, the required blade twist to maintain constant angle of attack decreases and becomes more linear, meaning that the trade-off between edgewise/hover performance versus cruise performance diminishes. As mentioned in Section 5.2.2, the required RPM reduction is at least 50%, which reduces the cruise tip speed and increases the inflow ratio in cruise. We considered cruise tip speeds as high as 375 ft/s ( $\lambda_c = 2$ ) and as low as 250 ft/s ( $\lambda_c = 3$ ) in trade studies. Figure 5.9(a) shows at those inflows, twist profile for constant blade angle of attack should be fairly linear and no greater than 25 degrees. For baseline analyses the linear twist was set by the equation  $\theta_{tw}(x) = -88^\circ + \arctan(\lambda_c)$ . This equation provides a linear twist which in cruise, will maintain a relatively constant angle of attack in the outboard section while allowing the angle of attack to reduce slightly in the inboard section as shown in Figure 5.9(b). Low or slightly negative angles of attack at the root will decrease airfoil lift and drag forces to a minimum. This is desirable because, the inboard section is a thick airfoil that is set to a blade pitch of nearly 90 degrees in cruise, meaning airfoil lift will contribute to rotor torque, and airfoil drag will contribute a negative thrust. Both of these forces reduce prop-rotor cruise performance so minimizing both the airfoil lift and drag near the root is a design feature. Further refinement of the twist profile is discussed in Section 5.3.2.

### 5.2.5 Disk Loading

Low disk loading means reduced downwash, which is beneficial for search and rescue operations and improves the landing capabilities in dusty environments. On the other hand, low disk loading for a tiltrotor increases the wing span and, therefore vehicle weight significantly. An initial guess of  $20 \text{ lb}/\text{ft}^2$  was used in trade studies prior to the refinement of the disk loading parameter, which is discussed in Section 5.4.



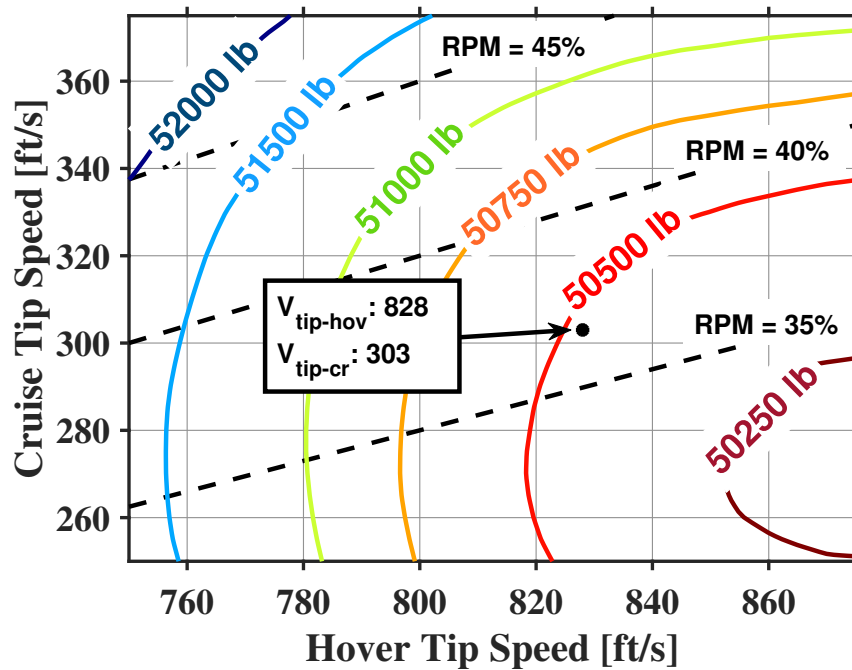


Figure 5.10: Gross takeoff weight [lb] variation with hover and cruise tip speeds

### 5.3 Aerodynamic Trade Studies

Trade studies were conducted using the parameters chosen in the previous section for the baseline blade to maximize the propulsive efficiency and Figure of Merit. The following parameters were varied to obtain the optimal design: hover and cruise tip speeds, blade twist profile, blade sweep profile, and the airfoil transition location.

The trade studies were carried out using an in-house developed propeller BEMT model for target blade loading. Large inflow angles are handled exactly. The model is capable of handling twist, taper, and sweep with multiple airfoils along the span exactly using the full  $3 \times 3$  coordinate transformations from the rotor frame to the airfoil frame.

#### 5.3.1 Hover and Cruise Tip Speeds

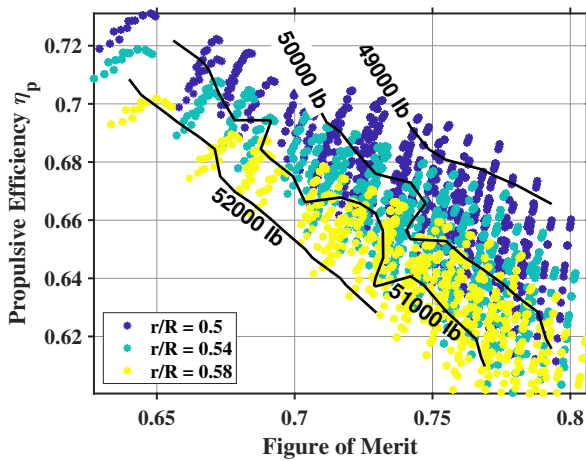
The design trade study between hover and cruise tip speed is shown in Figure 5.10. RPM reduction percentages between hover and cruise are displayed in dashed lines. The following are the takeaways from Figure 5.10.

1. Gross takeoff weight increases with decreasing hover tip speed, for a constant cruise tip speed. This is because reducing tip speed in hover only will result in a lower RPM reduction value, leading to a lower cruise performance as discussed in Section 5.2.2.
2. Gross takeoff weight increases with decreasing hover speed, for a constant RPM reduction. This is because reducing hover tip speed while maintaining a constant RPM reduction requires lowering cruise tip speed. The corresponding increase in propeller cruise inflow ratio  $\lambda_c$  reduces cruise performance as discussed in Section 5.2.4.
3. Increasing hover tip speed achieves diminishing returns above 820 ft/s. This is because of an increase in structural weight required with high centrifugal loads and a decrease in Figure of Merit due to

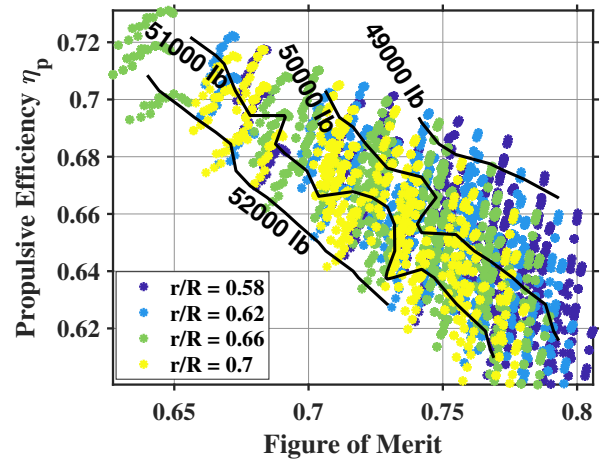


blade tip compressibility effects. A decreased Figure of Merit results in higher turboshaft weight and the improved cruise performance may not necessarily compensate for this increase in engine weight. Finally, a hover tip speed of 828 ft/s and a cruise tip speed of 303 ft/s was chosen for the design.

### 5.3.2 Blade Airfoil Transition



(a) Inboard airfoil transition (15% - 11% t/c)



(b) Inboard airfoil transition (11% - 7% t/c)

Figure 5.11: Variation of airfoil transition locations with efficiency and gross weight

The three airfoil transition locations were varied, as shown in Figure 5.11. The variation of propulsive efficiency and Figure of Merit is displayed, and the resulting vehicle gross takeoff weights contour lines are overlaid on the figures to help judge the design trade. Figure 5.11(a) shows improved propulsive efficiency with the most inboard transition at 0.5R from the 15% to the 11% thick airfoil without a corresponding decrease in Figure of Merit. The inboard transition location also provides the lowest gross takeoff weight. Radial stations below 50% were not considered for this transition due to structural load concerns.

Figure 5.11(b) shows an improved Figure of Merit with a more inboard transition from the 11% to 7% thick airfoils while propulsive efficiency is not affected much. The lowest gross takeoff weight is achieved at transition locations between 0.58R and 0.62R. Therefore 0.6R was chosen.

Finally, Figure 5.12 shows the transition from the 7% to the 5% thick airfoil. The lowest gross takeoff weight is provided by transition at 0.88R or 0.92R. The location 0.92R was initially selected, but further refinements revealed equivalent performance at 0.95R, which was chosen for the transition location to minimize the extent of ultra-thin airfoils for structural concerns.

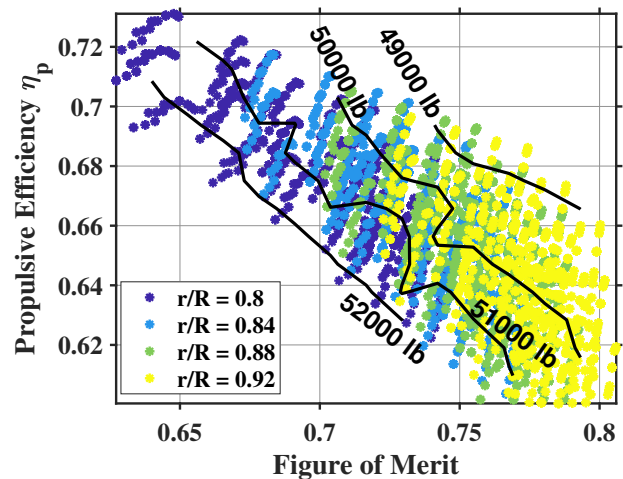


Figure 5.12: Outboard airfoil transition (7% - 5% t/c)



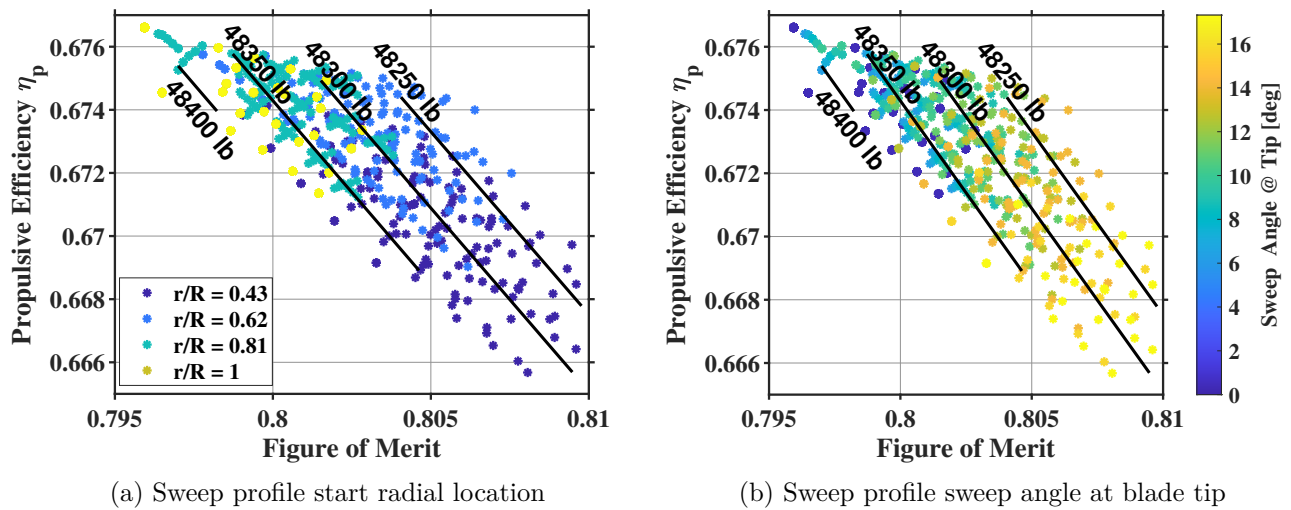


Figure 5.13: Scimitar sweep profile characteristics effect on vehicle design

### 5.3.3 Blade Sweep

Modern manufacturing has made scimitar sweep profile acceptable solution for propellers experiencing high Mach numbers. The sweep profile used in BEMT is a function of the radial start location of the sweep (shown in Figure 5.13(a)), as well as a strength which is correlated to the sweep angle at the tip (shown in Figure 5.13(b)). The variation of propulsive efficiency and Figure of Merit with sweep profile is shown in Figure 5.13, and the resulting vehicle gross takeoff weights contour lines are overlaid on the figures to help judge the design trades. Beginning the sweep at a more inboard radial station or installing a stronger sweep profile (higher tip sweep angle) reduces propulsive efficiency and increases Figure of Merit. More sweep reduces cruise performance because it leads to lower effective rotational velocities, meaning higher effective inflow ratio, and higher blade pitch angles. It also leads to a reduction in lift produced by the blade in cruise. Sweep improves hover performance because it reduces compressibility effects due to high hover tip speed. The lowest gross takeoff weight is achieved with a very slight sweep beginning at a radial station of 62% and reaching a sweep angle of 15% by the tip. However, the effect of sweep on gross takeoff weight, Figure of Merit, and propulsive efficiency is very minimal. Ultimately, the sweep was not used in the design because the benefit is minimal ( $< 0.5\%$  reduction in gross takeoff weight), while manufacturing complexity is increased and unnecessary bending torsion coupling is introduced at high thrust. Since the RPM was already low, these complexities were not warranted.

### 5.3.4 Blade Taper

Linear tip taper was considered for the blades. The variation of propulsive efficiency and Figure of Merit with taper profile is shown in Figure 5.14, and the resulting vehicle gross takeoff weights contour lines are overlaid. Taper ratio is defined as the chord at the tip divided by the chord at the taper start radial location. Figure 5.14(a) shows that a more inboard start to the taper reduces both propulsive efficiency and Figure of Merit. Figure 5.14(b) shows that Figure of Merit is improved with a lower taper ratio (more taper) while propulsive efficiency is improved with a higher taper ratio (less taper). The lowest gross takeoff weight is achieved with a 50% taper beginning at 0.96R thus it is chosen as the final design point.



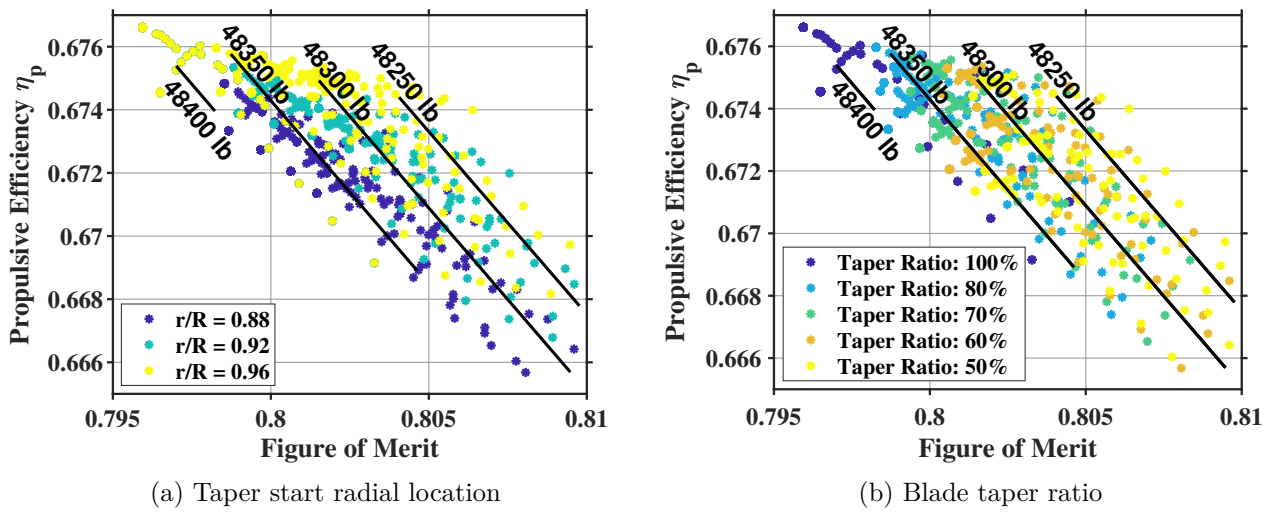


Figure 5.14: Linear taper characteristics effect on vehicle design

### 5.3.5 Blade Twist

The inboard part of the rotor has a thick airfoil and should be at very low or even slightly negative angles of attack in cruise for best performance as discussed in Section 5.2.4. To allow for lower angles of attack near the root of the blade, bilinear twist was considered. The twist transition location was varied between 40% radius and 60% radius and very little effect was found on vehicle design and rotor performance. Therefore a twist transition location at 50% radius was chosen for the design. The propulsive efficiency and Figure of Merit are plotted with varying inboard and outboard twist angles in Figure 5.15. Contour lines are overlaid on the plots showing the effect of the design trade between propulsive efficiency and Figure of Merit on vehicle gross takeoff weight. Increased twist improves Figure of Merit but propulsive efficiency is highest at around  $-20^\circ$  of twist for both the inboard and outboard region. The minimum vehicle gross takeoff weight was achieved with  $-21.9^\circ$  outboard twist and  $-19.4^\circ$  inboard twist. Reducing the twist in the last 5% of the blade to account for tip effects was also considered, however this provided only a marginal performance improvement in cruise. Hence, the bilinear twist with lowest vehicle gross weight was chosen as the final blade twist profile.

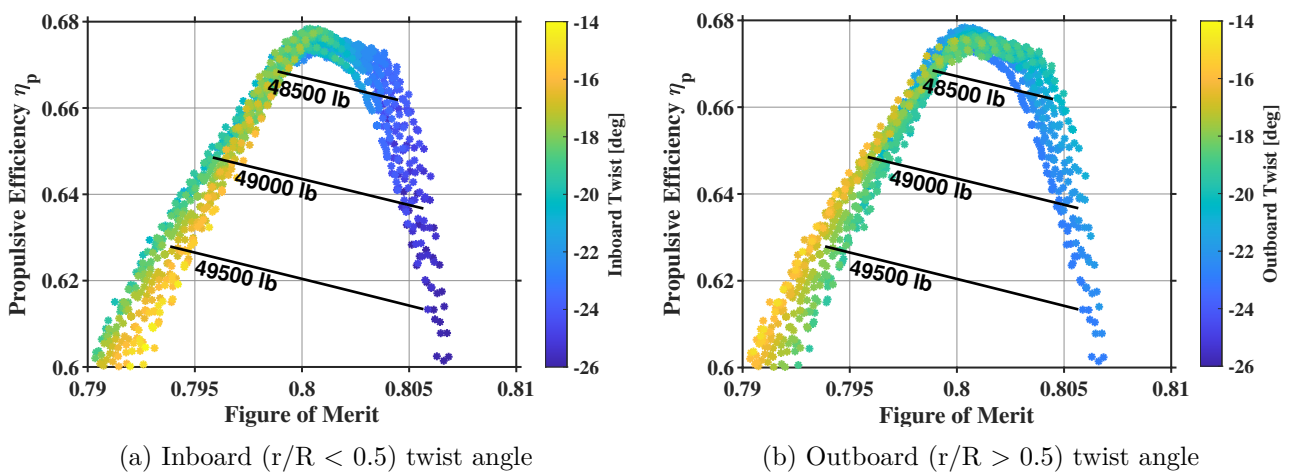


Figure 5.15: Blade bilinear twist selection



### 5.4 Rotor Sizing

With non-dimensional aerodynamic properties of the blade in hover and cruise set, trade studies on rotor sizing were conducted to choose a disk loading and number of blades. Figure 5.16 shows the variation of gross takeoff weight with disk loading and number of blades for a constant  $C_T/\sigma = 0.125$ . Figure 5.16 shows diminishing improvements in weight beyond a disk loading of  $23 \text{ lb}/\text{ft}^2$ , and increasing vehicle weight beyond a disk loading of  $25 \text{ lb}/\text{ft}^2$ . A disk loading of  $23 \text{ lb}/\text{ft}^2$  was selected to balance reducing downwash with minimizing gross takeoff weight. The GTOW decreases with number of blades hence five blades were chosen for the final design.

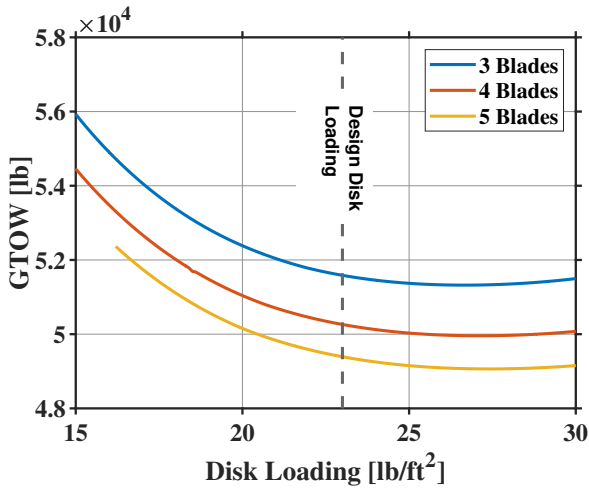


Figure 5.16: Rotor parameter selection

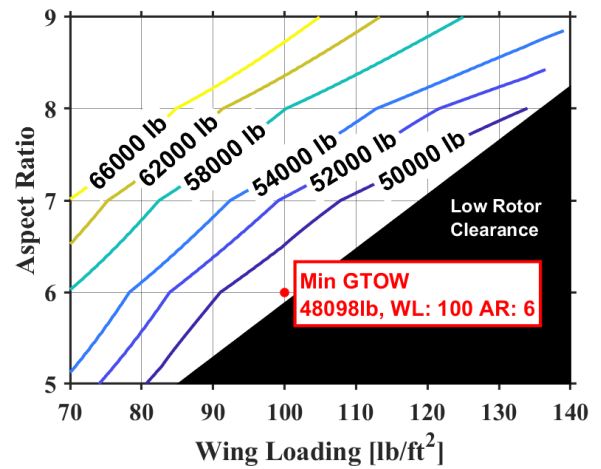


Figure 5.17: Wing parameter selection

### 5.5 Wing Sizing

To iterate wing size, the effect of wing loading on drag had to be estimated. Higher wing loading means greater wing area for the same vehicle weight and should result in increased drag. The Harris trend however, only accounts for vehicle weight, leading the code to significantly under-predict drag for low wing loading cases. To correct for this, the wing Harris factor (initially set to 0.6) was adjusted to be 10% higher at a wing loading of  $80 \text{ lb}/\text{ft}^2$  vs  $120 \text{ lb}/\text{ft}^2$ . This adjustment was determined by backing out Harris factors from wing drag using airfoil tables.

Wing sizing parameters were varied as shown in Figure 5.17. A minimum clearance between the rotor and fuselage body was set at 1.5 feet. Vehicle gross takeoff weight was reduced with increasing wing loading and decreased aspect ratio. An increase in aspect ratio for the same wing loading means increased wingspan. Since the rotors and pylon are a large tip weight, increasing wingspan results in a large increase in wing structural weight.

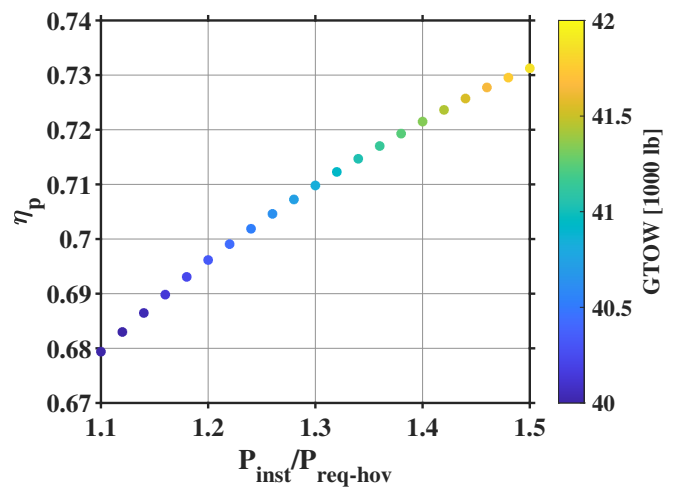


Figure 5.18: Cruise propulsive efficiency variation with turboshaft power installed. Colors indicate the resulting design GTOW.



## 5.6 Powerplant Sizing

Figure 5.18 shows the effect of installing turboshaft power greater than what is required for hover. A minimum of 110% of required power installed for hover was considered to allow for some vertical climb performance, hover at slightly higher altitudes, and to provide some margin for design. Increasing turboshaft power installed results in an improvement in propulsive efficiency due to higher  $C_T/\sigma$  in cruise, however its net effect is an increase in gross takeoff weight due to increased turboshaft, drivetrain, and structural weight. Qualitatively, turboshafts can also have a large form factor so smaller turboshafts were preferred to reduce form drag. Therefore turboshaft installed power was selected to be 110% of the minimum installed power required for hover at 2k/85°F conditions.

## 5.7 Final Tabulated Design Parameters

*Arion* is a mixed-power tiltrotor aircraft, utilizing both a prop-rotor and a turbofan for thrust in forward flight. Figure 5.19 shows the planform of the rotor blade. The final configuration specifications are summarized in Table 5.2.

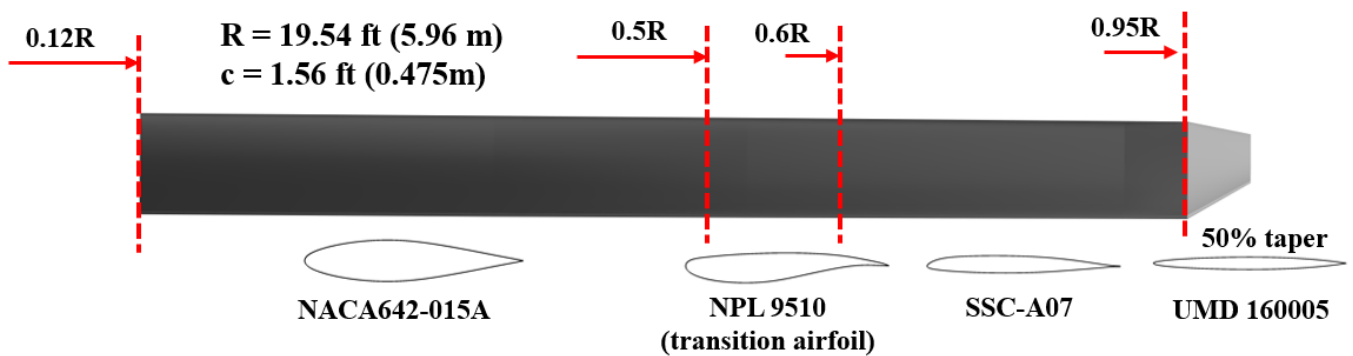


Figure 5.19: Final blade aerodynamics design

# 6 Blade Structural Design

The rotor of *Arion* is a five-bladed stiff in-plane hingeless design composed of composite materials, which are superior to metals in terms of strength-to-weight ratio and fatigue life. The blade structure was designed to achieve the stiffness distribution to carry the centrifugal forces and dynamics bending loads in flight.

## 6.1 Blade Internal Structure

The internal structure of the blade assembly was designed with adequate flap bending ( $EI_n$ ), lead-lag bending ( $EI_c$ ), torsion bending ( $GJ$ ), and axial ( $EA$ ) stiffnesses to sustain loads on the blade in flight. These loads include centrifugal, steady, and oscillatory flap, lead-lag, and torsional moments. Loads accounted for also include shear stresses resulting from aerodynamic and inertial forces. The design variables considered were: spar section dimensions, chordwise position, spar and skin thickness, and leading-edge mass. An iterative procedure was used in Section Builder, a comprehensive finite element-based code for cross-sections [19], to analyze and optimize the sectional properties.

An exploded view of the blade segment is shown in Fig. 6.1. A hollow spar is used to provide the necessary



Table 5.2: Design Parameters

Property	English	Metric
<b>Rotor System</b>		
Number of Blades		5
Disk Loading	23 <i>lb/ft</i> <sup>2</sup>	0.97 <i>kg/m</i> <sup>2</sup>
Rotor Diameter	39.08 ft	11.91 m
Chord	18.78 in	47.70 cm
Solidity		0.127
Root Cutout		12%
<b>Hover Condition</b>		
$V_{tip-hover}$	828 ft/s	252 m/s
RPM in hover		404.65
Density	0.00210485 <i>slug/ft</i> <sup>3</sup>	1.08467 <i>kg/m</i> <sup>3</sup>
Altitude (MSL)	2000 ft	610 m
Speed of Sound	1144.1 ft/s	348.7 ft/s
Tip Mach		0.724
<b>Cruise Condition</b>		
$V_{tip-cruise}$	303 ft/s	92 m/s
RPM in Cruise		148.08
Density	0.00106526 <i>slug/ft</i> <sup>3</sup>	0.548946 <i>kg/m</i> <sup>3</sup>
Altitude (MSL)	25000 ft	7620 m
Speed of Sound	1016.0 ft/s	309.7 ft/s
Tip Helical Mach		0.805
<b>Blade Design</b>		
UMD 16005 Airfoil r/R		95% - 100%
SSCA07 Transonic r/R		60% - 95%
NPL9510 Transonic r/R		50% - 60%
NACA640015 r/R		12% - 50%
NPL9510 Transonic r/R		50% - 60%
Inboard Twist		-19.4 degrees
Outboard Twist		-21.9 degrees
Twist Transition r/R		50%
Taper Ratio		50%
Taper Start r/R		95%
Figure of Merit		0.813
Propulsive Efficiency $\eta_p$		0.685
Hover $C_T/\sigma \eta_p$		0.125
<b>Wing Design</b>		
Span	53.7 ft	16.4 m
Chord	8.95 in	2.73 m
Wing Loading	100 <i>lb/ft</i> <sup>2</sup>	4.21 <i>kg/m</i> <sup>2</sup>
Aspect Ratio		6
Airfoil		DFVLR-R4 Transonic

stiffness at a relatively low cost-to-weight. The D-spar design was chosen because it offers a simple closed-section structure with high torsional rigidity. The spar extends from a chordwise position of  $0.02c$  to  $0.4c$



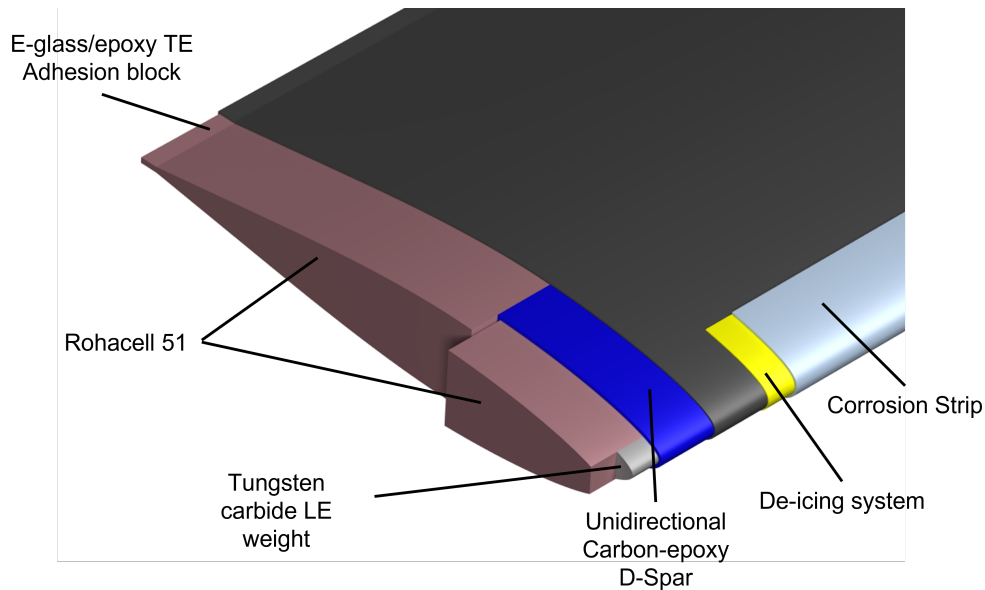


Figure 6.1: Blade internal anatomy with materials

from the leading edge. The center of gravity (CG) of the blade cross-section was placed at  $0.25c$  from the leading edge using a leading-edge tungsten carbide ballast weight to move the CG forward. Keeping the cross sectional CG at the blade aerodynamic center at the quarter chord ensures pitch-flap flutter stability. The composite skin holds the leading edge ballast weight in place in front of the D-spar. The leading edge weights are broken into 20 separate segments along the blade to ensure they do not contribute to the stiffness of the structure.

Fiber-reinforced composite materials were chosen for the blade because of their superior specific strength, excellent fatigue characteristics, and ability to conform to complex geometries. The blade skin consists of two balanced  $[\pm 45^\circ]$  plies of T300 graphite/epoxy for high torsional stiffness. The D-spar comprises unidirectional  $[\pm 0^\circ]$  plies of T300 graphite/epoxy. Rohacell 51 foam was chosen as the core material for preserving the aerodynamic contour of the blade. Rohacell 51 was chosen over the honeycomb core because Rohacell 51 has a closed cell structure reducing the need for core filling paste required to bond the edges of the honeycomb core to the skin. The lower cost and ease of machining make Rohacell foam an attractive option compared to honeycomb. Honeycomb cutting often requires extensive post-processing to conform to the skin profiles. Unlike Rohacell, cutting honeycomb to the airfoil profile often requires extensive post-processing. Lastly, the trailing edge block is made of fiberglass-reinforced epoxy. A trailing edge E-glass/epoxy block of 2% chord is added to reinforce the trailing edge of the blade and provide adequate surface area to bond the upper and lower skin.

Polyurethane protective tape 8542HS was chosen for enhanced erosion protection because of its low weight, structural conformity, and ease of repair. This tape is made from an abrasion-resistant polyurethane elastomer that resists erosion, puncture, tearing, abrasion, and ultraviolet light damage. The added flexibility it does not contribute any structural stiffness to the blade compared to metal protective sheaths (i.e., titanium, steel, or nickel). The entire blade is wrapped with a copper mesh sleeve to provide an electric current path spanwise to the hub in the event of a lightning strike, avoiding electrostatic charge build-up and damage to the blade in accordance with 14 CFR 25.581. The de-icing system used on the blade consists of a series of actuators along the leading edge between the blade skin and erosion shield. These actuators produce ultrasonic frequency distortion of the blade surface to shear off any accumulated ice; the ice detaches from the blade from centrifugal and aerodynamic forces.



## 6.2 Rotor Blade Sectional Properties

Each individual blade weighs 54.69 kg (120.6 lb). The weight of the 10 rotor blades 546.9 kg (1,206.0 lb). Figures 6.2(a) through 6.2(d) show the non-dimensional mass and stiffness distribution of the blades. The rotor has a 12% span root cut-out. The hub connection to the flexbeam begins at 2% span and the blade connection to flexbeam begins at 6% span, therefore the stiffness and mass properties within this region are dominated by the connecting materials, which is signified by a jump in the non-dimensional stiffnesses. Outboard of the root cutout, the skin, spar, and leading edge weights contribute to the sectional properties and spanwise variations are observed due to the change in airfoil cross-section and blade taper. The discrete changes in the sectional properties are a result of ply drop-offs at each transition zone.

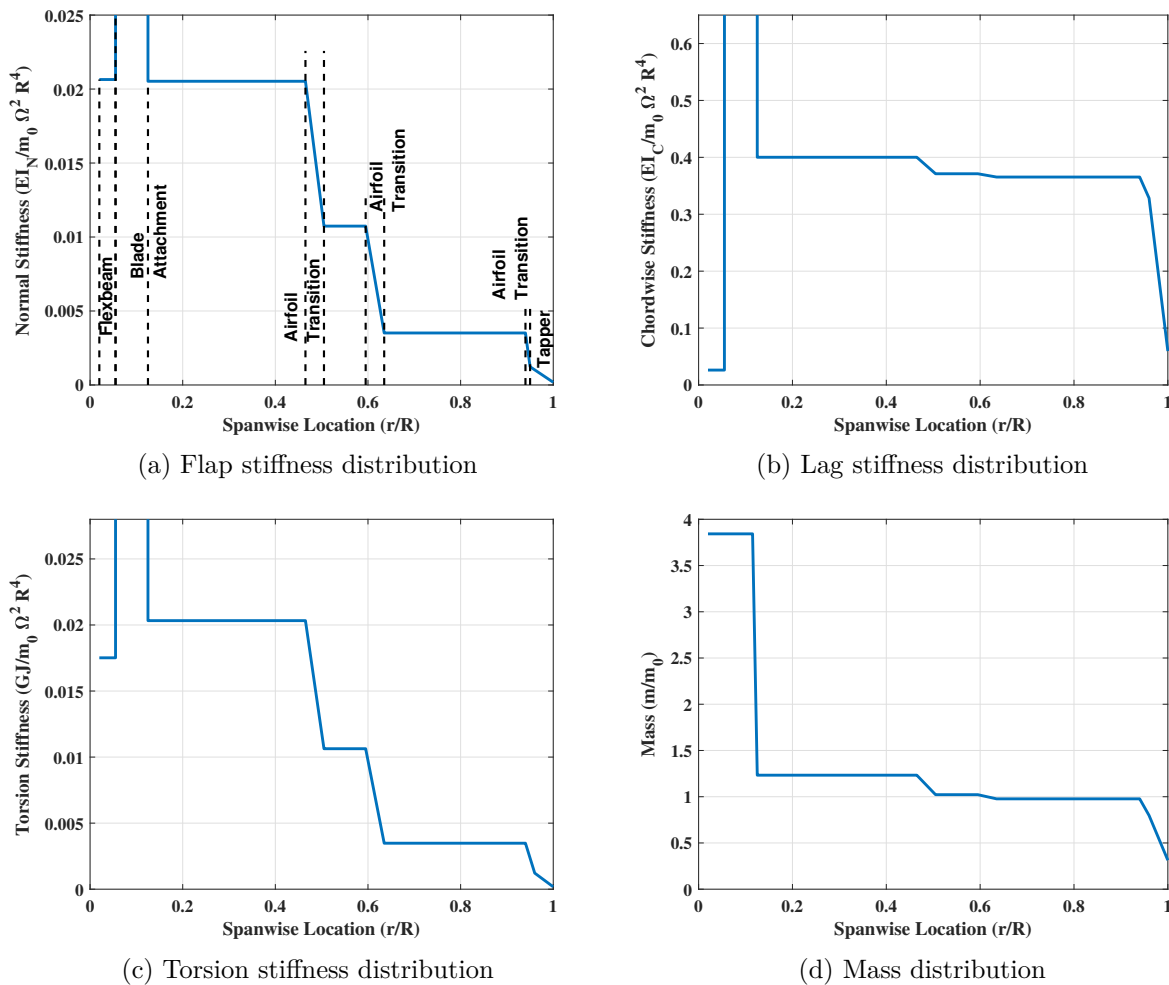


Figure 6.2: Rotor Blade Sectional Properties

Fan plots of the rotor blade are shown in Fig. 6.3, one each for hover and cruise. The variation in collective between hover and cruise is  $13.66^\circ$  to  $74.06^\circ$ . As the blades pitch up, flap becomes stiffer and lag softer. Due to the blade twist, the modes are highly coupled. The dominant mode is listed first. The plots show that the blade natural frequencies are well separated from  $1/\text{rev}$  harmonics at the operating conditions. Necessary torsional stiffness is achieved through added pitch link stiffness, resulting in a fundamental torsion frequency of  $5.7/\text{rev}$ . In the transition from helicopter to airplane mode, it is necessary to cross several resonant frequencies. Therefore, the reduction in RPM is initiated after the pylons are fully tilted to airplane mode to reduce oscillatory loading. The drop in RPM is performed quickly via the two-speed



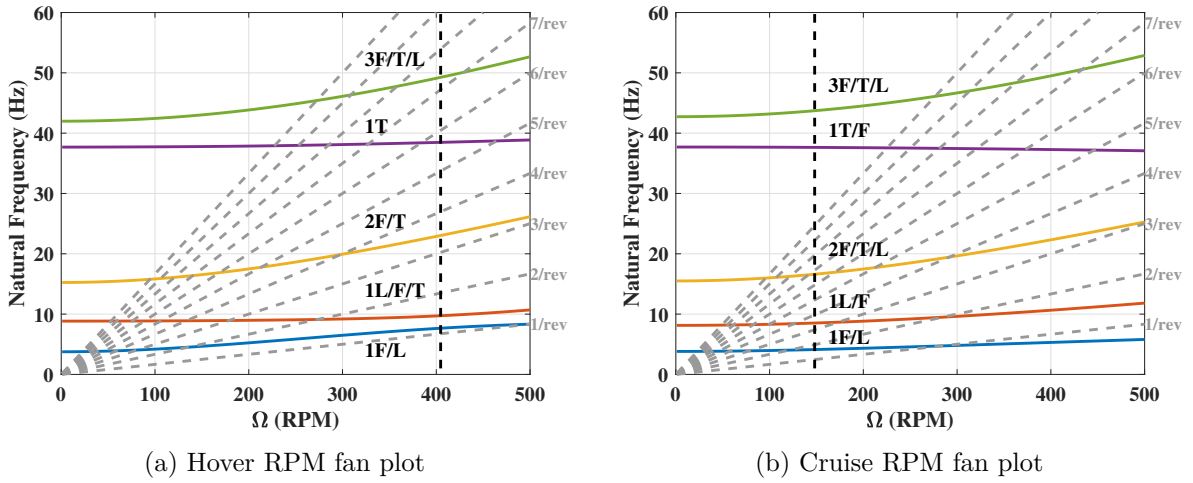


Figure 6.3: Fan plots showing first five rotor frequencies at hover and cruise RPM

Table 6.1: Hover RPM natural frequencies

Frequency (/rev)	Hover 405 RPM
1st Flap/Lag	1.14
1st Lag/Flap/Torsion	1.44
2nd Flap/Torsion	3.42
1st Torsion	5.70
3rd Flap/Torsion/Lag	7.30

Table 6.2: Cruise RPM natural frequencies

Frequency (/rev)	Cruise 148 RPM
1st Flap/Lag	1.67
1st Lag/Flap	3.45
2nd Flap/Torsion/Lag	6.73
1st Torsion/Flap	15.25
3rd Flap/Torsion/Lag	17.72

transmission to minimize the impact of these adverse operating conditions. The mechanisms to achieve this are discussed in detail in section 10.

### 6.3 Blade Manufacturing

The rotor blades are manufactured in two steps. The spar is manufactured separately using a solid mandrel assembly, which defines its internal geometry, including its restraining surface. The ballast tungsten weights are placed to flush with the spar, and Rohacell is placed behind the spar. The entire assembly is wrapped with graphite/epoxy cloth to contain the structure tightly. Automated fiber placement is used to better capture the complex geometry of the blade due to twist, taper, sweep, and anhedral. Gradual ply drop-off zones were added in the blade's cross-section transition zones to ensure continuous fibers along the span of the blade. Finally, the spar is cured in a specialized mold that perfectly captures the geometry. The erosion protection tape and de-icing layer are implemented in this step to complete the outer blade assembly. Transition in airfoil geometry, and the skin transition region, draping techniques are employed appropriately to ensure a wrinkle and deformity free product. A mold is produced with a shallow indent on the leading edge for the stainless steel strip. Final curing is achieved in an autoclave.

### 6.4 Aeroelastic Stability Analysis

Aeroelastic stability analysis was performed to ensure stability margins for *Arion*. Pitch-flap and flap-lag couplings were considered throughout the design of the rotor by eigen-analysis. Stability boundaries were identified using appropriate mass, damping, and stiffness properties of the rotor itself.



Flap-Lag flutter arises from Coriolis and structural coupling. High inflow is an important factor (requiring  $\delta_3$  for gimbaled hubs to separate flap and lag frequencies). Generally, rotors that are stiff in both flap and lag are susceptible to this phenomenon. Stability analysis of the blades showed stability in both hover and cruise operating conditions. Due to the twist of *Arion* blades, further analysis was carried out to identify the boundaries of this instability and ensure adequate margins. Figure 6.4 shows the flap-lag flutter boundary at hover conditions in the form of egg plots with increasing blade loading at a representative twist rate of  $-21^\circ$ . Lag dampers are difficult to incorporate in hingeless hubs, therefore natural stability is crucial. No flutter boundary exists at any operating blade loading and the rotor would stall in edgewise flight before this instability is reached. In cruise mode, the aerodynamic lag damping increases significantly and no flutter boundary exists at all. Figure 6.5(a) shows the eigenvalues obtained at the design frequencies. *Arion* is free of flap-lag flutter in all operating conditions.

Pitch-flap coupling was analyzed to ensure the blades are free from pitch divergence and pitch-flap flutter. These boundaries can be seen in Fig. 6.5(b). Pitch divergence is a static instability resulting from coupling between lift and centrifugal force. Offset between these forces induces a twisting motion of the blade that may cause failure. The location of the elastic axis is unimportant. Pitch-flap flutter is the dynamic instability from lift and centrifugal coupling about the pitch axis. The best way to mitigate this is to ensure the blade center of gravity and pitch axis are in line with the aerodynamic center. Therefore, the rotor blade pitch axis and C.G. are placed at quarter chord. A high fundamental torsional frequency further increases this stability margin.

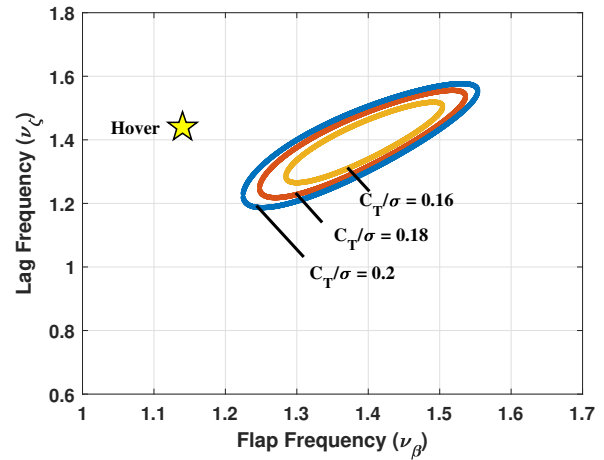
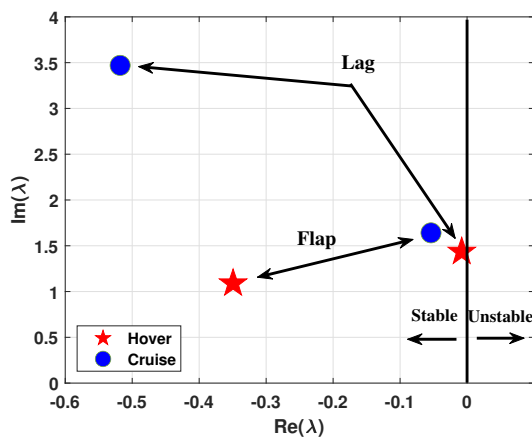
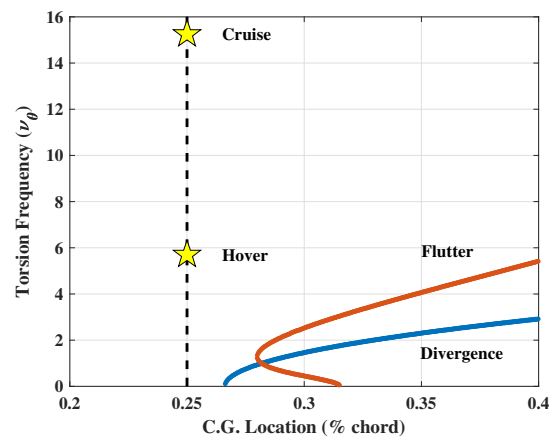


Figure 6.4: Flap-lag flutter boundaries at  $\theta_{tw} = -21^\circ$  with increasing blade loading



(a) Flap-Lag eigenvalues in hover and cruise



(b) Pitch divergence and flutter boundary

Figure 6.5: Flap-lag and pitch-flap stability margins

### 6.4.1 Ground Resonance

Because *Arion* has a stiff in-plane rotor ( $\nu_\zeta > 1$  /rev), it is free from ground resonance with no need for additional lag dampers.



### 6.4.2 Whirl Flutter

Whirl flutter is a critical instability for high-speed tiltrotors. *Arion* is designed to be flutter-free at 450 kts cruise. The use of hingeless hub and careful placement of rotor-pylon c.g. helps to achieve a flutter-free flight for the given mission. A comprehensive whirl flutter analysis was carried out using UMARC-II [20,21] to verify the design. UMARC-II is a multi-body aeromechanics solver that can model the rotor, wing, and the pylon with element beams and joints.

Figure 6.6 shows the coupled frequency and damping predictions as a function of airspeed at 2000 ft altitude. The wing beam, chord, and torsion modes are labeled in each figure. Only the important modes are shown. Wing beam mode damping shows a peak at 320 kts and decreases thereafter due to interaction with the regressive flap mode as shown in Figure 6.6(b). Wing chord mode damping is the least damped of all and shows an increase with airspeed. This is because the wing is very stiff in chord direction and the chord mode does not interact with dominant rotor modes; therefore it does not present a danger for whirl flutter. The wing torsion mode damping increases until 350 kts and starts to drop thereafter.

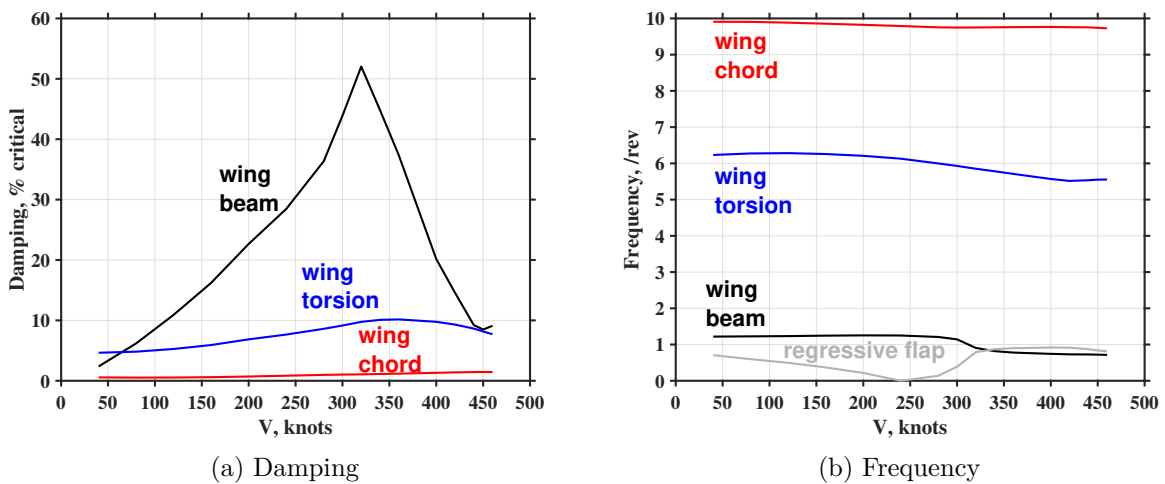


Figure 6.6: Whirl flutter stability analysis of coupled modes at 2000 ft

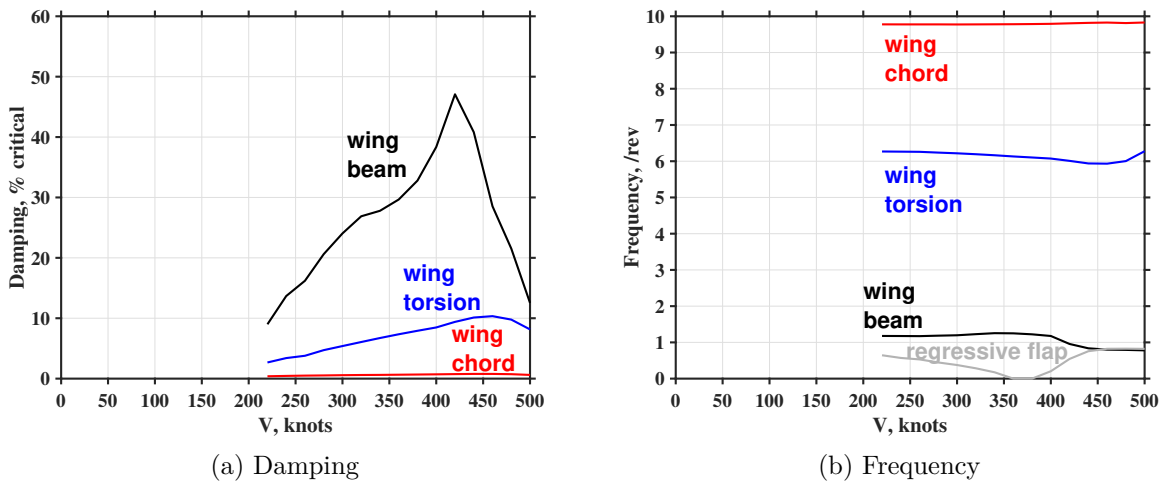


Figure 6.7: Whirl flutter stability analysis of coupled modes at 27,000 ft

Figure 6.7 shows the frequency and damping predictions as a function of airspeed at the cruise altitude of



27,000 ft. Similar conclusions to the predictions of 2000 ft can be drawn. The difference is that instability speed is significantly higher at high altitude. At the cruise speed of 450 kts, the beam and torsion modes have damping greater than 10%, while the chord mode has about 3%. This is sufficient for flutter-free flight (Boeing M222 aircraft had only 1.7% damping at 355.6 kmph (221 mph)) [22]. In addition, these damping predictions do not include any structural damping which would further stabilize the system.

The reason for high stability is high non-dimensional wing frequencies, placement of turbofans on the fuselage and turboshafts inboard of the wing, and the stiff in-plane hingeless hub. The wing non-dimensional frequencies are high because of the low rotor speed achieved with the two-speed transmission. Placement of the turbofans and turboshafts reduces wing beam/torsion coupling and helps keep the frequencies high with the same wing stiffness/weight. Hingeless hubs have better flutter characteristics than gimbaled/articulated hub and a stiff in-plane hingeless hub does not suffer from air resonance, which is another critical instability that is seen with tiltrotors.

## 6.5 3-D Stress Analysis

A detailed three-dimensional structural analysis of the blade was performed using the US Army/University of Maryland solver X3D [23] to provide guidance on hub and internal structure design and stress-check for ultra-thin tip. This solver uses three-dimensional (3D) finite elements to model the structure from first principles and capture the dynamic stresses. The objective was to capture the stress concentrations at both root and thin cross-sections near the tip and ensure that an acceptable factor of safety was maintained particularly at the thin tip where interlaminar stresses could lead to delamination. The analysis was conducted at different flight conditions, but the results are only shown for the hover RPM at a collective of 13.66 degrees where maximum concentration was encountered at the root.

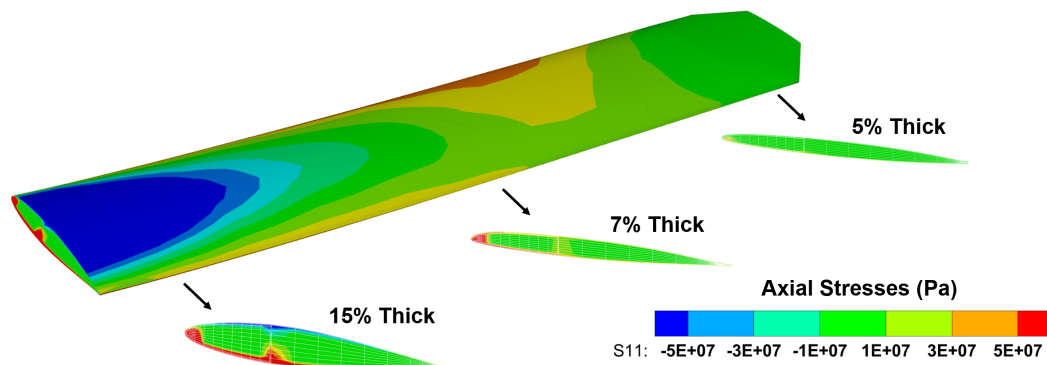


Figure 6.8: Axial stress distribution of *Arion* blade in hover,  $C_T/\sigma = 0.12$ .

Figure 6.8 shows the axial (bending) stress distribution along the blade. Three cross-sections are highlighted at 15% R, 75% R, and 90% R. These cross-sections correspond to three different airfoils, with the outboard one being the thinnest. The highest stresses understandably occur near the root. Zooming into this area, high compressive stresses are observed on the top surface, with the bottom surface having high tensile stress. There is some tensile stress concentration at the top surface of the blade near mid-span due to the blade pre-cone ( $3^\circ$ ). The maximum tensile stress in the spar is approximately 400 MPa, which gives a factor of safety over 4. The stresses in the 5% thick airfoil near the tip are well within limits, providing a safety factor of 8.

To summarize, the rotor blade of *Arion* was designed to achieve the targeted frequencies and free from all aeroelastic instabilities. A high-fidelity 3D analysis was performed to guide structural (hub) and aerodynamic (tip) design.



## 7 Hub Design

Current tiltrotors employ a gimbaled hub. Hub loads in edgewise and transition flight are greatly reduced because the gimbal allows the blades to flap freely. A pitch link offset angle  $-\delta_3$  introduces kinematic pitch-flap coupling which helps separate the lag frequency from flap and allows for stable axial flight up to the whirl flutter boundary [24]. However, the gimbaled hub can be bulky and complex. Higher number of blades cannot be accommodated due to the high  $-\delta_3$  requirement. Five blades are desired to increase solidity and maximize  $C_T$  in hover and transition. They also reduce vibration in cruise from blade passage. Therefore, a different hub type was considered that would enable flutter-free flight up to 450 kts, have no flap-lag instability without  $\delta_3$ , and still have manageable loads. Modern 3-D analysis and materials produced such a hub.

### 7.1 Hub Selection

Larger hubs increase nacelle size and hub drag, significantly hindering performance. With a design cruise speed of 450 kts, minimizing hub drag is imperative. A high collective range is also necessary to achieve collective targets in cruise, enabling increased propulsive efficiency. Lastly, a higher number of blades is desired relative to conventional tiltrotors to maximize thrust production in hover and transition while distributing the forcing, reducing vibratory loading. The available space around the hub becomes a limiting factor.

With two main rotors, cyclic controls are required to achieve adequate control authority in all flight conditions. A cyclic-capable swashplate adds size and complexity to the hub. An articulated hub will yield the most complex and least compact design, maximizing the size required of the nacelle. A bearingless configuration will not enable the collective range necessary to achieve reasonable propulsive efficiency in forward flight. A gimbaled hub would minimize the loading in transition. It is possible to design a gimbaled hub with more than three blades but the required  $-\delta_3$  angle for high-speed forward flight will force the placement of the pitch links further from the hub center. This will significantly increase the size of the hub resulting in higher drag in cruise. A hingeless hub is the simplest to design and the most compact, but comes with the highest loads in transition. However, the minimization of hub drag in forward flight is crucial. Therefore, a hingeless hub is selected to minimize drag understanding the transition to and from axial flight must be rapid to reduce the time under adverse loading. Lastly, whirl flutter is the key barrier to achieve high-speed forward flight for tiltrotors. The Boeing Vertol company developed a hingeless tiltrotor hub in the 1970s and conducted tests in the  $40 \times 80$  ft. wind tunnel at NASA Ames [22]. The test data shows their design was free of aeroelastic instability at high speeds [25]. Therefore, a similar target for the 1st flap frequency target was chosen at 1.14/rev for *Arion*. A stiff in-plane configuration is desired to avoid ground resonance concerns. Higher lag frequency will result in higher loads in transition. However, it is difficult to design a cross section that yields a lower lag frequency, still over 1/rev, that can withstand the stresses experienced in edgewise flight. Therefore, the target for 1st lag frequency is selected as 1.5/rev so a larger flexbeam can be designed to reduce stress on the hub.

### 7.2 Hub Assembly

The hub assembly is shown in Fig. 7.1. Titanium, steel, and aluminum alloys were considered alongside fiberglass and carbon fiber composites for the flexbeam, shown in yellow. The design and material selection for the flexbeam drives frequency placement and must safely transmit loading to the rotor mast. Of the materials considered, titanium has the best fatigue resistance. Composite materials tend to fail abruptly with little warning which makes titanium ideal for the cyclic nature of loads the hub encounters, ensuring long operational life for the customer. High Modulus of Elasticity allows for a smaller cross section to



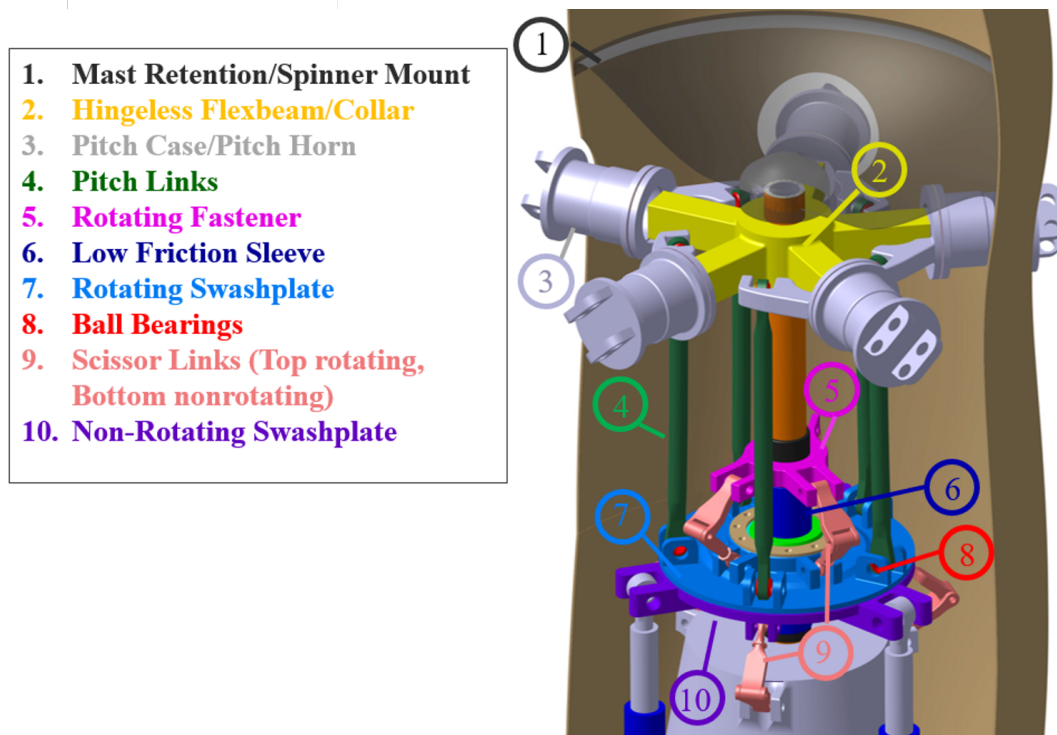


Figure 7.1: Hub assembly

achieve the same target stiffness, reducing the size of the nacelle. Titanium is also highly resistant to corrosion, allowing for operations in a wide range of environments vital for meeting “critical military needs in highly-contested environments”. Thus, the Ti-6Al-4V alloy is selected for the flexbeam. The flexbeam is sized through iterative dynamic analysis to meet the desired frequency targets. The resulting cross section is rectangular with a width of 3.25 in (8.26 cm) and a height of 2.875 in (7.30 cm).

The pitch cases have an angular spacing of  $72^\circ$ , with pitch horns designed for a compact nacelle. The pitch cases themselves are also Ti-6Al-4V. The pitch case houses the bearing stackup and contains steel thrust and needle roller bearings to appropriately transfer forces and moments from the rotor blade to the flexbeam. Shoulder bolts are sized to connect the blade grip at the end of the pitch case securely to the blade.

### 7.3 Swashplate Design

The swash plate must provide full collective and cyclic control to provide adequate control authority in hover and transition. Three hydraulic actuators with triple redundancy lines provide control to the non-rotating swashplate with  $\pm 3.64$  in (9.25 cm) of stroke. The non-rotating swashplate is held in place with scissor links attached to the transmission casing, and is allowed to roll over cylindrical bearings shown in 7.2(a). The rotating swashplate is forced to rotate via scissor links to a rotating fastener, thus alleviating bending loads on the pitch links. This configuration ensures easier maintenance and replacement than a splined drive tube/gimbal ring system in use on the V-22, allowing for *Arion* to remain operational in critical military environments for a longer period of time.

The pitch links have spherical ball bearings, with ample room to rotate shown in 7.2(b), thus allowing for the full  $80^\circ$  collective range required for *Arion* efficient cruise and hover operations. The pitch links are made of Ti-6Al-4V, maximizing strength in fatigue, bending, and buckling.



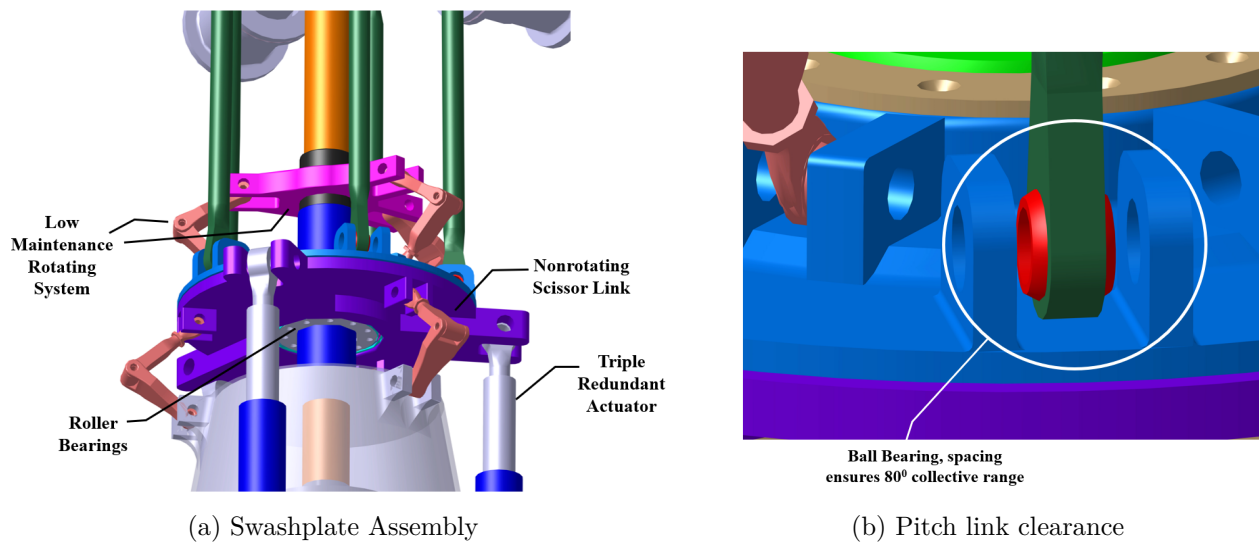


Figure 7.2: In-depth component details of the hub and swashplate assemblies

## 8 Wing and Pylon Design

The wing provides lift required to sustain level flight in airplane mode. Wing sizing was described in Section 5.5 and a corresponding aspect ratio and wing loading were selected. However, unlike all HSVTOL, the *Arion* cruise warrants detailed investigation in the wing design. For most tiltrotors, wings must carry the proprotor, engine, and fuel, thus are 20-25% thick. However, at 450 kts, delaying the drag divergence Mach number is a priority. While the wing must be capable of mitigating drag effects at high Mach numbers, it must also provide adequate lift with sufficient stall margins at low speeds. In addition, the structural design has to withstand a 3.5g limit load factor with a factor of safety of 1.5 in accordance with FAR regulations. Aeroelastic instabilities at high cruise speeds are common amongst tiltrotors as the rotor fixed frame frequencies coalesce with the wing frequencies. This instability is known as whirl flutter. This section confronts the limitations of wing design in current tiltrotors and provides detailed descriptions of how *Arion's* wing was designed.

### 8.1 Wing Aerodynamic Design

The aerodynamic design focused on: airfoil geometry, wing span, wing aspect ratio, wing dihedral, wing vertical offset, wing sweep, and incidence angle. The wing span and aspect ratio were obtained from the sizing.

#### 8.1.1 Lift Requirements

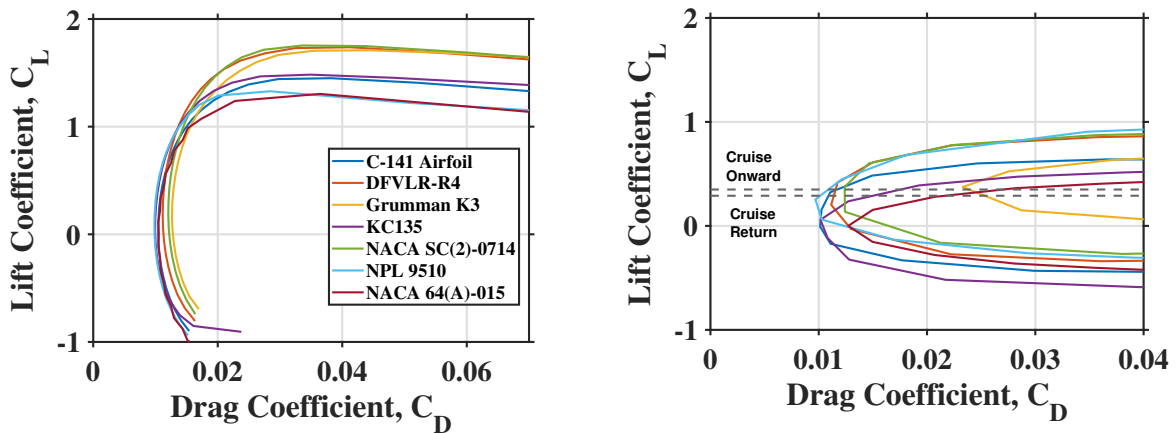
In cruise, the wing will provide sufficient lift to sustain level flight. During onward cruise and HSP, the main wing must provide lift coefficients of 0.352 and 0.162, respectively. Likewise, the lift coefficients required during the return cruise and HSP segments are 0.297 and 0.135. The *Arion* will operate in airplane mode during cruise and high-speed penetration (HSP) segments. During transition to forward flight, rotors will provide supplemental lift.



### 8.1.2 Wing Airfoil Selection

The wing airfoil selection was based on the following: (a) the  $C_L$  requirements in cruise and high speed penetration segments, (b) delay the drag divergence Mach number, and (c) widen the drag bucket range surrounding the operating cruise  $C_L$ . Additional considerations were given to using airfoils with high section thickness-to-chord ( $t/c$ ) ratio to improve torsional stiffness and assist in preventing whirl flutter instabilities. However, after initial simulations with a 13% thick M2222 airfoil at cruise altitude, whirl flutter proved not to be a factor.

A wide range of airfoils were investigated for the wing. NACA airfoils, such as the NACA SC(2)-0714 and NACA 64(A)-015, and common airfoils like the C-141, Grumman K3, DFVLR-R4, and KC135 developed by Lockheed Martin, Northrup Grumman, Airbus, and Boeing, respectively, were selected as potential candidates for the wing section. A drag bucket at the cruise Mach number is shown in Figure 8.1(b). Based on the required lift, three airfoils were selected as desirable based on the ability to minimize drag in cruise: (1) NPL9510, (2) C-141, and (3) DFVLR-R4. Additionally, part of the wing airfoil selection criteria is the ability for an airfoil to prevent stall at low speeds, hence preventing the need for the rotor to produce any vertical thrust. This requires an airfoil to have a high  $C_{L,max}$  at low speeds. Figure 8.1(a) illustrates the DFVLR-R4 airfoil is capable of obtaining the largest lift coefficient among all airfoils. This airfoil provides a shallow drag bucket compared to the other airfoils, allowing for low drag over a wide range of flight conditions, thus it was selected for the wing section.



(a)  $C_d$  vs  $C_l$  at forward speed of Mach 0.3

(b)  $C_d$  vs  $C_l$  at cruise speed with no wing sweep

Figure 8.1: Airfoil Performance Curves calculated using in-house 2D CFD solver

### 8.1.3 Wing Geometric Parameters

Most aircraft rely on sweep for delaying compressibility effects and adjusting the aircraft center of gravity. A rearward sweep would require the proprotor to sit on an extended shaft, far ahead of the wing to prevent the rotor from striking the wing. With the size of the Arion rotors, this becomes quite unfeasible to justify from a complexity and aerodynamic point of view. However, forward sweep is possible and is analyzed in this study. Forward sweep is common in tiltrotors to allow clearance for blade flapping when gimbaled hubs are used. The Arion utilizes hingeless hubs for whirl flutter considerations, but as an additional benefit, forward sweep is not needed for blade flapping clearance. Instead enough clearance between the hub plane and wing is given by the extended rotor mast in the pylon during airplane mode. Figure 8.2 highlights a forward sweep  $11^\circ$  allows for a 4% improvement in 2-D wing drag. However, under this degree of forward sweep, stability concerns arise, especially at high cruise speeds. The structural complexity and



compromised maneuverability outweighs the small drag reduction. Five blades also reduces the vibratory loads stemming from wing pylon interactions since 3/rev loadings are more severe than 5/rev.

The wing is placed above the fuselage. This offers several benefits, mainly easing the loading and unloading of cargo and providing safer operations for ground crew. A cross shaft connecting the two turbo shaft engines for the case of OEI, as well as electric wiring and fuel, pass through the wing easily. Placing the wing on top increases cabin space and prevents the load carrying cross shafts from passing through the cabin. Finally, top mounting the places the proprotors higher, increasing safety during ground operations. The wing is placed 2.1 ft above and 1.94 ft ahead of the vehicle CG to ensure sufficient CG range is possible.

To generate equal thrust in cruise, the rotors are spaced equally from the center of gravity. This distance, along with a clearance of 2 ft between the rotor tip and fuselage, and fuselage width contribute to the wing span. The wing incidence angle was set based on the required lift for cruise. The required lift in cruise comes at a wing angle of incidence of  $-0.34^\circ$  with respect to the freestream.

Twist rates and tapering of wings are often used to reduced induced drag by giving closer to an elliptical lift along the span. However, for tiltrotors, justifying these geometric variations are not as easy. With proprotors at the tip of the wing, high structural stiffness is required, which is compromised by taper. The downwash from the contracted wake of the proprotors increases the dynamic pressure on the outboard section of the wing, altering the lift distribution anyway. The effect of downwash on the outboard sections of the wing means that the chord line of a twisted wing tip will not align with the prop thrust vector. This adds unnecessary complexity of manufacturing with no gain in aerodynamic performance. For these reasons, the Arion wing has no twist or taper.

The wing is designed with flaperons which are sized based on download in hover. The flaperon is located over the trailing edge of the main wing, covering 30% of the wing chord. The flaperons increase the effective camber and chord of the wing, allowing for a reduced stall speeds and pitch angles during slow flight, which gives the pilot more flexibility and safety margin during conversions. Figure 8.3 shows the flap angle versus stall speed at different atmospheric conditions. An estimation for lift provided by flaps based on Glauert's simple flap model [26] shows an in  $C_{l,max}$  of 0.54 and a maximum increase in  $C_{l,max}$  of 1.5 when the flaps are deployed. However, flaps generate considerable amounts of drag, therefore large deflection angles are not utilized in airplane mode.

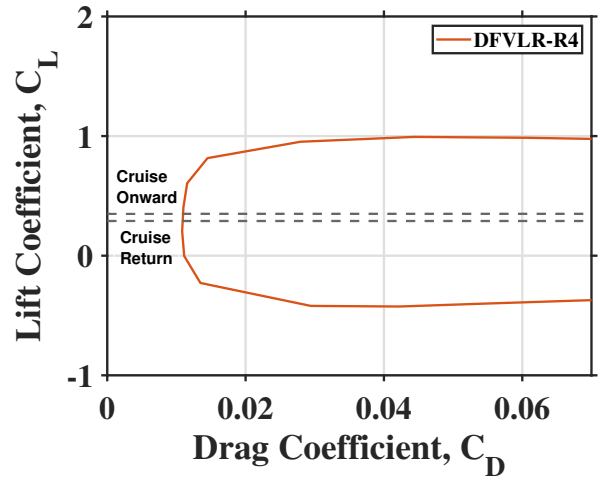


Figure 8.2:  $C_d$  vs  $C_l$  at cruise speed with  $11^\circ$  sweep

The required lift in cruise comes at a wing angle of incidence of  $-0.34^\circ$  with respect to the freestream.

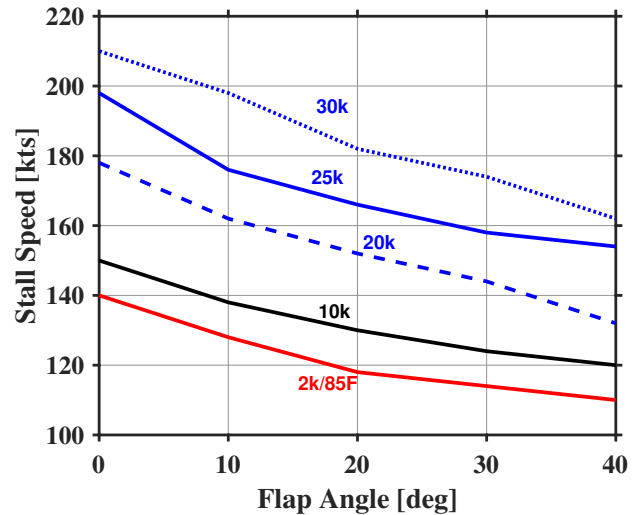


Figure 8.3: Stall Speed Varying with Flap Deflection at Different Altitudes and ISA conditions



Once the wing airfoil was selected an in-house 3-D RANS CFD solver was used to understand the flowfield surrounding the wing at difficult conditions throughout the mission profile. During cruise, the wing is at an angle of attack of  $-0.34^\circ$ . At this speed, 3D effects are relatively small, with induced drag having a minimal effect on the airfoil performance. While wing tip vortices are present, the induced drag is relatively small compared to the wing drag, leading to a high Oswald efficiency factor. At higher angles of attack, 3D effects become important and the performance decreases significantly as expected of a supercritical airfoil. These results are critical to performance calculations in Section 13. The visualization of the wake of the wings and their interactions can be seen in Figure 8.4(a). As shown in Figures 8.4(c) and 8.4(d), flow separation is not a concern in cruise or during high-speed penetration, as the flow remains attached to the wing as it accelerates around the leading edge curvature. These results confirmed the supercritical wing is suitable for all mission segments, and performs exceptionally well in cruise. At low speeds, when the the angle of attack of the wing is higher to generate more lift, larger vortices will be generated. Therefore, lift should be generated by a combination of vertical thrust provided by the rotor and wing lift at low speeds to prevent operating at high wing incidence angles.

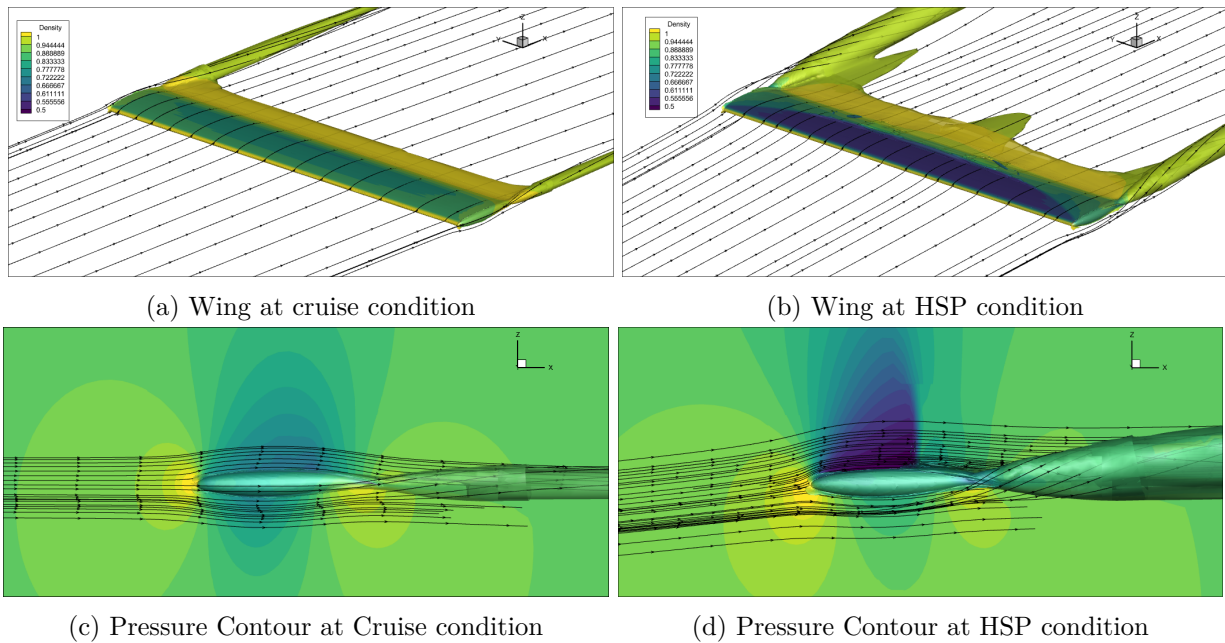


Figure 8.4: Main wing pressure distribution with wing-tip vortices and flowlines at  $-0.4^\circ$  and  $5^\circ$  AOA

## 8.2 Wing Structural Design

The wing comprises a single-cell continuous torque box between wing tips. Unlike conventional fixed-wing aircraft, the wings of tilt rotors are typically sized to meet stiffness requirements, not strength requirements. The torque box was designed to provide the necessary bending and chordwise stiffness to delay the onset of whirl flutter and to support the structural and aerodynamic loading. A closed cross-section box spar is chosen to provide adequate torsional stiffness to delay air resonance.

### 8.2.1 Wing Structural Design

Initial sizing of the wing torque box was determined using the methods presented in [27]. The required wing stiffness is determined by scaling the frequencies of a reference tiltrotor, XV-15, to our vehicle. The material properties and area moments required to achieve the desired stiffness were then estimated. The



method assumes the torque box has a constant cross-section and uniform wall thickness. The area moments of inertia are determined by approximating the torque box's geometry as a trapezoid. Once a baseline was established, Section Builder [19] was used to model the wing cross-section using finite element analysis. The optimum values of the design variables are as follows: flap bending stiffness  $18 \times 10^9$  lb-in<sup>2</sup> (52 MPa), in-plane bending stiffness  $1 \times 10^{12}$  lb-in<sup>2</sup> (3426 MPa), torsion stiffness  $15 \times 10^9$  lb-in<sup>2</sup> (46 MPa), and axial stiffness  $1 \times 10^{12}$  lb-in<sup>2</sup> (2962 MPa). The mass per unit length of the torque box is 28 lb/ft (42 kg/m). Using the method proposed by [27] for estimating the mass of control surfaces and fittings for tiltrotor wings, an overhead of 17 lb/ft (25 kg/m) to make the total mass per unit length of the wing to be 45 lb/ft 67 kg/m.

### 8.2.2 Wing Jump Take-off Loads

The common maneuver of a highly-accelerated vertical takeoff is often used to avoid dangerous situations. The maneuver results in a high load factor acting at the wing tip. An Euler-Bernoulli beam bending analysis of the wing was completed to determine the wing stiffness required to sustain a jump take-off maneuver. The results show that a wing stiffness of  $1.31 \times 10^9$  lb-in<sup>2</sup> ( $3.76 \times 10^6$  N-m<sup>2</sup>) is required to sustain a 3.5g load at the tip with a safety factor of 1.5. Comparing the required wing stiffness to Arion's actual wing stiffness of  $18.0 \times 10^9$  lb-in<sup>2</sup> ( $51.7 \times 10^6$  N-m<sup>2</sup>), demonstrates that Arion is capable of sustaining the prescribed jump take-off load; however, the wing stiffness is not over-engineered either. Instead, the results demonstrate that whirl flutter mitigation is the driving criterion for wing stiffness.

### 8.2.3 Wing Structure

The analysis placed the front spar at 0.07c and the rear at 0.55c. Because the wing has a 13% thickness-to-chord ratio with a maximum thickness of 0.40c, the torque box has a characteristically large lag stiffness compared to the flap stiffness. This design also provides space for the fuel tank between the spars and the rear spar for supporting actuators, drive shaft, and flaps. The spar webs meet the spar caps for I-beams to achieve adequate chordwise bending stiffness. No cutouts are present within the torque box because this destroys the continuity of shear flow. Cutouts for the interconnecting shaft, electric, and hydraulic lines are on the ribs.

### 8.2.4 Wing Material Selection

T300/5208 graphite-epoxy composite was chosen for the construction of the torque box because it met the high material stiffness requirements of the design while providing a 34% reduction in weight, thereby significantly reducing the empty weight of the aircraft. The torque-box skin is a balanced and symmetric laminate with 10% [0°] plies, 80% [ $\pm 45^\circ$ ] plies, and 10% [90°] plies. The wing-spar caps are 85% [0°] plies and 15% [ $\pm 45^\circ$ ] plies. This layup follows the rules of thumb proposed by Kassapoglou [28]. This design also protects against unforeseen secondary load cases that might lead to premature failure.

The wing is constructed as one long continuous unit from nacelle to nacelle. Prefabricated molds of the wing structure are used to house the reinforced graphite fiber layers along with the preformed assemblies of the spar cap sections. Mandrels within the mold are used to shape the internal geometry of the torque box and then cured. Given that composite materials are poor conductors of electricity, an aluminum mesh is applied to the outermost ply of the wing to prevent damage to the structure in the event of a lightning strike. *Arion* can fly at high altitudes and possibly cold environments. A thermal-based anti-icing system was selected to ensure no ice forms along the wings leading edge.



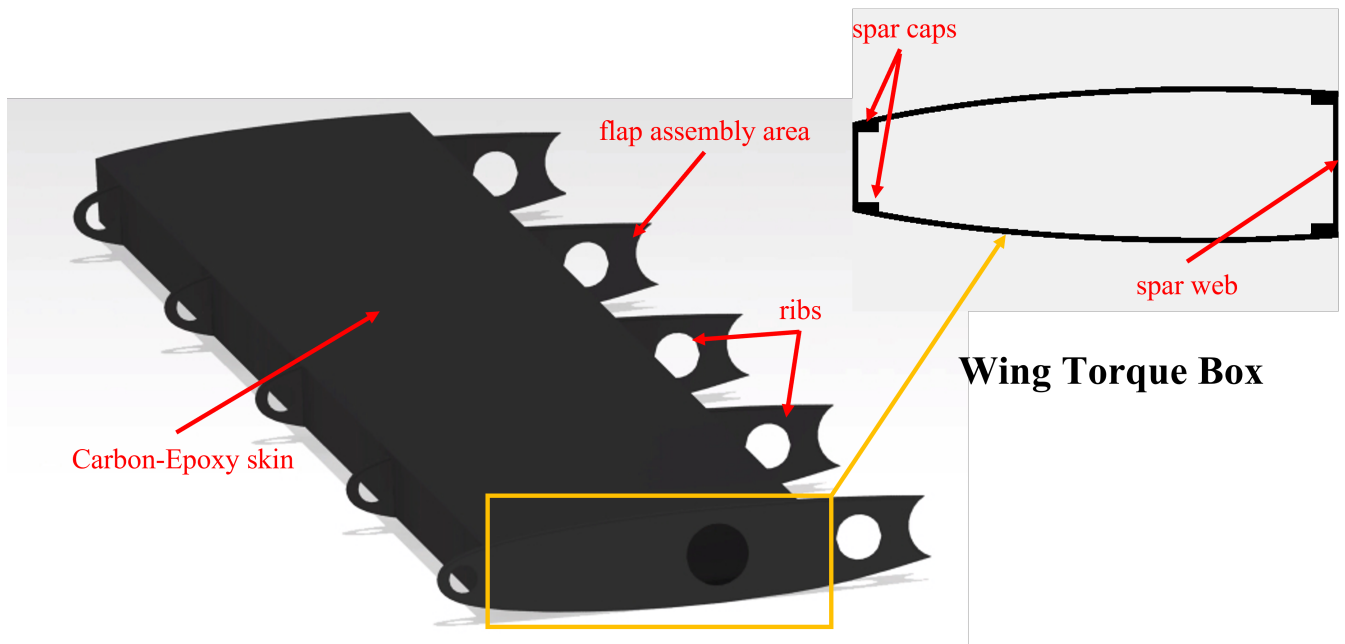


Figure 8.5: The primary load-bearing structure of the wing (shown without flaps / flaperons)

### 8.2.5 Wing Fuselage Connection

The front and rear spars of the wing are riveted and bonded to the fuselage bulkheads to support the wing torque box. Finite-element analysis using the Ansys solver was conducted to determine the stresses at the wing-fuselage connection.

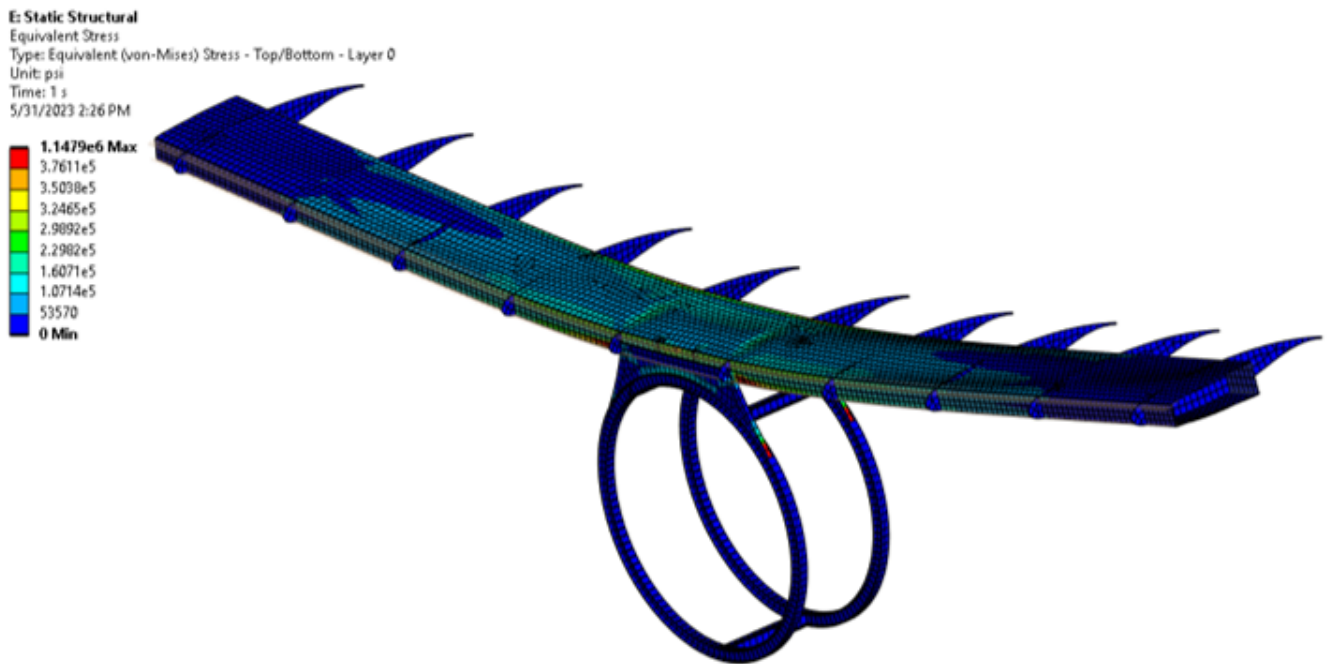


Figure 8.6: Finite element analysis of the wing-fuselage connection



The analysis was performed at 3.5g loading condition with MGTOW. Multiple configurations were analyzed with different materials, spar thicknesses, and wing-fuselage attachments. Figure 9.3 shows the final converged design with the structural stress distribution along the wing and bulkhead. The highest stresses occur near the wing-fuselage connection; hence more material was added to strengthen the connection. While the wing is less likely to experience such a loading condition, as per the FAR (CFR) Section 23.337 requirements the wing must be able to withstand a load factor of 3.5g and still maintain a safety factor that is more than 1.5 which is possible with our design.

### 8.3 Pylon Structure

The pylon houses a bevel gear, the Two-Speed Transmission, swashplate actuators, rotor hub system and a conversion actuator. The entire pylon tilts to minimize download, and the conversion actuator is sleekly stored within the pylon to minimize drag in cruise. The pylon was built such that the rotor blades have a 12 degree clearance from the leading edge of the wing in axial flight.

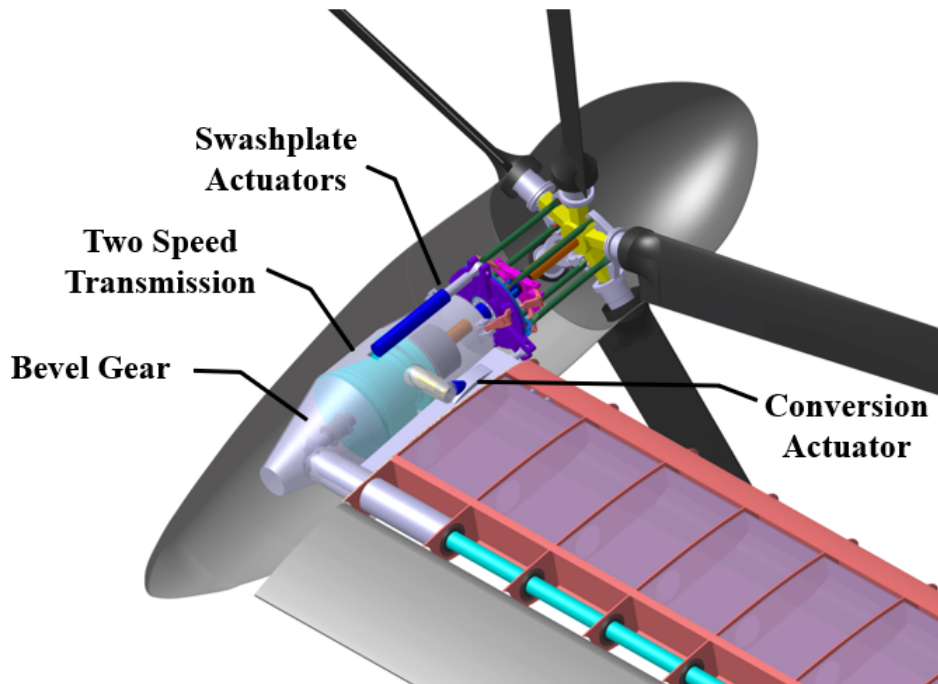


Figure 8.7: Pylon Interior shown in Axial Flight

Multiple configurations of pylon interiors, and methods of rotor rotations, were considered. First trade study conducted; placing the turboshaft in the pylon at the wing tip or inboard on the fuselage. Drag, weight, and complexity were considered. It was found that with proper burying of the turboshafts in the fuselage, the pylon could be tapered for optimal drag improving *Arion's* cruise efficiency. If the turboshaft was outboard in the pylon, both the main transmission and two-speed transmission would need to be stored in the pylon, increasing the weight needed on the wing structure and the complexity of the pylon/hub rotation system. Most importantly, the additional weight at the tip of the wing increased the risk of whirl flutter. Based on this study, it was determined that the pylon should only hold the two-speed transmission and the hub system, and the turboshaft must be placed inboard.

A sleek internal arrangement for the tilting mechanism was necessary. Hover download minimization was a priority as well. Because it was determined that the turboshaft would not be in the pylon, engine exhaust was no longer a concern with respect to pylon tilt angle. This meant that the full pylon must be tilted



to minimize download. Due to the weight of the two speed transmission, and the rotor system, a linear conversion actuator was needed. To minimize drag, the conversion actuator was stored inside the nacelle avoiding the bubble effect on the wing tip as seen on the V-22. The conversion actuator extends, the nacelle rotates along the drive shaft with a portion of the skin under the conversion actuator remaining ensuring proper clearance.

## 9 Airframe Design

### 9.1 Fuselage Design

The fuselage structure must not only support the weights of the internal components and the external loads but also accommodate the aerodynamic outer mold line. The dominant loads arise from the weight of the internal components, especially the engine, and payload, once the structure is restrained at the rotors. Three fuselage barrel designs were considered: the conventional aluminum (baseline), a conventional composite, and a composite geodesic (anisogrid lattice structures) fuselage barrel. The primary structure of the conventional fuselage (semi-monocoque fuselage) contains skin, bulkheads, and longerons as load-bearing elements. This is shown in Figure 9.1. Conventional fuselages require fasteners and joining elements, creating discontinuities in the load-bearing elements. Holes cause large concentrations of stress and, in composites, create fiber discontinuities, reducing their effective strength. Additionally, conventional fuselages may require keel beams to increase hull strength.

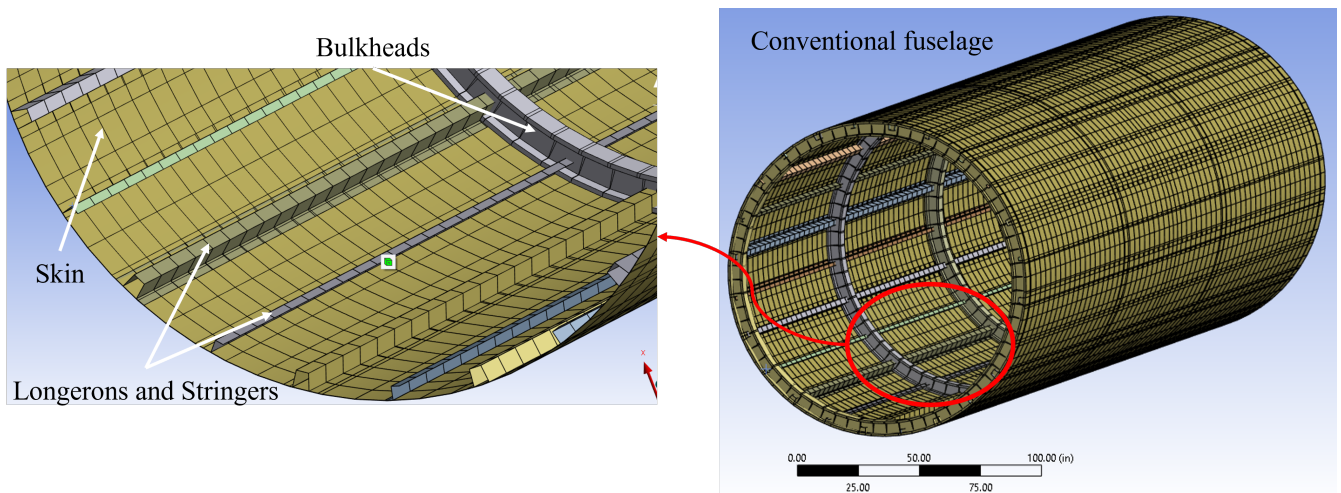


Figure 9.1: Semi-monocoque architecture for metal and composite primary airframe structure showing the basic load-bearing elements.

Geodesic composite lattice structures consist of helical and circumferential unidirectional carbon-epoxy composite ribs formed by continuous winding. The skin transfers only internal pressure and shear forces to the ribs. The lattice pattern of helical and hoop ribs has a constant cross-section (area =  $0.5 \text{ in}^2$ ), spacing, and angle of orientation, such that the unfolded pattern comprises a linear pattern of quadrilaterals and triangles, as shown in Figure 9.2. The ribs are the main load-carrying elements in contrast to the conventional longeron and bulkhead configurations. Skin damage does not cause the failure of the structure, whose strength is controlled by the ribs. Advanced anisogrid lattice structure formula, weight, bending stiffness, and suggested fabrication procedure was defined in a NASA technical memorandum in 1975 [29]. Unidirectional carbon tows impregnated with resin are wound into the groves of a mandrel, creating a web of helical and circumferential ribs. The 0.059 in (1.5 mm) thick skin is similarly wound around the

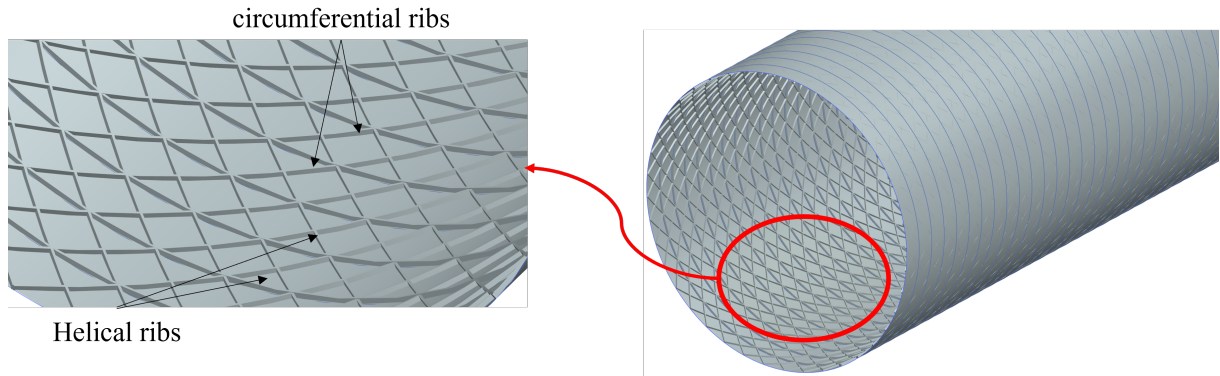


Figure 9.2: Geodesic fuselage geometry and design

mandrel or using the traditional wrapping and rolling around the mandrel. The composite skin is made of unidirectional and woven ( $\pm 45^\circ$ ) carbon epoxy plies to resist the hoop and longitudinal stress of the pressurized fuselage after completion of the winding process. After the winding process, the structure is placed in an autoclave for curing. The mandrel is then carefully removed, leaving the formed fuselage with ribs and skin.

The following features were considered to arrive at the final fuselage structure: Weight of the structure, Cost of the manufacturing process and materials, and ease of repair. Finite element models for each fuselage design were created and analyzed for critical loading conditions to meet a 3.5g load factor. Only the load-bearing elements were modeled: anisogrid structure, stringers, skin, and bulkheads. The total weight, including fasteners, circumferential and longitudinal interfaces, was then estimated using heuristics from known aircraft designs. All fuselages considered were designed for material strength, buckling, and bending strength.

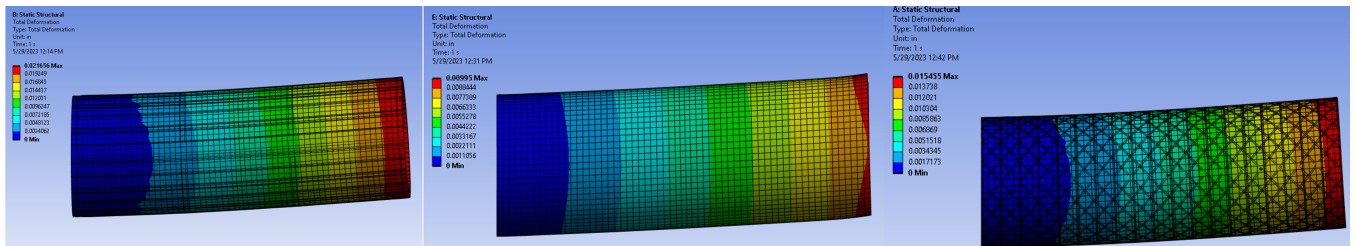


Figure 9.3: Finite element displacement for each of the fuselage designs. From left to right the conventional aluminum fuselage, conventional composite fuselage and geodesic fuselage

Fuselage Type	Weight (lb)	Max Displacement (in)
Conventional (Aluminum)	3134	0.021
Conventional (Composite)	2413	0.010
Geodesic (Composite)	2100	0.015

The geodesic fuselage was selected because of the higher strength-to-weight characteristics. It reduces the structure mass by 40% compared to the conventional fuselage. The construction of the geodesic fuselage can be streamlined to manufacture the fuselage structure since it consists of a uniform cross-section with no breaks in the lattice pattern. The ability to manufacture the entire fuselage barrel as a unit (integral construction) decreases the need for fasteners and bonding agents required for conventional fuselages. Fasteners and bonding agents in conventional fuselages further increase the total weight of the structure. The repetitive pattern is a significant factor in reducing the cost of construction caused by the efficient



use of capital equipment and rapid construction methods. Additionally, the smeared thickness of geodesic composites allows for interfacing with adjacent structures without a high weight penalty. The structure is more damage tolerant due to the redundant load paths formed by the rib lattice. A static load case that includes all the structural loads in the flight envelope over the aircraft's lifetime was applied to the chosen fuselage. The loads in the fuselage depend on the total mass, the mass distribution, the accelerations on the ground and in the air, and the aerodynamic forces of the aircraft. The structure is designed for a limit maneuvering load factor exceeding a positive limit of 3.5g to a negative limit of -1.0g.

## 9.2 Landing Gear

### 9.2.1 Configuration Trade Study

Five landing gear configurations were considered: skids, tricycle, quadricycle, and tandem with outriggers. The tricycle landing gear was the best compromise between weight, drag penalties, and stability during ground operations. Some configurations may also affect the wing frequencies and were discarded to avoid whirl flutter. Table 9.1 summarizes the configuration selection.

Table 9.1: Table summarizing the landing gear configuration study.

Configuration	Considerations	Decision
Skids	<ul style="list-style-type: none"> <li>· Cannot support a 50,000 lb vehicle.</li> <li>· Cannot be retracted for high-speed flight.</li> </ul>	Not chosen.
Quadricycle	<ul style="list-style-type: none"> <li>· Adds an extra gear to the tricycle with no additional benefits for the aircraft.</li> </ul>	Not chosen.
Tandem w/ Outriggers	<ul style="list-style-type: none"> <li>· Avoids the need for sponsons.</li> <li>· Outriggers add weight to the pylon which may induce whirl flutter.</li> <li>· The bending moment from the outriggers during landing will add weight to the wing.</li> </ul>	Not chosen.
Tricycle	<ul style="list-style-type: none"> <li>· May require sponson use which adds drag.</li> <li>· Stable for loading and unloading.</li> </ul>	Chosen.

### 9.2.2 Tire Selection

The tire selection was driven by the need to withstand the landing loads and foreign object debris with minimum size. A tire configuration with minimal internal pressure and maximal aspect ratio was also considered to expand landing capabilities on unprepared surfaces. Five tire types were considered: Type III, Type VII, Three Part Type, Radial, and Metric. Table 9.2 provides a summary of the best types of landing gears for each. The Type III 7-8 tire was chosen for the nose gear and a Type III 8.5-10 for the main gear because the Type III tires offer a lower tire pressure and higher aspect ratio which increase adaptability at the expense of a small increase in size. The nose gear tire is smaller than the main gear because there is a 20:80 load share between the front and rear landing gears.

### 9.2.3 Modeling Landing Gear Dynamics

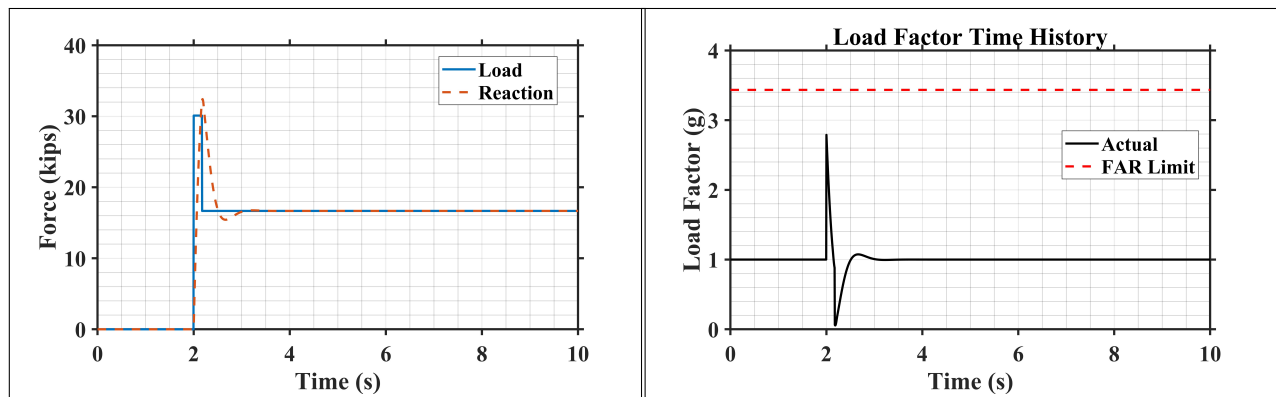
The RFP (Section 2.2, Requirement 5) states that the vehicle will land with two-thirds of the rotor lift at a sink rate of 10 ft/s. The RFP (Section 2.4.9, Requirement 3) also requires component design loads. To determine the loads, a dynamic model was created. The landing gear was treated as a one-degree-of-freedom system to simplify the analysis. Side and drag forces are accounted for. The force of the impact was assumed to be absorbed by just one landing gear to account for unfavorable conditions. The tires are assumed to be stiff as to not deflect and the wheels always stay in contact with the ground after touchdown. Then, the landing struts may be modeled as a simple spring-mass-damper system, where the natural frequency and damping ratio are tuned for the aircraft. The natural frequency was tuned to be



Table 9.2: Various tires considered for tire selection. \*Chosen tire.

Parameter	Tire Type	Size	Diameter (in)	Aspect Ratio	Tire Pressure (psi)
Front	Type III*	7-8	20.9	0.882	125
	Type VII	18×5.5	17.9	0.869	215
	Three Part	18×6.5-8	18.0	0.770	150
	Radial	20×4.4R12	19.8	0.843	265
	Metric	450×190-5	18.1	0.850	225
Rear	Type III*	8.5-10	25.7	0.898	125
	Type VII	26×6.6	24.2	0.887	355
	Three Part	21×7.25-10	21.3	0.779	325
	Radial	25.5×8.0R14	26.2	0.860	310
	Metric	670×210-12	26.8	0.874	205

much lower than the rotor frequencies to avoid ground resonance and to provide a displacement less than the estimated stroke length. The damping ratio was also tuned to meet the design goals. The damping ratio was set to 65% and the natural frequency was tuned to 7.43 rad/s (0.176/rev). Figure 9.4(a) shows the modeled impact load and the reaction load. Figure 9.4(b) shows the load factor acting on the aircraft during landing.



(a) Landing gear load and reaction time history.

(b) Landing gear load factor time history.

Figure 9.4: Landing Gear Analysis

### 9.2.4 Strut Sizing

As part of the RFP graduate requirement to provide stress analysis substantiation, the landing gear was sized with stress considerations. Specifically, the landing gear strut was sized using the peak reaction load shown in Figure 9.4(a). The landing gear structure is modeled as a hollow cylinder, cantilevered at the frame of the aircraft. The loads acting on the landing gear strut include the impact load, two transverse loads, and an internal pressure load. The impact load was determined using the model described in the previous section, and is applied axially to the strut. Two transverse loads are also applied based on FAR regulation. The two forces act at the free end of the landing gear strut, each with a magnitude equivalent to 80% of the impact load. In addition to the point loads, there is the consideration of internal pressures from the Oleo-pneumatic suspension. Oleo-suspensions are highly efficient at dissipating impact loads and are an industry standard in aviation. Using thick-walled pressure vessel equations, axial, hoop, and radial stresses were calculated for a typical internal pressure of 3600 psi. All stresses acting on the suspension



were summed to determine the net radial, axial, and hoop stresses. The internal diameter of the suspension was solved using the equation for Von Mises effective stress. The Von Mises stress was set to the yield stress of high-strength steel, with a safety factor of 1.5. The outer diameter of the strut was determined using Equation 3 along with a safety factor of 1.5 [30].

$$D_{oleo} = 1.3 \sqrt{\frac{4L_{oleo}}{R_{max}\pi}} \quad (3)$$

The length of the suspension,  $L_{oleo}$ , was calculated as 2.5 times the stroke length which is 2.15 ft [30]. The peak reaction load,  $R_{max}$ , is approximately 32 kips. As a final check, the strut is checked against the Euler-buckling criterion and was found to be well within the margin of safety. The final suspension properties were adjusted to also account for the longitudinal center of gravity since there is a 20:80 load share between the front and rear gears. The final landing gear properties are shown in Table 9.3.

Table 9.3: Summary of Landing Gear Sizing

Parameter	Strut Outer Diameter (in)	Strut Inner Diameter (in)	Strut Length (in)	Tire Type	Tire Size
Front Gear	1.97	1.64	25.8	Type III	7-8
Rear Gear	3.94	3.28			8.5-10

### 9.2.5 Gear Position and Packaging

The height of the aircraft center of gravity is used to determine the lateral placement of the landing gear. The gear is positioned laterally to provide the minimal allowable tip-over angle of 25°. The lateral placement also considers the tire displacement under static load and a fuselage clearance of 1.5 ft. The longitudinal placement of the landing gear is defined to provide a 20:80 load share between the front and main landing gear about the longitudinal center of gravity. The main landing gear and nose gear are placed at 55% and 13.75% of the fuselage length. The rear landing gear is packaged to fold laterally about the sponson tips and into the fuselage body. Other folding mechanisms were considered to avoid sponsons; however, the aircraft high center of gravity and heavy weight required the sponsons. The front gear retracts longitudinally into the fuselage toward the nose of the aircraft to aid in deployment should there be a hydraulic failure.

## 9.3 Cargo Bay and Ramp

The aircraft was designed with a large internal cargo bay with contiguous dimensions of 30 ft (9.14 m) long, 6.5 ft (1.98 m) high, and 8 ft (2.43 m) wide to hold a payload of 5,000 lb (2,268 kg), which may be cargo, 20 combat loaded troops, or some combination of the two. The primary access to the cargo bay is through the rear ramp as shown in Figure 9.5. The cargo door is composed of two doors that are actuated and held in place by hydraulic cylinders. The upper cargo door rotates upward to clear the horizontal area behind the cargo bay. The lower cargo door rotates downward and can be held level for unloading palletized cargo or rotated 15 degrees downward for personnel offload. Wheeled vehicles with proper clearance can also be driven directly onto the ramp using integrated ramp extensions.

The cargo bay floor is provisioned with reconfigurable, integrated wheels so that palletized cargo can easily roll in and out. Standard 463L master pallets are easily guided and locked into place by an integrated rail and lock system. Non-palletized cargo is also easily secured with chains, straps, or nets to a series of tie-down points built into the floor. The floor can also be reconfigured to be flush to load vehicles and minimize trip hazards for personnel. Non-powered vehicles and cargo are assisted in loading operations by an electrically-powered, self-contained hydraulic winch located at the front of the cabin underneath



the cockpit steps. Temporary pulleys installed to the tail allow the winch to assist with both onload and offload operations.

There is seating for 20 non-crew personnel in the cabin or up to 12 littered patients. With the spacious cabin, portable medical gear can be secured to the floor and powered by the aircraft's electrical system via outlets in the cabin.

Additional cabin loadouts may include internally carried auxiliary fuel tanks that will provide up to an additional 5,000 lb of fuel through the cabin's internal fuel transfer port. The 30% increase to the fuel on board will greatly extend the endurance and range. Command and control stations can also be loaded into the cargo bay that integrate into the aircraft's communication, navigation, and mission sensors, allowing mission commanders and highly trained sensor operators to embark on board *Ar-ion* to control the battlespace. Both the auxiliary fuel tanks and command and control stations are integrated into a 463L master pallet base for easy loading.

Personnel access to the aircraft can also be accomplished through the side door and ladder on the right side of the aircraft. Emergency egress from the cabin is provided through the main ramp if it is open, the side door, or 4 escape hatches in the fuselage bulkhead. The pilots may exit through the cabin or by activating the detonation cord in the windscreen. All emergency egress points can be opened or activated from outside the aircraft.



Figure 9.5: Rear cargo ramp open for loading cargo, vehicles, or personnel

## 10 Transmission Design

The requirement to cruise at 450 knots (232 m/s) imposes the challenge of avoiding tip Mach effects; however, designing the rotor blade for a low tip speed would incur penalties in hover performance. The solution is to vary the rotor blade tip speed as the vehicle transitions from hover to forward flight. Ideally, the rotor will operate at a nominal tip speed during hover and reduce the tip speed in forward flight. Results from blade element theory and sizing analyses corroborate the need for rotor speed reduction. A review by Amri et al., supports the requirement to reduce the rotor speed [31].

Three methods of decreasing rotor tip speed include: shortening the blade radius, introducing blade sweep, or reducing the rotational speed. At the target cruise velocity, blade sweep did not significantly lower the tip speed without suffering performance losses. Shortening the blade is difficult because of mechanical complexity and weight penalties. The most viable solution is to decrease the rotation rate of the blade. A two-speed transmission is needed to reduce rotor speed without ruining the engine-specific fuel consumption. The technology readiness level of two-speed transmissions may also be acceptable (TRL 4+).

### 10.1 Investigation of Two-Speed Transmissions

The first transmission studied was Moore's transmission [32]. Moore's gearbox has the advantage of a small and compact form factor because it modifies a typical helicopter transmission. The benefit of using a



familiar technology is that there is less of a technological gap. The disadvantages of Moore's invention stem from its lack of testing. There is no additional information on its design beyond the patent. Consequently, this transmission has a low technology readiness level (TRL 2).

Karem's transmission utilizes intermeshing gears to ensure a synchronous dog clutch match between both the slow and high-speed gears that extend from the main drive shaft [33]. The synchronous dog clutch allows for reliable clutching and declutching between desired rotor speeds. While the mechanical redundancy is thorough, the amount of gearing and shafts required lead to a heavy transmission weight.

The National Aeronautics and Space Administration (NASA) designed, tested, and identified two promising transmission configurations for its large civil tiltrotor (LCTR) project [14, 34]. These are the dual-star idler (DSI) and the offset compound gear transmissions (OCG). The offset compound gear operates in two different modes: hover mode and cruise mode. In hover mode, Figure 10.1, supplementary gearboxes reduce the engine rotational speed to the rotor angular speed required for hover. The offset compound gear input shaft then receives an input speed equivalent to the hover speed, labeled 1. The input shaft, labeled internal shaft, splits into two load paths: it simultaneously rotates an intersecting spur gear, and continues past the spur gear until it reaches a frictional clutch. Following the path of intersecting spur gear leads to the first gear reduction stage, labeled 2 and 3, where the spur gear meshes with an internal gear. The internal gear drives a hollow drum with a spur gear attached at the other end, labeled 4. The spur gear meshes with an internal gear, marked 5, and drives a low-speed drum that rotates at a 2:1 ratio compared to the input. The low-speed drum rotates at an angular rate equal to the angular speed required at cruise. The low-speed drum also accommodates a frictional clutch within its interior. The frictional clutch couples the internal input shaft to an output shaft when the clutch is engaged, shown with marking 6. A sprag clutch, labeled 7, connects the output shaft on an inner annulus and the low-speed drum on an outer annulus. The sprag clutch is overrunning, which means it does not interfere with the speed of the output shaft; therefore, the output shaft rotates at its nominal hover speed. With the sprag clutch overrunning, the rotor attached to the output shaft would revolve at the angular rate required for hover, as shown with label 8. In cruise mode, the transmission functions the same, except the frictional clutch disengages, marked 6 in Figure 10.2. When the frictional clutch disengages, the output shaft tends toward

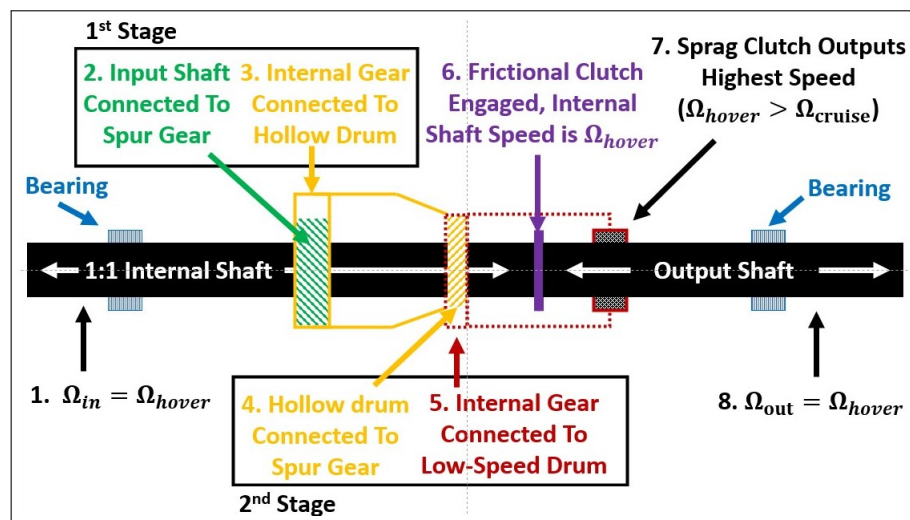


Figure 10.1: Simplified diagram of the NASA offset compound gear in hover mode.

a zero angular speed. Indeed, the output shaft would not revolve if it were not for the sprag clutch. As the output shaft slows down, it eventually approaches the angular speed of the low-speed drum. When the output shaft reaches the speed of the low-speed drum, the sprag clutch instantaneously drives the output shaft. The low-speed drum rotates the output shaft at the cruise speed; thus, the rotor operates at its



angular rate for cruise as shown by marking 8 in Figure 10.2.

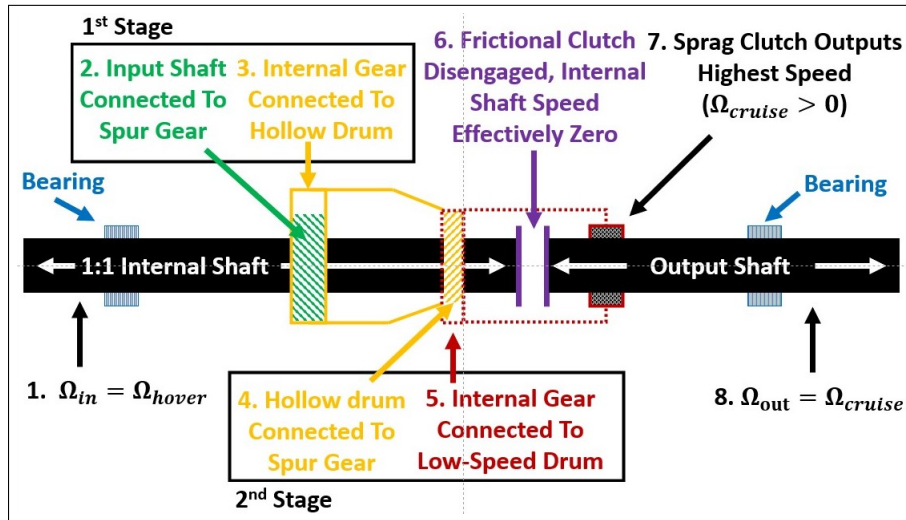


Figure 10.2: Simplified diagram of the NASA offset compound gear in cruise mode.

The NASA dual-star idler transmission works like the offset compound gear, except it uses a planetary gear to achieve the required speed reductions. The input shaft rotates at a reduced angular rate compared to the engine using supplementary gearboxes. The input shaft simultaneously rotates a planetary gear set and continues shaft rotation past the planetary. The planetary gear reduces the speed by a ratio of 2:1 and connects directly to a low-speed drum. The low-speed drum rotates at the same time as the internal shaft. If the clutch is engaged, hover mode activates, and a sprag clutch overruns to output the hover speed to the rotor. If the clutch disengages, cruise mode activates, and a sprag clutch drives to output the cruise speed to the rotor. The dual-star idler transmission was also considered for *Arion*.

## 10.2 Selection of a Two-Speed Transmission

The previous section briefly investigated the function of four two-speed transmissions. The advantages and disadvantages of each were deduced and led to the selection of one of the two-speed transmissions.

The NASA offset compound gear and dual-star idler transmissions have similar advantages, with a few differences and disadvantages. Both transmissions have the benefit inherent to their geometry: the low-speed drum required for both gearboxes improves the specific torsional stiffness of the structure. The offset compound gear further leverages the effect of geometry on stiffness because it uses its space efficiently: it maximizes the size of its gears within a compact volume. Both transmissions are less complex than the other transmissions, which reduces the weight and mechanical complexity. A key disadvantage to the dual-star idler is that it uses an idler gear with a 1:1 ratio, which is undesirable because it increases the wear and incurs penalties in maintenance and cost. The dual star-idler also has a higher part count than the offset compound gear. Both transmissions require supplementary gearboxes; however, the disadvantage is relatively slight when comparing all transmission designs.

Based on the advantages and disadvantages, the offset compound gear was selected. It has a lower part count and better structural performance. It minimizes mechanical complexity and weight. It uses a large hollow shaft as part of its gearing, which increases torsional stiffness without weight penalty. The increase in stiffness is advantageous in cruise when the torque is high. The disadvantage is that gearbox uses frictional clutches, which incur sizing, heating, and weight penalties. Using a dog clutch instead of a friction clutch may prove advantageous and this modification is recommended in our design. This



configuration is henceforth called the Terp Two-Speed Transmission (TTT).

### 10.3 Placement of Powertrain Components

Operating at a cruise speed of 450 knots (232 m/s) at cruising altitude requires a very high power installed. Typical tiltrotors maintain powertrain components within a wing pylon; however, increasing mass on the wing is undesirable for whirl flutter since it reduces the wing bending frequency, effectively reducing its stiffness from a dynamic perspective. The additional tip load also incurs a weight penalty because the wing structure requires reinforcement and the increased pylon size increases the vehicle's drag; therefore, placing most powertrain components within the fuselage becomes the desirable solution to mitigate weight and drag penalties. Inboard placement of heavy components also improves maneuverability during low-altitude operations like high-speed penetration, hovering, landing, and takeoff. However, moving the engine within the fuselage is not without its own set of issues. The mass of the primary driveshaft increases but by a relatively small amount because the driveshaft would replace the cross-shaft needed for a pylon-mounted engine. Engines within the fuselage increase the fuselage area and require a special air intake. With the engine placement defined, the layout of gearbox systems was determined.

The gear reduction required by the powertrain is found by comparing the defined engine and rotor speeds, which yields an overall transmission ratio of 49.5:1 for hover and 108:1 for cruise. The high transmission ratio indicates that multiple speed reduction phases are necessary. Four main subcomponents reduce the speed between the engine and the rotor: the main transmission, the two-speed transmission, and three intermediate gearboxes. As mentioned in Section 10.1, the placement of the two-speed gearbox must be after the main gearbox; therefore, the two-speed transmission is positioned within the nacelle and bears the final connection to the rotor. Placing the main gearbox by the engine then avoids weight on the pylon and mitigates the whirling of the drive shaft. Decreasing the rotational speed before the driveshaft leads to a reduction in critical shaft speed crossings. Additionally, placing the main transmission within the fuselage allows for shorter accessory drive lines for components like the auxiliary power unit (APU) and environmental control system (ECS), which further reduces weight. The power delivery from the engine in the fuselage to the rotor at the wing tip requires three 90-degree direction changes: two between the main transmission and the drive shaft, the other between the drive shaft and the two-speed transmission. A beveled gearbox is well-suited for the direction change, and three serve as intermediate gearboxes. All intermediate gearboxes are leveraged for additional gear reduction, reducing the complexity of the primary and two-speed transmissions. The final layout of the powertrain appears in Figure 10.3.

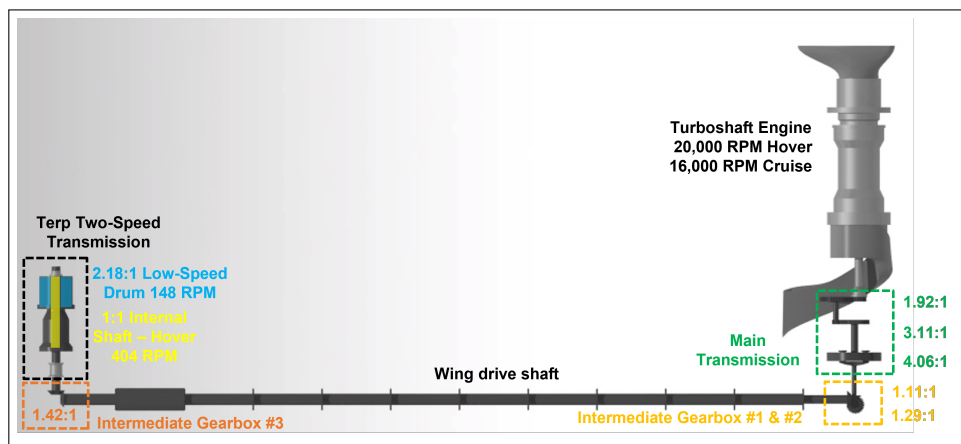


Figure 10.3: Final powertrain layout.

The layout begins with the engine rotating at its nominal speed of 20,000 rpm (2094 rad/s), or 80% nominal



speed (16,000 rpm, 1676 rad/s) for cruise. The engine transmits its power to the main transmission via its shaft. The shaft is attached to a spur gear that meshes with another spur gear to form the first stage of the main gearbox. An accessory drive runs off of the first stage as well. After the first stage reduces the speed by a ratio of 1.92:1, the power reaches the second stage, where two spur gears form the second stage with a gear reduction of 3.11:1. The power then arrives at a planetary gear set that reduces the speed by a gear ratio of 4.06:1. After the planetary gear set is the cross shaft and the first intermediate gearbox. The intermediate gearbox has a 1.11:1 gear ratio and uses beveled gears to change the direction of the load path by 90 degrees. There is a second intermediate gearbox that directly follows the first, reducing the speed by a 1.29:1 gear ratio. The second intermediate gearbox is connected to a cross-shafting member and to the main drive shaft. The load is transmitted across the wing drive shaft until it reaches another pair of beveled gears, which form the third intermediate gearbox. A two-speed transmission follows the second intermediate gearbox. The two-speed gearbox has an internal shaft that can directly transmit power with a 1:1 speed ratio if a dog clutch is engaged, resulting in a hover speed of 404 rpm (42 rad/s). For cruise, identical gear reductions occur, except the pilot lowers the engine to 80% nominal speed. The two-speed transmission's clutch is disengaged, and the load diverts to two gear stages with a 2.18:1 ratio. The resulting angular rate at the rotor is 148 rpm (16 rad/s).

## 10.4 Design of Transmission Components

The vehicle transmission system contains five main parts: the main gearbox, three intermediate gearboxes, and the Terp Two-speed Transmission (TTT). The main gearbox is primarily responsible for reducing the engine speed to the hover speed. The primary function of the two intermediate gearboxes is to change the load path direction; however, it is also possible to leverage slight gear reductions (around 1.25:1). The two-speed gearbox is solely responsible for reducing the hover speed to cruise speed. The defined functionality of each component assists with the design of the overarching system, specifically in finding the gear ratios required.

Finding the gear ratios is an iterative process. Gears have a natural number (positive integer) of teeth, which means gear ratios become fixed fractions that cannot match exact targets. The number of teeth is also limited because increasing the tooth size increases the gear size proportionally, and there is limited space. The natural numbers chosen for two gears meshing must also not be divisible by each other. If the number of teeth shares a common factor, the gear pattern will cause uneven wear. The divisibility principle explains why 1:1 gear ratios are highly undesirable. To find the gear parameters, a range of gear ratios and an array of (natural) number of teeth are set for the input shaft. Using the gear ratios and input teeth number, the number of teeth on the output gear is calculated and the number closest to a natural number is chosen. For example, if potential teeth numbers are 12.9, 14.3, or 15.4, then 12.9 is chosen and rounded to 13. Before iterating, the exact gear ratio is recalculated using the number of teeth on the input and output gears. The process is repeated for each stage, starting from the engine and moving down the powertrain toward the rotor.

The main transmission and intermediate gearboxes reduce the engine speed to the hover speed independently of the two-speed gearbox. Assuming the three intermediate gearboxes have a ratio of 1.25:1 each, the main gearbox must have a gear ratio of 25.34:1. The gear ratio is very high, so the speed reduction is assumed to occur over three stages. The three gear stages had the objective of progressively increasing the gear ratio. The goal allows the main transmission to ease the load transfer between gears. Converging the iterative design method yields gear ratios for the first, second, and third stages as 1.92:1, 3.11:1, and 4.06:1, respectively. Figure 10.4(a) provides an image of the main transmission design. The intermediate gearboxes were adjusted to have gear ratios of 1.11:1, 1:29:1, and 1.42 which are reasonable since the target was approximately 1.25. The design of the Terp Two-speed Transmission (TTT) is now possible, given that the primary and intermediate gearboxes were defined.



The TTT primarily serves the cruise condition because the gear reduction only occurs for cruise, and there is no gear reduction in hover. For the cruise condition, the engine reduces its speed to 80% to alleviate the burden on the two-speed gearing. The two-speed transmission has two gear stages. The input to the gearbox is 0.8 times the angular speed at hover, reduced by 20% via the engine, and the output is the angular speed required for cruise. The second stage gear ratio should be higher than the first to step up the torque change appropriately. After converging on the design, the gear ratios for the two-speed gearbox are 1.29 and 1.69 for the first and second stages, respectively. The overall transmission ratio of the two-speed gearbox is 2.18:1. During hover, the entire transmission system has a reduction ratio of 49.5, and during cruise the ratio is 108.

Table 10.1: Summary of key transmission characteristics in hover.

Transmission Step	Stage No.	Gear Interaction	Gear Type	No. of Gears	No. of Teeth	Gear Ratio	Output RPM	Output Torque (ft-lb)
Engine	N/A	N/A	N/A	N/A	N/A	1 (Shaft)	20,000	2,438
Main Transmission	1	Spur-Spur	Spur	1	25	1.92	10,417	4,681
			Spur	1	48			
	2	Spur-Spur	Spur	1	27	3.11	3,348	14,562
			Spur	1	84			
			Sun	1	32			
	3	Planetary	Planet	4	33	4.06	824	59,157
			Ring	1	98			
Bevel			1	27				
Intermediate Gearbox #1	1	Bevel-Bevel	Bevel	1	30	1.11	742	65,729
			Bevel	1	24			
Intermediate Gearbox #2	1	Bevel-Bevel	Bevel	1	31	1.29	574	84,901
			Bevel	1	26			
Intermediate Gearbox #3	1	Bevel-Bevel	Bevel	1	37	1.42	404	120,820
			Bevel	1	37			
TTT (Hover Mode)	N/A	N/A	N/A	N/A	N/A	1 (Shaft)	404	120,820

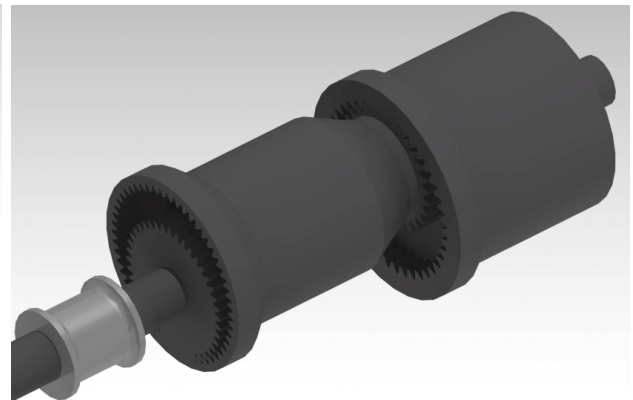
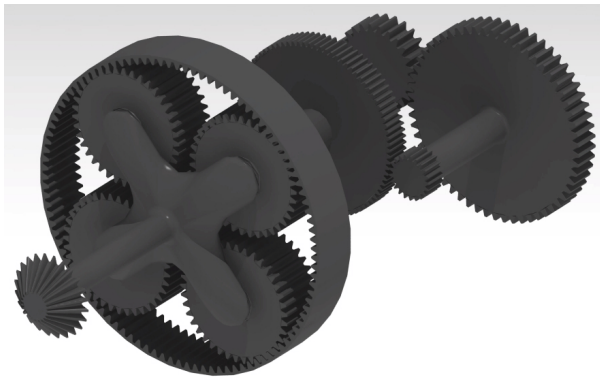
## 10.5 Novel Terp Two-Speed Transmission Clutch System

The Terp Two-Speed Transmission (TTT) features a novel clutch mechanism. The clutch found on the NASA offset compound gearbox is a frictional clutch which is highly prone to wear, especially with the amount of torque at the rotor. To combat the immense torque, multiple clutch plates would be needed which would increase weight, parts, and volume. The clutch plates may be unreliable because heating would reduce the effectiveness of friction. The extreme torque also suggests frequent replacements may be necessary, inflating maintenance costs. An alternative solution is a dog clutch, which is less prone to wear. The dog clutch uses large teeth to form a physical connection rather than a frictional one. Though the dog clutch may be better when the clutch is engaged, it may be problematic during shift changes. The clutch teeth do not allow for relatively smooth gear changes. Typically a synchromesh would assist with the shifting of a dog clutch because it helps synchronize the teeth; however, a synchromesh cannot be installed because of the two speed. A synchromesh is installed between two adjacent gears: a configuration not found on the two-speed transmission. Instead, a unique control system may be designed to synchronize the clutch to significantly reduce transient loads and wear. The control system proposed is a collective-induced rotor speed controller (CRSC).



Table 10.2: Summary of key transmission characteristics in cruise.

Transmission Step	Stage No.	Gear Interaction	Gear Type	No. of Gears	No. of Teeth	Gear Ratio	Output RPM	Output Torque (ft-lb)
Engine	N/A	N/A	N/A	N/A	N/A	1 (Shaft)	16,000	3,047
Main Transmission	1	Spur-Spur	Spur	1	25	1.92	8,333	5,851
			Spur	1	48			
	2	Spur-Spur	Spur	1	27	3.11	2,679	18,202
			Spur	1	84			
	3	Planetary	Sun	1	32	4.06	659	73,946
			Planet	4	33			
Ring			1	98				
Intermediate Gearbox #1	1	Bevel-Bevel	Bevel	1	27	1.11	593	82,162
			Bevel	1	30			
Intermediate Gearbox #2	1	Bevel-Bevel	Bevel	1	24	1.29	459	106,126
			Bevel	1	31			
Intermediate Gearbox #3	1	Bevel-Bevel	Bevel	1	26	1.42	323	151,025
			Bevel	1	37			
TTT (Cruise Mode)	1	Spur-Internal	Spur	1	41	1.29	250	195,227
			Internal	1	53			
	2	Spur-Internal	Spur	1	35	1.69	148	329,098
			Internal	1	59			



(a) Internal view of main transmission consisting of a 2-stage gear set and a planetary gear.

(b) Terp Two-Speed Transmission inspired by the NASA offset compound gear transmission.

Figure 10.4: Transmission Drawings

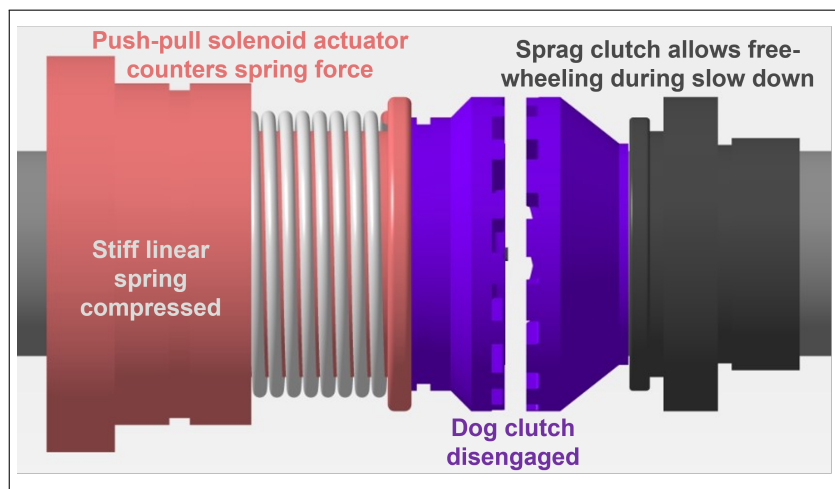


Figure 10.5: Internal view of the Terp Two-Speed Transmission clutch system when *Arion* is in hover mode.

The principle behind CRSC is to leverage the collective in controlling the rotor speed during a free-wheeling state. Recall from Section 11.2, when the two-speed transmission clutch is engaged, the rotor is in hover



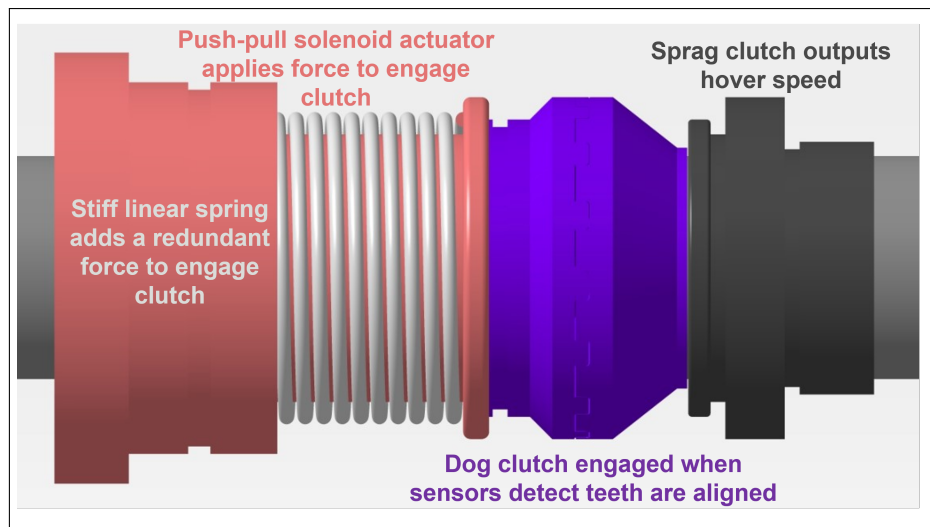


Figure 10.6: Internal view of the Terp Two-speed Transmission clutch system when *Arion* is in cruise mode.

mode and spins at its fastest angular rate. When the aircraft is in airplane mode, the clutch is disengaged and the rotor temporarily enters a free-wheeling state. During the free-wheeling state the rotor must be slowed in a quick and controlled manner to avoid overspeeding and blade resonance frequencies. When the rotor slows down to the cruise speed setting, the low-speed drum on the two-speed transmission drives the rotor. In the case that the aircraft is in cruise mode, and the hover speed is required (i.e., low to high speed) the collective setting may be changed to increase the rotor speed. Increasing the rotor speed is possible because when the clutch is disengaged, the sprag clutch allows the rotor to rotate at the cruise speed, or enter a freewheeling state if the rotor spins faster than the cruise speed. *Arion* can leverage its turbofan to increase thrust, allowing for angular acceleration of the rotor if collective control is not effective alone. As the rotor approaches the hover speed, the dog clutch is synchronized with the high-speed shaft and the clutch may be engaged. Speed-matching allows the dog clutch to engage with minimal wear and reduces the transitional torque load.

The collective-induced rotor speed controller (CRSC) is implemented with an onboard suite of sensors and actuators. Hall effect sensors and encoders for tracking the synchronization of the dog clutch teeth. Tachometers and Hall effect sensors are used to determine the rotor speed. A stiff spring around the internal shaft is placed to maintain a constant force on the clutch, thus maintaining its engagement. A linear push-pull solenoid is mounted on the shaft and actuates to compress the spring and disengages the dog clutch. When the clutch is re-engaged, both the spring and the solenoid apply a force to quickly mesh the dog clutch. If the solenoid fails, the spring alone maintains enough pressure to keep the clutch engaged. During a solenoid failure, the aircraft speed is limited but the spring-engage clutch allows the pilot to land safely because the hover rotor speed is maintained. If the CRSC system fails, the high-strength steel dog clutches may be rated for at least three forced impacts before maintenance is required: allowing the aircraft to complete an entire mission as defined by the RFP. If the dog clutch fails entirely and the vehicle needs to land, the aircraft may still freewheel at the cruise-speed or higher, via collective control while the airplane design glides down to safety. Figure 10.5 shows the dog clutch engaged and Figure 10.6 shows the dog clutch disengaged.



## 11 Propulsion System

### 11.1 Propulsion Selection Overview

The selection of propulsion systems to satisfy the RFP was heavily driven by the high power requirements for both hover and high-speed forward flight at 450 kts. Following the aircraft general configuration selection described in Section 3, only conventional combustion engines were determined to have a high enough specific energy to realistically power the rotor. Despite increases in battery and electric motor technology, the specific energy of a fully electric or hybrid electric system would add significant weight to the vehicle, despite some savings on drivetrains and total engine weight.

Similarly, the high-speed thrust required for the augmented thrust portion of the aircraft was limited to turbofan or turbojet engines. If thrust was augmented with a propeller, the rapidly decreasing propulsive efficiency required larger engines despite some fuel savings. The placement of a propeller in the current configuration was difficult without disrupting the high-speed aerodynamics with a tractor-type propeller or adding significant safety risk to cargo loading operations with a pusher-type propeller.

The choice between turbofan and turbojet engines came down to an analysis with the sizing code that found the decreased thrust specific fuel consumption (TSFC) of the turbofan engines at 450 kt resulted in a lower gross takeoff weight at the start of the RFP mission.

Initially, a single turbofan engine was considered with a V-Tail configuration, but stability concerns dictated a transition to a T-Tail configuration (see Section 15). The centrally placed vertical stabilizer forced an analysis of whether a one or two-engine configuration would be preferred. Ultimately, the analysis found that the difference between one or two turbofan engines would have negligible effect on weight, engine frontal area, or total TSFC. The addition of the second engine adds redundancy satisfying several RFP requirements including resilience to FOD and the highly contested environment. If a single turbofan engine was lost for any reason including FOD (Foreign Object Damage) or hostile fire, the remaining engine along with the rotors would still be able to provide thrust for a high-performance conversion, climb-out, and a cruise speed in excess of 400 kts.

### 11.2 Turbofan & Turboshaft Sizing

To determine the turbofan size, geometric data on military and civil turbofans was analyzed [12]. Both military and civil data were considered to determine current capabilities and to better predict future engine capabilities. The data reviewed relates thrust to diameter and dry weight. A linear fit was applied and a best-fit equation was determined. Figure 11.1(a) shows the relationship between thrust and diameter for turbofan engines. Figure 11.1(b) shows the relationship between thrust and dry weight for a turbofan. Using the thrust requirement of the aircraft and the best-fit equations, the diameter and weight were calculated. The diameter of each engine was found to be 39.3 in (99.8 cm) and the weight of each engine is 2119 lb (963 kg).

To determine the size of the turboshaft, a similar process of analyzing data was used except diameter and weight is correlated with power. Figure 11.2(a) depicts the relationship between diameter and power and Figure 11.2(b) shows the relationship between weight and power. The weak relationship between thrust, weight, and diameter meant that the engine parameters must be discretely selected rather than estimated using a best-fit equation. Given the power required by the aircraft, the diameter of each turboshaft is 27 in (69 cm) and the weight is 1,100 lb (501 kg) each.



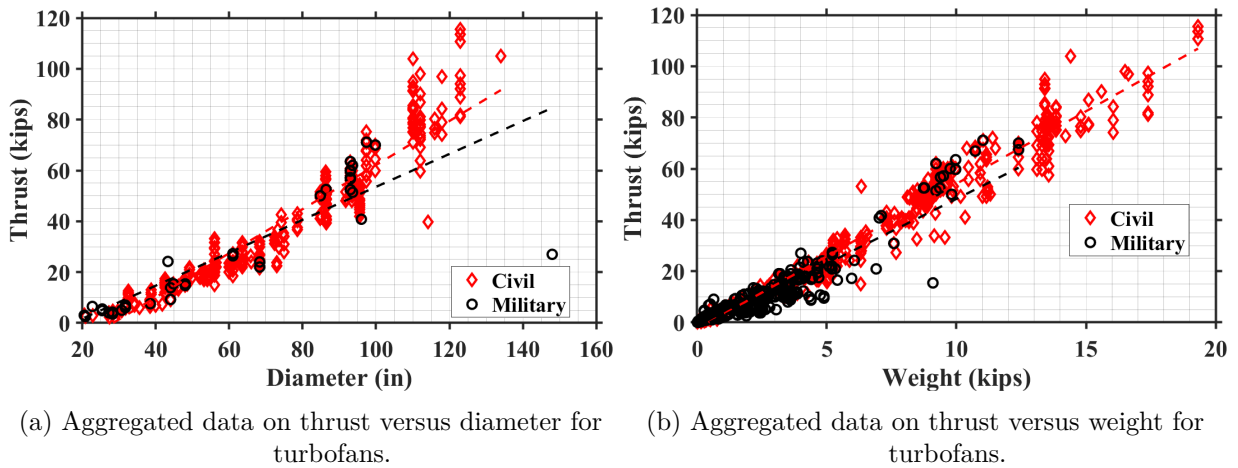


Figure 11.1: Turbofan engine sizing

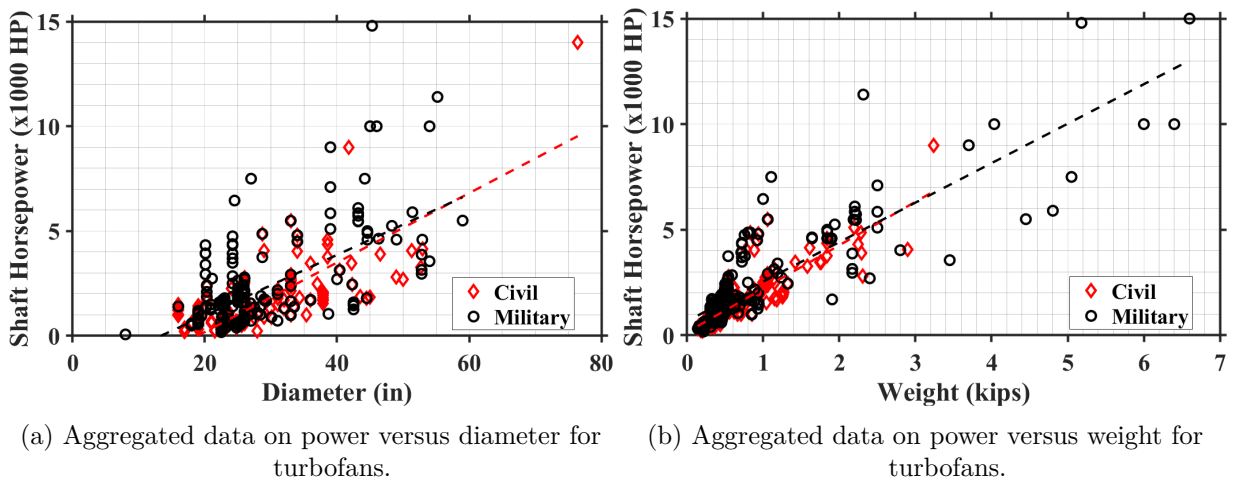


Figure 11.2: Turboshift engine sizing

### 11.3 Engine Material Selection

While the high bypass turbofan engine configuration has conceptually remained the same since its inception, significant improvements have been made in the material properties and spool configuration that have enabled continued marginal improvements in the TSFC. Specifically, material properties such as low density, high strength, and heat resistance have allowed larger fan blades to withstand stronger centrifugal forces, higher compressor ratios to withstand increased temperatures, and superalloy turbine blades to withstand higher combustion exit temperatures [35]. These improvements are considered in the aircraft sizing code as a technology factor that accounts for the reduction in engine and fuel weight required to produce the same thrust.

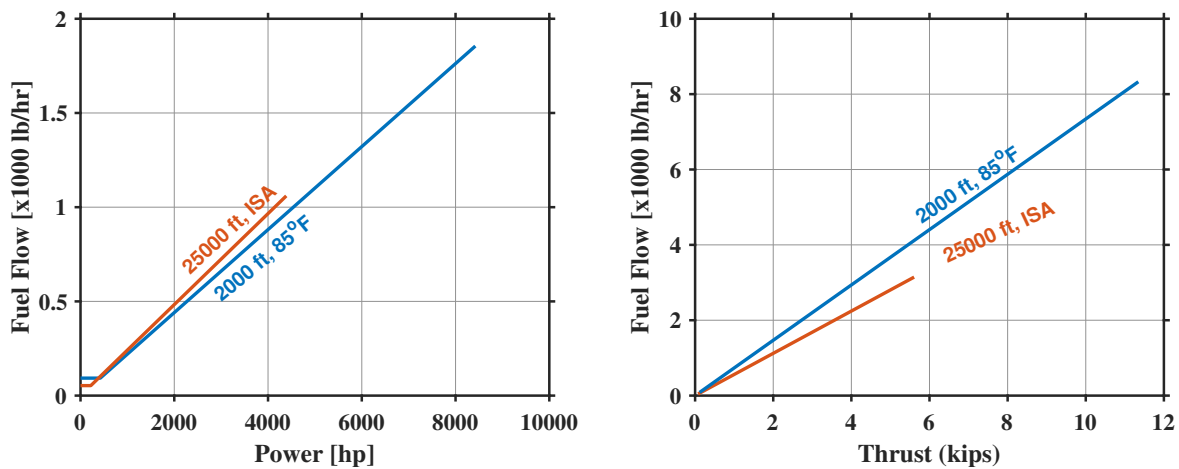
While state-of-the-art turbofan blades transition to carbon fiber composite materials for their favorable strength, corrosion, and creep properties, it is important for fan blades of *Arion* to have a reinforced leading edge that will increase resistance to damage from FOD ingestion. The composite fan blade with titanium leading edge has also demonstrated favorable impact damage resistance, reducing the risk of collateral damage to the tail, fuselage, or the other engine in the event of a bird strike or other catastrophic single engine failure [35].



## 11.4 Engine Performance Data

The turboshaft model was derived from the engine model given in the 2007 AHS RFP [36]. The turbofan model is based on a gas dynamics equation-based methodology (Ref. [37], Ch. 6).

Engine performance data is shown in Figure 11.3. The turboshaft fuel flow is shown in Figure 11.3(a) and the turbofan fuel flow is shown in Figure 11.3(b). Turboshafts are rated for power available while turbofans are rated for thrust available so the x-axis in each figure corresponds to the throttle setting. Note that the maximum throttle setting is reduced at higher altitude due to lower-density air. The turboshaft is slightly more fuel efficient at the lower altitude while the turbofan is more fuel efficient at cruise altitude.



(a) Fuel flow rate vs. power setting for turboshaft (b) Fuel flow rate vs. thrust setting for turbofan

Figure 11.3: Fuel flow rate for turbofan and turboshaft engine vs. throttle setting

## 12 Vehicle Aerodynamic Design

The airframe shape was selected based on the cruise flight conditions and cargo dimensions specified in the RFP. An optimization study was conducted to determine a cross-sectional area that would minimize fuselage profile drag. At a cruise altitude of 20,000 ft, cabin pressurization is required. With a cruise speed of 450 knots, *Arion* is operating near Mach-drag divergence for the majority of its mission. Preliminary iterations of the airframe were designed with the intention of minimizing drag based on current aircraft operating at transonic speeds. In-house 3D RANS CFD simulations were performed to optimize the airframe geometry while accounting for structural and mission limitations. Additional design considerations included preparedness for hostile environments and ease of loading/unloading cargo.

### 12.1 Fuselage

The baseline fuselage shape was designed based on existing tiltrotor configurations, NASA XV-15, and Bell V280 Valor. Modifications were made to this design, catering to mission requirements and minimizing drag. An in-house CFD solver, HAMSTR [38], was used for the CFD-based drag estimations and ANSYS Fluent solver was also used for certain cases.

A steady simulation was conducted at a cruise speed of 450 knots at 25,000 ft and standard ISA conditions. A body pitch angle of 0° was used. Figure 12.1 illustrates the flow-field of the initial fuselage geometry,



highlighting vortices formed and the pressure distribution along the fuselage. Past the nose of the vehicle, the flow travels along the surface of the vehicle, until the ramp region, where there is a tendency for flow to separate, leading to high-pressure drag. A ramp was deemed necessary for this mission based on the payload requirement. Due to the potential of a hostile environment during the mid-mission landing segment, it was assumed ground crew assistance would be minimal. Thus, a cargo bay door that could be opened remotely was desired.

A ramp's robustness allows *Arion* to carry a diverse range of cargo, from personnel to vehicles, and unload in less than 2 minutes without affecting the pilot workload. Careful consideration was given to the ramp design, recognizing the twin engines and empennage would still need to be structurally supported. Additional modifications were made to follow a similar ramp design to the C-130 Hercules. As observed in Figure 12.2(a), the flow from the bottom of the fuselage has two small regions of separation, highlighted by the low-pressure contour at the bottom corners of the fuselage. The sudden change in area provokes flow separation in this region, increasing pressure drag. However, for the majority of the ramp region, flow remains attached to the rear end and stays attached up until the upper end of the rear ramp, thus drag due to small regions of flow separation does not dominate pressure drag in this scenario. In the ramp region, Figure 12.2(b) shows two large vortices leaving the fuselage due to the pressure difference between flows coming from the different surfaces of the fuselage. These vortices create suction at the ramp surface, further increasing the pressure difference between the front and rear surfaces of the fuselage, leading to an increase in pressure drag. In addition to increasing drag, the circulation due to the vortices contribute to down force on the upper surface in the ramp region as can be seen in Figure 12.2(a). Large portions of upwash can be seen in Figure 12.2(b), further contributing to the strength of the vortices. With plenty of room for improvement, the initial flat plate drag area and download area are  $13.2 \text{ ft}^2$  ( $1.23 \text{ m}^2$ ) and  $33.5 \text{ ft}^2$  ( $3.11 \text{ m}^2$ ), respectively.

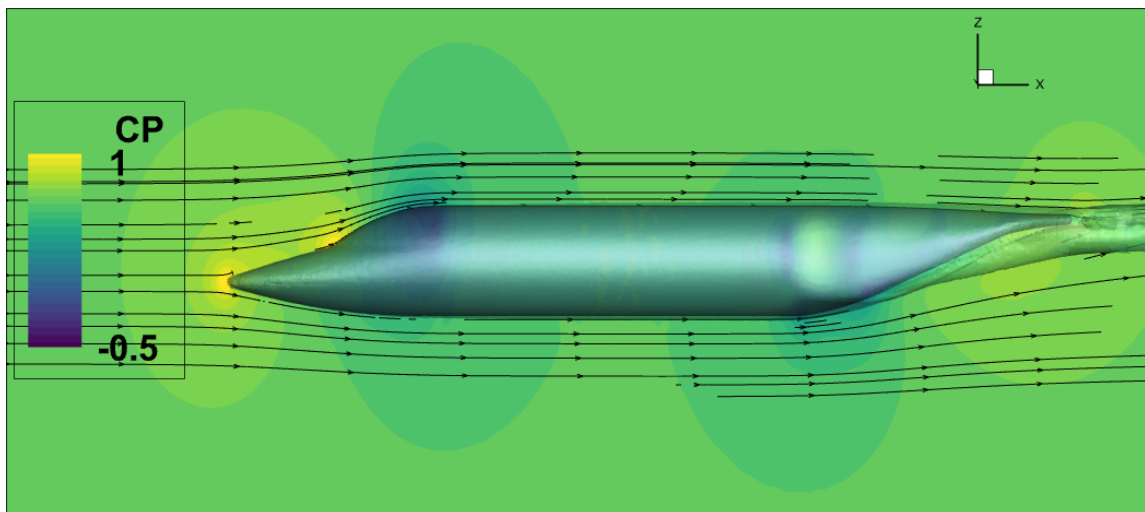
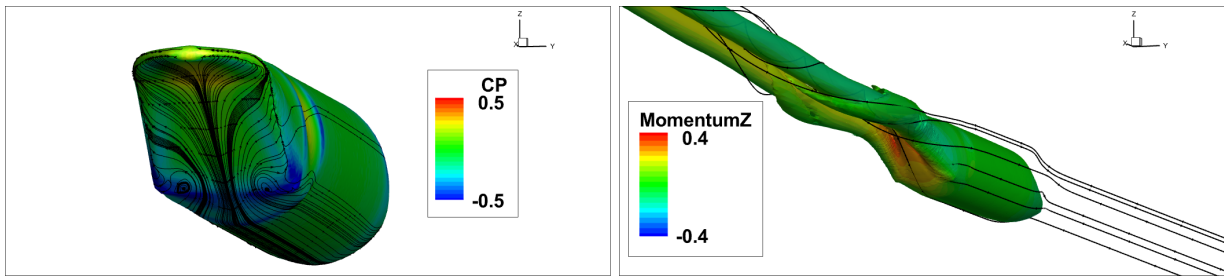


Figure 12.1: Fuselage Version 1.0 Pressure Distribution

For further improvement, the strength of the vortices arising at the trailing edge was reduced. Using Ansys Fluent, multiple fuselage configurations were evaluated. Decreasing the slope of the ramp was one method of reducing the strength of the trailing vortices. This helps to remove sudden changes in area and support flow attachment far upwards along the ramp as it leaves the bottom surface of the fuselage, as shown in Figure 12.3(a), thereby maintaining low-pressure drag. While decreasing the slope of the ramp warrants a longer ramp, the mitigation of the vortices strength outweighs the increase in skin friction drag. In addition, a longer ramp increases the structural integrity in the region of the twin engines and empennage. The reduction in the strength of trailing vortices can be seen in Figure 12.3(b) compared to previously shown in



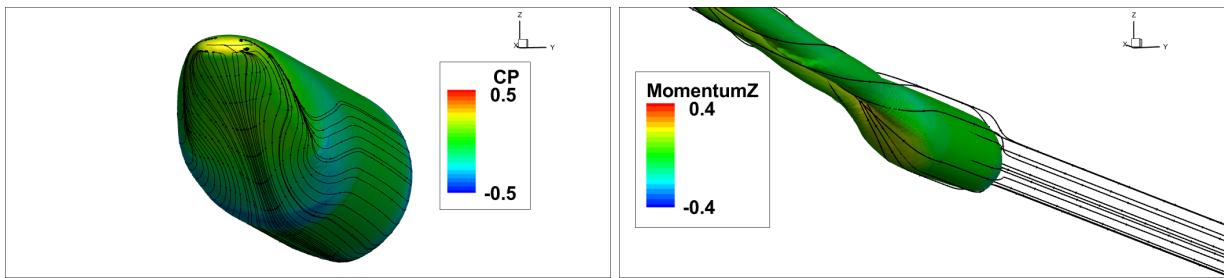


(a) Fuselage Version 1.0 Pressure Distribution

(b) Fuselage Version 1.0 Upwash

Figure 12.2: Initial Ramp Design

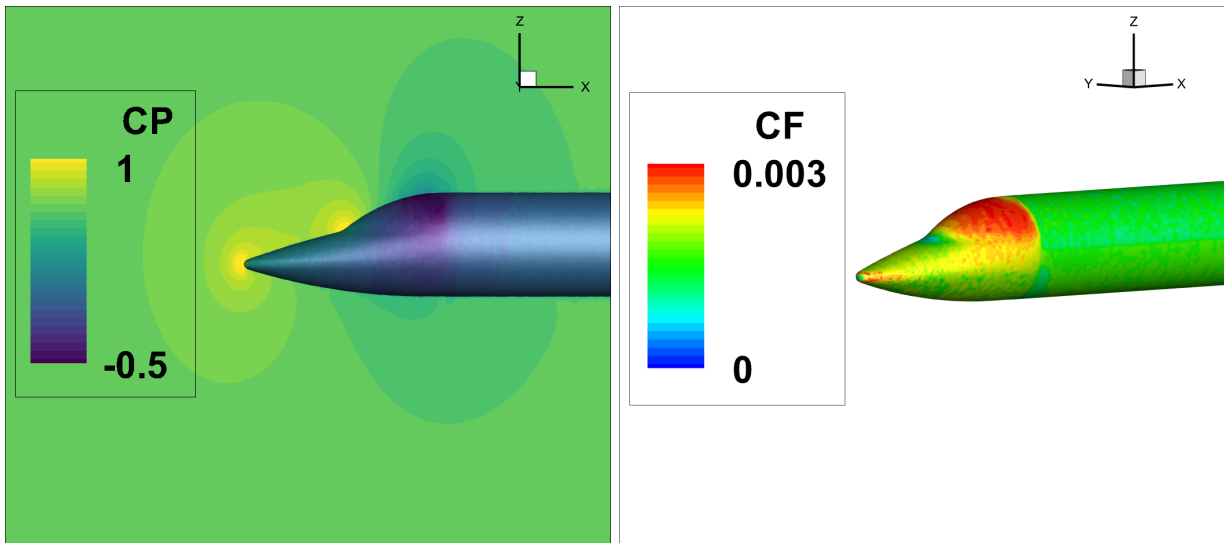
Figure 12.2(b). The use of vortex generators was investigated to produce counter-rotating vortices to offset the vortices leaving the trailing edge. However, based on sizing studies of vortex generators [39] and given the large generators that would be needed to counter turbulent flow, the weight and skin friction increase could not be justified. The turbofan exhaust was expected to only enhance the shedding of vortices and aid drag reduction further.



(a) Fuselage Version 2.0 Pressure Distribution

(b) Fuselage Version 2.0 Upwash

Figure 12.3: Improved Ramp Design



(a) Pressure Distribution

(b) Skin Friction Drag Distribution

Figure 12.4: Pressure and Skin Friction Contour of Fuselage Version 1.0



Along with the ramp, a study was conducted on minimizing the drag and download accumulated at the nose. Initially, a change in slope near the windshield was preferred for improved visibility. But as seen in Figure 12.4(a), the pressure on the nose acts both in the negative lift direction as well as the drag direction. The sudden change in slope results in a second stagnation region at the vertex of this curvature change. To minimize download, two configurations were analyzed. Figures 12.5 show the pressure distribution of these two fuselage noses, each showing a significant improvement over the baseline. The nose geometry in Figure 12.5(a) offers a solution to the high-pressure drag by utilizing a steeply raked windshield. By maintaining a favorable pressure gradient on the nose, the pressure drag decreases in magnitude significantly, however, it extends farther along the nose than desired. Due to the extended favorable pressure gradient region, the velocity accelerates significantly, specifically in the nose-cargo bay blend region resulting in an increase in skin friction. In addition, the low position of the nose relative to the center of the body results in a higher download on the fuselage. As an alternative, a slightly blunter nose raised towards the mid-body, with a sleek aerodynamic after-body was used as can be seen in Figure 12.5(c). The blunt nose corresponds to large pressure at the stagnation point but quickly decreases thereafter due to the favorable pressure gradient offered by the curvature of the geometry. Therefore, the dynamic pressure does not increase to the same degree as for that of the steeply raked nose; thus skin friction drag is lessened as shown in Figure 12.5(d). The raised nose location reduces download on the fuselage further. Overall, the reduction of skin friction drag offered by the rounded nose outweighs any pressure drag increase.

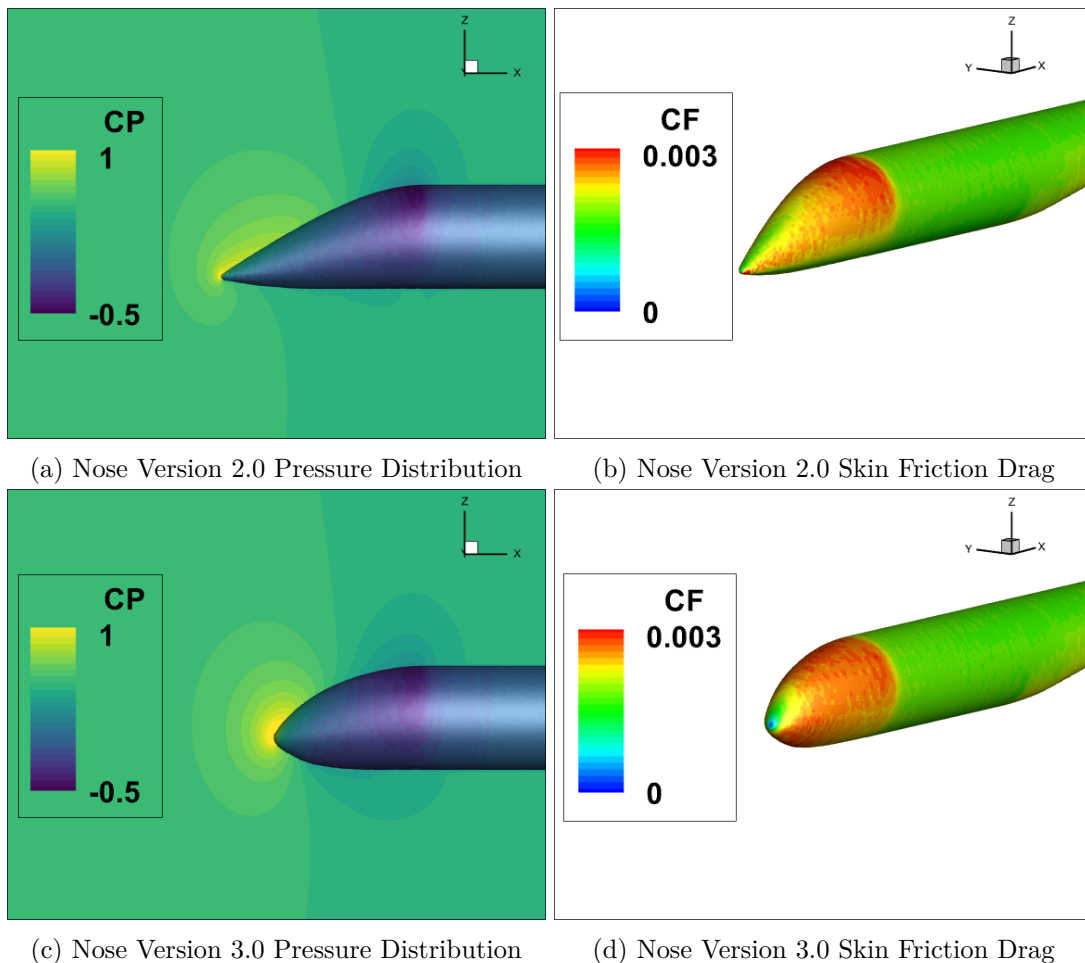


Figure 12.5: Comparing Pressure and Skin Friction Drag for Different Nose Geometries

Drag breakdowns of the baseline fuselage version compared to the final two versions are reported in Table



12.1. Improvements in the nose and ramp region resulted in a 54% reduction in download and 45% reduction in drag.

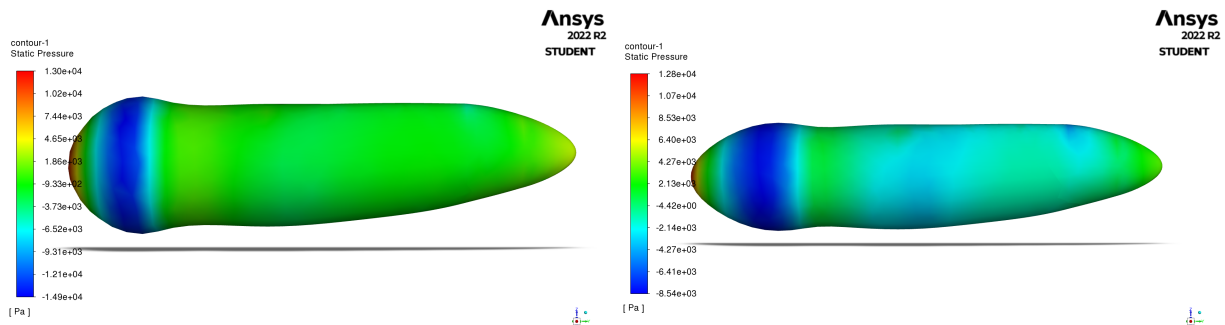
Table 12.1: Fuselage Drag

Iteration No.	Download - lb (N)	Drag - lb (N)
Fuselage Version 1.0	10,289 (45,769)	4,062 (18,069)
Fuselage Version 2.0	4,941 (21,981) <b>-51.98%</b>	2,318 (10,309) <b>-42.93%</b>
Fuselage Version 3.0	4,716 (20,980) <b>-54.16%</b>	2,227 (9,905) <b>-45.17%</b>

### 12.2 Rotor Pylon

In addition to the fuselage, the rotor pylon was also optimized for minimizing drag. The turboshaft engines are installed in the fuselage body which allows for smaller pylons at the wing tip. The rotor pylon incorporates a large spinner to hide the cylindrical blade root. The spinner is designed to cover the root cut-out (0.12 R). The pylon was designed to follow area rules with an indentation or dip in the region of the blade root. This would slow the flow, reducing the dynamic pressure experienced by the exposed root airfoils. The after-body was designed to eliminate flow separation while maintaining a low-pressure drag. Drag estimates were conducted using Ansys Fluent and the results are shown in Figure 12.6.

To reduce the high pressure experienced due to the bluntness of the pylon, a shallower gradient near the leading edge was used. While there still is a stagnation point, the pressure drag in this region decreases significantly for the second pylon iteration. There is a small increase in skin friction drag in the second iteration, however, the reduction in pressure drag makes this configuration more favorable as shown in Table 12.2.



(a) Rotor Pylon Version 1.0 - Blunt Nose

(b) Rotor Pylon Version 2.0 - Slender Nose

Figure 12.6: Comparing Pressure Distribution for Different Rotor Pylon Configurations

Table 12.2: Rotor Pylon Drag

Iteration No.	Skin Friction Drag - lb (N)	Pressure Drag - lb (N)	Total Drag - lb (N)
Rotor Pylon Version 1.0	144.3 (642.0)	264.8 (1,178)	409.2 (1,820.0)
Rotor Pylon Version 2.0	156.5 (696.0)	163.8 (728.6)	320.3(1424.6)



### 12.3 Cruise Operating Conditions

Using the final fuselage (version 3.0), further analysis was conducted to obtain the best body pitch that can provide minimum drag.

At zero-degree body pitch, the two vortices along the ramp area dominate the total drag. The pressure difference between the front and rear of the fuselage promotes flow to move towards the rear of the fuselage, thus contributing to the strength of the vortices. This phenomenon is highlighted in Figure 12.7(a). Off-design body pitch angles were investigated to determine if the drag and download could be mitigated at different conditions. At near-zero angles of attack, the flow has a tendency to curl around the fuselage due to the suction peak in the rear. This swirling motion near the tail is significantly lessened at  $2.5^\circ$  and  $5^\circ$  fuselage pitch angles as can be seen in Figures 12.8(b) and 12.8(c). Additionally, flow along the ramp is more inclined to stay attached at a body pitch angle of  $5^\circ$  compared to  $0^\circ$ . These results are highlighted in Figure 12.8 as low skin friction drag near the edges of the ramp is an indication of flow separation.

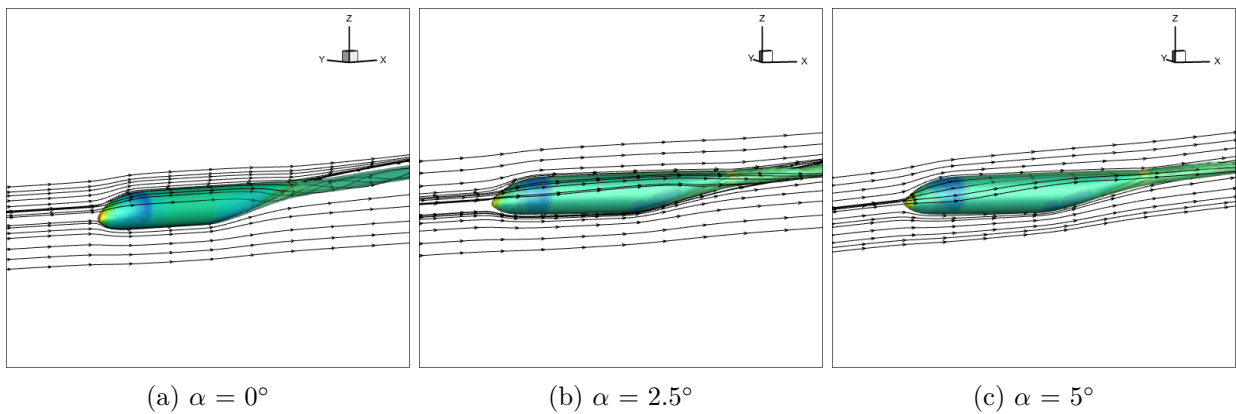


Figure 12.7: Fuselage pressure distribution and flowlines for different body pitch angles

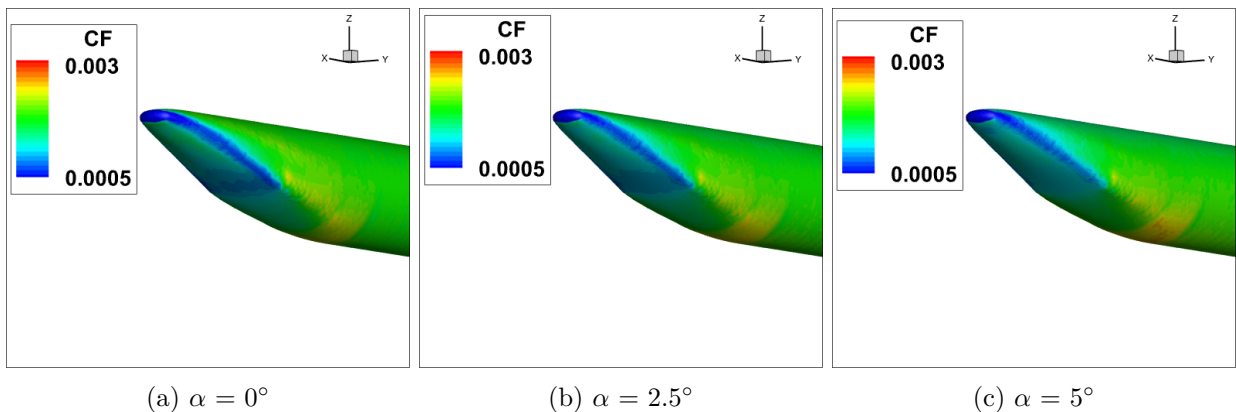


Figure 12.8: Fuselage skin friction coefficient distribution in ramp region for different body pitch angles

While operating at high body pitch angles proves to be aerodynamically favorable, drag penalties of other components attached to the fuselage must also be considered. In particular, spsonsons and turbofans will pitch with the fuselage, generating more drag at a higher angle of attack. The drag of the turbofan does not change significantly with higher degree angles of attack. The drag penalty was accounted for approximately with a 10% increase in drag per each degree increase in the angle of attack [13]. Since the spsonson was modeled as a symmetric airfoil, their drag is highly influenced by the body angle of attack. In addition, a higher pitch angle resulted in a more negative wing set angle. This proved to be unfavorable at slow



speeds when a high wing pitch angle is needed to generate lift, the fuselage pitch angle may tilt up to  $5^\circ$ , depending on the body pitch angle chosen for the cruise. Lastly, a larger body pitch of the fuselage reduces the axial component of thrust offered by the turbofan. At larger pitch angles, more thrust would be required from the turbofan engine to reach the cruise requirement. After studying different orientations of the vehicle in cruise, a  $2.5^\circ$  pitch angle with a sponson set angle of  $-2.5^\circ$  for a  $0^\circ$  incidence angle was selected.

A  $2.5^\circ$  fuselage pitch angle with a sponson set angle of  $-2.5^\circ$  mitigated the effect of sponson drag while preventing the high pitch angle the body would otherwise experience at low speeds. It also reduces the pitching moment as can be seen in Table 12.3. At this body pitch angle, the wing is set an angle of  $-2.84^\circ$  with respect to the fuselage,  $-0.34^\circ$  with respect to the free stream, to provide the proper lift in cruise, as stated in Section 8.

The airframe equivalent areas for the different operating conditions are reported in Table 12.3. This table analyzes strictly the airframe, neglecting all external surfaces including wings, rotor systems, and propulsion mechanisms. A 3% increase in airframe drag is used to account for the installation of the turboshaft engines into the airframe structure. A technology factor of 5% is used to account for the turbofan exhaust weakening the strength of the trailing vortices.

Table 12.3: Fuselage Angle of Incidence Comparison

Angle of Incidence	$L/q - ft^2(m^2)$	$D/q - ft^2(m^2)$	$M/q - ft^3(m^3)$	$Y/q - ft^2(m^2)$
$\alpha = 0^\circ$	-15.3430(1.4254)	7.0880(0.6585)	-231.7498(6.5624)	-0.0864(0.0081)
$\alpha = 2.5^\circ$	-9.5969(0.8916)	5.9435(0.5522)	46.3129(1.3114)	0.1564(0.0044)
$\alpha = 5^\circ$	-4.8617(1.4254)	5.3542(0.4974)	-231.7498(6.5624)	-0.0864(0.0081)

## 13 Vehicle Performance

### 13.1 High-Fidelity Drag Estimation

To estimate *Arion's* flat plate area, the vehicle was divided up into seven parts: fuselage, wing, rotor pylon, tail section, engine nacelles, sponsons, "Miscellaneous" drag for antennas, door handles, and skin gaps, and interference drag between components. Table 13.1 shows the flat plate areas for each vehicle component in cruise. The methods used to estimate the drag on each component and interference drag are as follows:

- **Fuselage:** The fuselage drag was calculated using in-house 3D RANS flow solver Mercury Framework [38]. Discussion on the refinement of the fuselage shape based on 3D CFD results is found in Section 12. Drag in cruise is largely due to pressure drag on the nose and vortices due to suction from the ramp geometry behind the vehicle. Different body pitch angles were investigated and corresponding flat plate drag areas are reported in Table 12.3. Fuselage drag accounts for the installation of the turboshaft in the airframe structure with a 3% increase in total fuselage drag. A technology factor of 5% is used to account for the turbofan exhaust weakening the strength of the trailing vortices.
- **Wing:** The wing drag estimation was also calculated using 3D RANS CFD. Because performance estimates outside of the 450 kt cruise condition needed a model for the wing at various angles of attack, 2D airfoil tables were also generated in CFD, and the estimation of induced drag used is based on lifting line theory adjusted empirically based on the CFD drag estimation on the wing. The interference drag between the fuselage-wing junctions was estimated using methods presented by Prouty [13].
- **Rotor pylon:** The rotor pylon drag estimation in airplane mode was calculated using Ansys Fluent simulations.



- **Tail section:** The tail section drag was calculated based on airfoil tables generated by 2D RANS CFD. A NACA 0012 airfoil is modeled with 20° sweep for the vertical tail. The horizontal tail uses a NACA 0009 airfoil with 20° sweep. A less thick airfoil is sufficient as there are lower structural loads compared to the vertical tail. The reported drag coefficient is at an effective Mach number of 0.7 in cruise and at a flow incidence angle of 0°.
- **Engine nacelle:** The turbofan engine nacelle drag is estimated using an empirical method reported by Prouty [13]. The drag coefficient is determined based on the diameter of the nacelle and its distance to the fuselage, with nacelles closer to the fuselage having higher interference drag.
- **Sponsons:** The sponson was designed based on a NACA 0012 airfoil. 2D RANS CFD was used to calculate the drag coefficient at 0° angle of attack, capturing the cruise body pitch angle.
- **Wing Interference Drag:** In an estimation given by Prouty [13], the drag of wing junctions can be approximated using the wing thickness. Thicker airfoils as well as concave geometries will increase interference drag. Interference drag was calculated for the main wing, the vertical tail, and the sponsons. The sponson is expected to add more interference drag due to the concave blend to the fuselage.
- **Miscellaneous:** The miscellaneous parts include the drag associated with the antennas, door handles, and skin gaps, which were modeled based on Prouty [13].

Table 13.1: Drag breakdown

Component	Drag Coefficient ( $C_D$ )	Flat Plate Area - $ft^2$ ( $m^2$ )	% Contribution
<b>Fuselage</b>	0.08753	5.9472 (0.5525)	28.14%
<b>Main Wing</b>	—	—	—
Wing Drag (CFD)	0.08775	6.0927 (0.5660)	28.83%
Wing Interference Drag	0.10000	0.2877 (0.0267)	1.36%
<b>Turbofan Engine Nacelles</b>	0.12000	2.0944 (0.1946)	9.91%
<b>Two Rotor Pylons</b>	0.32000	2.0106 (0.1868)	9.86%
<b>Tail Section</b>	—	—	—
Horizontal Tail Drag (CFD)	0.00913	0.8769 (0.0815)	8.63%
Vertical Tail Drag (CFD)	0.00814	1.8234 (0.1694)	4.15%
T-Tail Interference Drag	0.09000	0.1836 (0.0171)	0.87%
<b>Sponsons</b>	—	—	—
Sponson Drag (CFD)	0.00992	0.6106 (0.0567)	2.89%
Sponson Interference Drag	0.10000	0.6319 (0.0587)	2.99%
<b>Miscellaneous</b>	—	0.5000 (0.0465)	2.37%
<b>Total</b>	—	21.0589(1.9564)	—

The vertical drag coefficient and equivalent flat plate drag area for each component are reported in Table 13.2. The vertical drag was measured assuming the vehicle is in helicopter mode. Methods based on Prouty [13] and Hoerner [40] were used to estimate the vertical drag coefficients. The wing, horizontal tail, and vertical tail were approximated as 3D flat plates, while the fuselage, turbofan engine nacelles, and sponsons are approximated at cylinders. According to Anderson [41], drag coefficients of bluff bodies were measured using the frontal area as the reference area.

## 13.2 Vehicle Download

A measure of hover performance for tiltrotor aircraft is the download of the rotor wake on the wing. In hover, the rotor must already produce enough thrust to overcome the weight of the vehicle in addition to any the down-force due to the aerodynamics of the fuselage and rotor wake. Particularly in tiltrotors



Table 13.2: Vertical Drag breakdown

Component	Drag Coefficient ( $C_D$ )	Flat Plate Area - $ft^2$ ( $m^2$ )	% Contribution
Main Wing	1.17000	449.2270 (52.2412)	38.01%
Fuselage	0.85000	514.5390 (47.8022)	34.78%
Two Rotor Pylons	0.35000	2.1991 (0.2043)	4.06%
<b>Tail Section</b>	—	—	—
Horizontal Tail Drag (CFD)	1.17000	262.0800 (24.3480)	0.17%
Vertical Tail Drag (CFD)	1.17000	6.4664 (0.6008)	17.71%
Turbofan Engine Nacelles	0.75000	60.0000 (5.57418)	0.44%
Sponsons	1.17000	71.4350 (6.6365)	4.83%
Total	—	1,479.35 (137.4364)	—

these downloads have a significant effect due to their higher disk loadings, hence higher downwash speeds, and larger affected wing area compared to conventional helicopters. Based on the XV-15 hover data, rotor wake download can cause a penalty in hover between 5-15% of the GTOW [42].

To minimize the effect of the prop rotor wake impinging on the wing, tiltrotors commonly utilize trailing edge flaps that deflect the wake downward to reduce the planform area of the wing exposed to the rotor wake. Rotor wake effects, such as induced velocity and rotor wake area, on the wing, are found using momentum theory along with a prescribed wake model. With no deflection, we can see a download factor of approximately 0.13, which is 13% of GTOW. This is a product of higher rpm in hover and large rotors, increasing the wing area affected by the rotor wake. Based on vertical drag coefficients from XV-15 hover tests [42], the optimal flap conditions can be found to minimize download as the percentage of thrust is reported for various locations and deflection angles of the trailing edge flap. Figure 13.1 shows as flap deflection increases, we see a significant drop in the download factor, with a minimum download occurring at  $72^\circ$ . Beyond this point, the flaperon will be deflected at too large of an angle, causing flow separation to be a highly dominant form of drag. With a reduction in planform area by incorporating a flap occupying 30% of the wing chord and designed to deflect down  $72^\circ$  in hover, the *Arion* is able to reduce the download factor significantly to 7.1%.

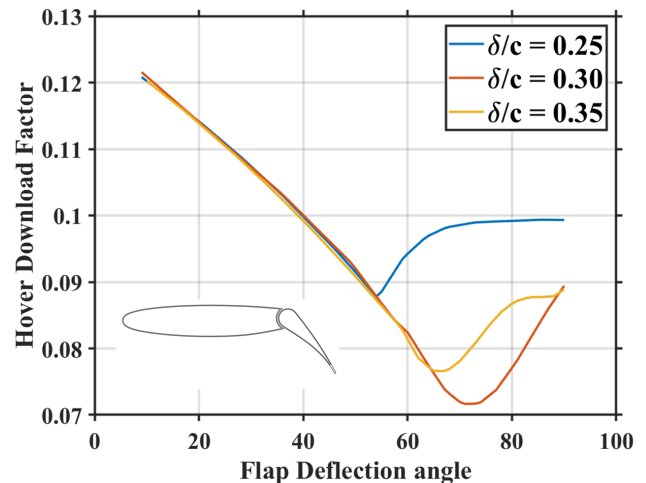
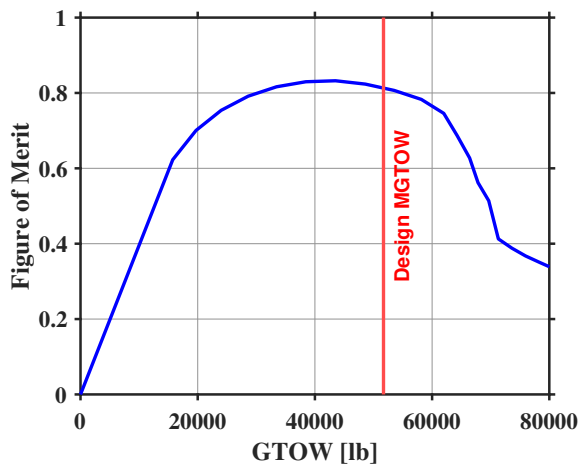


Figure 13.1: Hover download as a percentage of gross weight for various flap configurations in hover

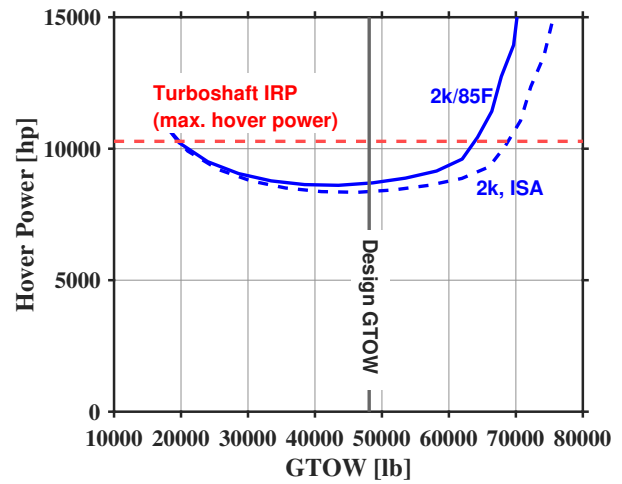
### 13.3 Hover Performance

While the *Arion* spends the majority of its time in forward flight, it is unlike any other vehicle in its size and speed class due to its ability to hover. *Arion* was designed to hover at 2,000 ft (610 m), ISA+18.4°C (2k/85°F conditions) for at least two minutes during takeoff and landing and at the mid-mission point, as required by the RFP. Although the hover during takeoff is a Hover In Ground Effect (HIGE) as per RFP, the aircraft was designed to Hover Out of Ground Effect (HOGE) to provide conservative performance standards for certification. The turboshafts are sized with an installed power capable of providing 110% of the required hover Intermittent Rated Power (IRP) at 2k/85°F conditions as discussed in Section 5.6,



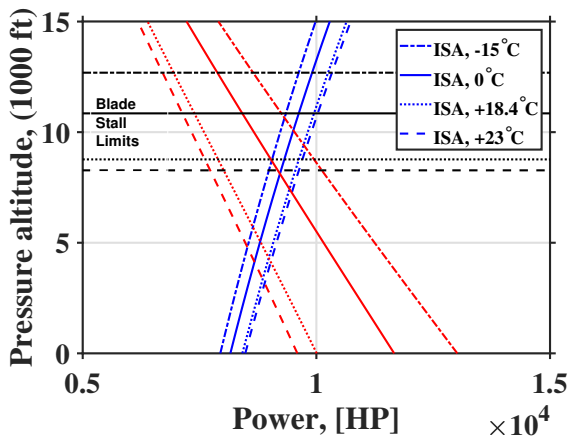


(a) Figure of merit versus gross takeoff weight at 2k/85°F conditions

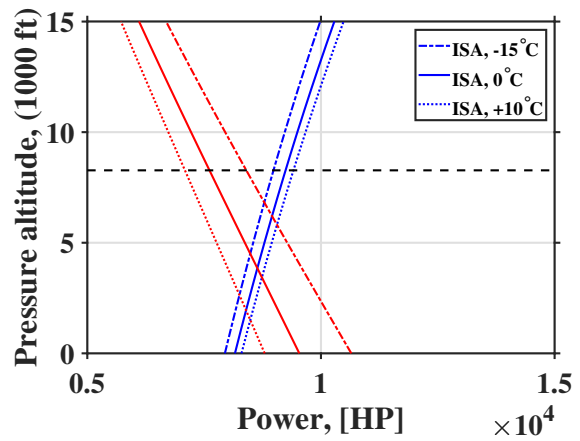


(b) Hover power versus gross takeoff weight at 2k/85°F conditions

Figure 13.2: HOGE performance curves at 2000 ft MSL and 85°F.



(a) Power rated for IRP



(b) Power Rated for MCP

Figure 13.3: HOGE power required (blue) and power available (red) for various ISA conditions

allowing for hover performance at higher and hotter conditions. A 5% increase in turboshaft engine power was added for additional losses due to engine installation. Hover performance in the required 2k/85°F atmospheric conditions is shown in Figure 13.2. The Figure of Merit at the design maximum GTOW of 48,098 lb is 0.813, and the power required is 8690 hp.

The RFP and further judge clarifications emphasize that the vehicle should be designed for highly contested zones and search and rescue operations. Many of these missions require hovering near high-altitude terrain, so the ability to hover at higher altitudes is a critical design feature. Figure 13.3(a) shows the power required to hover and power available as a function of pressure altitude for various ISA conditions. During HOGE at 2k/85°F conditions (the design point given by the RFP), the Intermittent rated power available for hover is 10,572 hp (7,884 kW). The power required to HOGE increases with altitude and increasing temperature. At MGTOW, *Arion* has the capability of hovering at a pressure altitude over 3,473 ft (1,059 m) at ISA+18.4°C conditions or 2,303 ft (702 m) at ISA+23°C. At standard atmospheric conditions (ISA) *Arion* is capable of hovering as high as 8,177 ft (2,492 m). The altitude at which rotor blade stall will occur



prior to achieving sufficient hover lift is also illustrated on Figure 13.3(a); however, these are well beyond the achievable hover altitudes at each ISA condition. *Arion* performs well in hot and high conditions, providing it with multi-mission capability and ample safety margins in highly contested zones. In addition, *Arion* has the capability to hover for extended periods of time as shown Figure 13.3(b). The maximum continuous power (MCP) of the turboshaft engines provides for continuous hover at ISA+10°C *Arion* up to an altitude of 1,506 ft (460 m). On a standard day, at ISA conditions, the maximum continuous hover altitude increases to 3,850 ft (1,173 m), allowing prolonged hovering operations such as search and rescue.

Figure 13.4 illustrates the maximum takeoff altitude of *Arion* as a function of GTOW for various temperature conditions. The maximum takeoff altitude is defined as the altitude when HOGE requires the intermittent rated engine power. At the design MGTO condition, *Arion* can hover at a maximum altitude of 3,473 ft (1,059 m) when operating in ISA+18.4°C, equivalent to 2k/85°F condition stated by the RFP. The excess engine power required for efficient cruise offers extraordinary performance in hover. When operating with only 5,000 lbs of payload and fuel, hover altitudes above 15,000 ft (4,572 m) are achievable. Furthermore, if conditions permit, *Arion* can be loaded beyond MGTO, and still be capable of low-altitude hover. Although designed as a high-speed vehicle, *Arion's* heavy lifting performance also excels in hover.

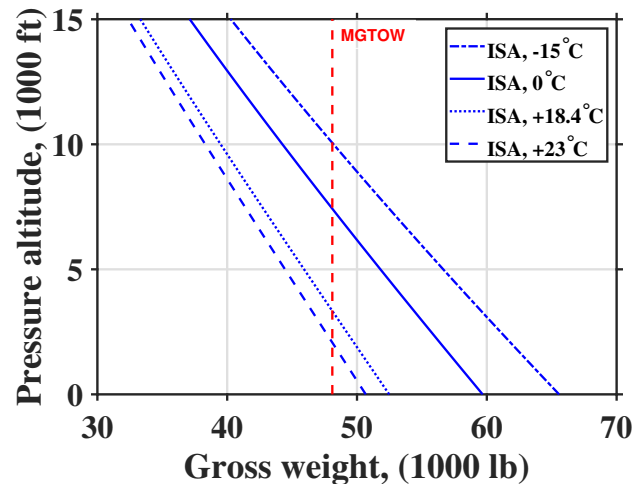


Figure 13.4: Maximum HOGE altitude vs. GTOW for various of ISA conditions

### 13.4 Performance in Airplane Mode

Cruise performance was predicted using an in-house performance model that trims the vehicle for forward flight incorporating the rotor BEMT model. The trim procedure for airplane mode iterates to determine trimmed aircraft pitch attitude, prop rotor and turbofan thrust required, and engine power settings for a given velocity. Figure 13.5 shows the turbofan thrust required versus the altitude at 450 kts cruise. Thrust available varies little with ISA temperature offset, so only a single line is shown. Typically, higher cruise altitudes correspond to less drag due to the decrease in air density, however, the cruise Mach number will also increase with altitude leading to compressibility effects. Additionally, at higher altitudes, available thrust decreases due to the change in ambient conditions. The altitude chosen for the mission is 25,000 ft (7,620 m) because it will not require additional turbofan weight and also provides margin so the mission can be completed even on a cold day.

Airplane mode performance was estimated based on drag estimates discussed in Section 13.1. During cruise, the Vehicle Management System (VMS) automates power sharing between the prop rotors and turbofans. Preference is given to the prop rotor in trimmed flight due to their superior fuel efficiency. When the turboshafts reached Maximum Continuous Power (MCP), the VMS commands turbofan thrust to augment the turboshaft engines. Because the prop rotors are very inefficient at lower thrust and power settings, maximum fuel economy is achieved by allowing the turboshafts to maximize their power prior to engaging the additional thrust. Prop rotor propulsive efficiency for a 450 kt cruise at 25,000 ft (7,620 m) ISA at MCP is 68.5% as shown in Figure 13.7.

The lift-drag ratio  $L/D$  is a common full-vehicle aerodynamic efficiency metric and is defined as:

$$\frac{L}{D} = \frac{L}{P/V} \quad (4)$$



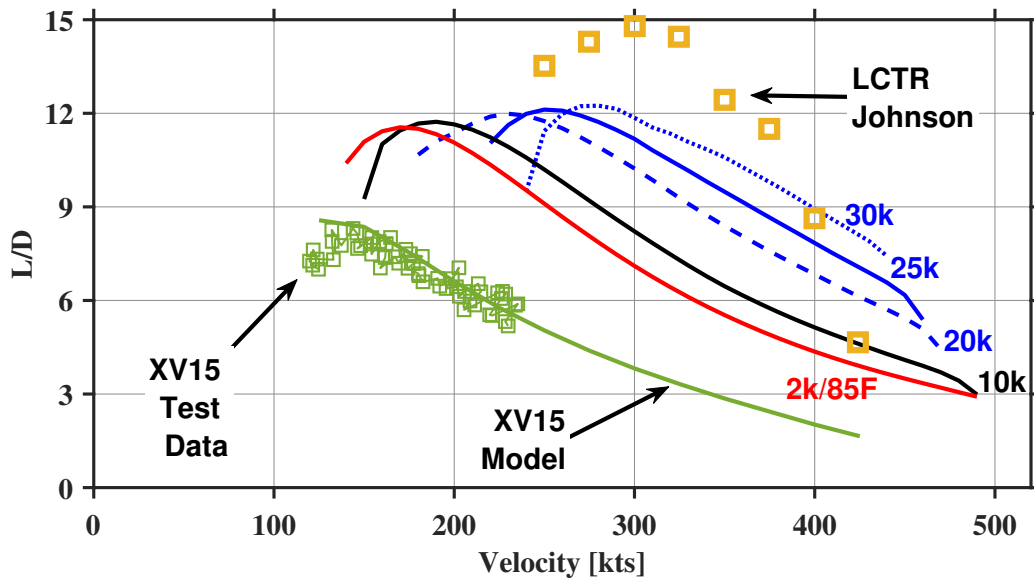


Figure 13.6:  $L/D$  vs. Velocity. ISA conditions within RFP requirement of 20k ft (6,096 m) or greater (blue), 10k ft (3,048 m), ISA (black), and 2k/85°F (red) are displayed. Flight test data from XV15 along with the analytical model, and LCTR analytical predictions are also shown [1]

$L/D$  versus speed is plotted in Figure 13.6 for the *Arion*. XV15 flight test data and matching analysis using the design team’s performance modeling code are shown to demonstrate validation of analytical methods. LCTR predictions from Johnson [1] are also shown. *Arion* is capable of achieving speeds higher than the LCTR by supplementing rotor thrust with turbofan thrust. Cruising at high altitudes increases  $L/D$  but decreases engine performance so the speed is limited to 440 kts at 30,000 ft (9,144 m). At the selected cruise altitude of 25,000 ft (6,096 m), an airspeed of 460 kts is achievable with an  $L/D$  just below 6. The high-speed penetration portion of the mission must be flown at 2k/85°F conditions. Although the vehicle was designed for a 450 kt high-speed penetration segment, maximum performance velocity at those conditions is 490 kts. Furthermore, there is ample space for the extra fuel required to fly at this speed, so the customer may consider faster high-speed penetration segments for a small range penalty.

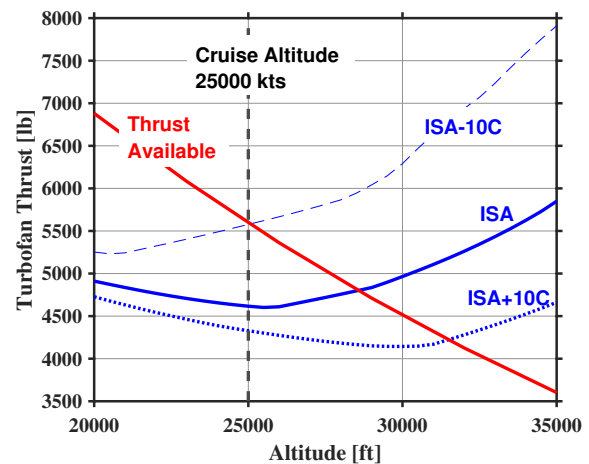


Figure 13.5: Turbofan Thrust 450 kt cruise.

Maximum  $L/D$  is around 12 and is achieved between 180 kts and 280 kts depending on altitude, as shown in Figure 13.6. To demonstrate the flexibility of the design for various missions, cruise speed versus range for *Arion* is shown in Figure 13.8(a) at different flight conditions. Although *Arion* is designed to fly for 1,000 nm (1,852 km) mission with a 450 kt cruise speed split into two legs, the range can be maximized by flying at lower speeds. A range of greater than 2,500 nm (4,630 km) can be achieved with a 20-minute fuel reserve by flying at cruise speeds of between 150 kts and 300 kts depending on altitude. Figure 13.8(b) shows the maximum range that can be achieved at the optimal airspeed at altitudes between 2,000 to 30,000 ft (610 to 9,144 m). Flying at 10,000 ft (3,048 m) MSL provides the absolute best range of 2,562 nm (4,745 km) at 180 kts, but flying higher at 30,000 ft (9,144 m) offers speeds of nearly 300 kts while



only reducing the range to 2,480 nm (4,593 km) which is a 42% decrease in mission time for a 3% range penalty.

Cruise speed versus endurance for *Arion* is shown in Figure 13.9(a) at different flight conditions. Endurance can be maximized by flying at airspeeds significantly slower than the RFP where fuel burn is minimized. Depending on the altitude required for the mission, an optimal airspeed can be flown to provide nearly 17 hours of endurance with a 20-minute fuel reserve. Figure 13.9(b) shows the maximum endurance that can be achieved at the optimal airspeed at altitudes between 2,000 to 30,000 ft (610 to 9,144 m).

Flying at lower altitudes and airspeeds generally provide the best endurance, but sub-optimal altitudes up to 30,000 ft (9,144 m) still can be flown optimally with an endurance of over 9 hours. Maximum endurance profiles are flown with the turboshaft engines providing all of the thrust due to their superior fuel efficiency. Consequently, the turbofan engines are idling for maximum endurance profiles, which has little impact on fuel consumption. The endurance profile can be further extended by keeping the turbofan engines off. The extremely long endurance capabilities should rarely require such a measure. Aircraft commanders may balance mission requirements with the added risk of a failed in-flight engine start attempt to decide if it is necessary. The long endurance time will permit *Arion* to remain on station while conducting search and rescue or airborne command and control missions requiring long loiter times.

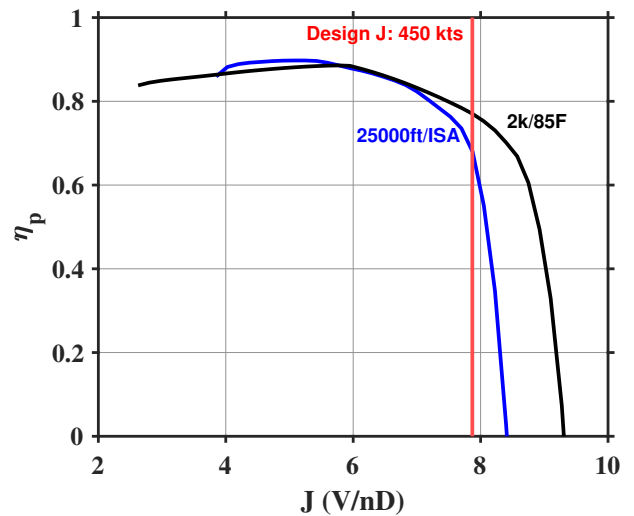
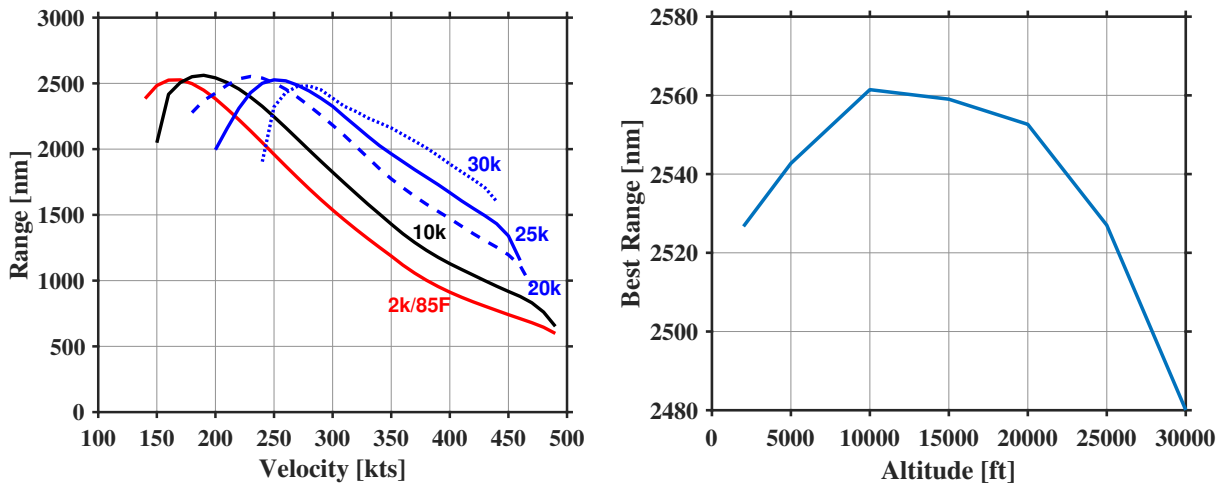


Figure 13.7:  $\eta_p$  versus propeller advance ratio



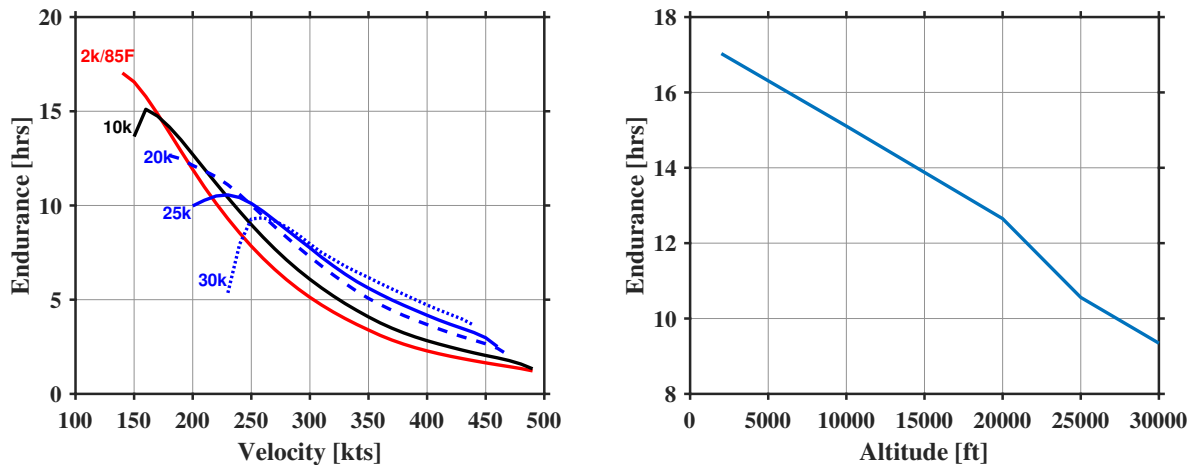
(a) Range vs. Velocity with 20 minutes reserves at several altitudes (b) Maximum range vs. altitude with 20 minutes reserves in mission conditions: atmospheric ISA, ground at 2k/85°F

Figure 13.8: Range Performance of *Arion*

The best climb velocity of the *Arion* is 275 kts for all altitudes. Because the turbofan is sized to overcome the very high drag in cruise, and the turboshaft is sized for hover, the vehicle is tremendously overpowered at mid-envelope airspeeds, providing a large excess power for climb. Maximum climb rate vs. ISA altitude



from 2,000 to 30,000 ft (610 to 9,144 m) is shown in Figure 13.10(a). The climb rate was a maximum of 9,800 ft/min (50 m/s) at ground level and decreased steadily to a still generous 2,200 ft/min (11 m/s) at 30,000 ft (9,144 m) altitude. The total time to climb to altitude from 2,000 ft (610 m) is shown in Figure 13.10(b). At the maximum climb performance, it only takes 3.5 minutes for *Arion* to climb from ground level to mission altitude of 25,000 ft (7,620 m), allowing the aircraft to spend more time in optimized high-speed forward flight. A reduced turboshaft-only powered climb can also be performed at the best climb speed below maximum power, taking 13.5 minutes to reach cruising altitude of 25,000 ft (7,620 m). The profile of this climb is steeper at low altitudes, allowing *Arion* to clear an obstacle quickly while also providing good fuel economy, crew/passenger comfort, and cargo safety. Because the RFP mission is in a highly contested environment, the maximum performance climb is used to quickly reach cruise altitudes where the risk from Man-Portable Air-Defense Systems (MANPADS) is minimized.

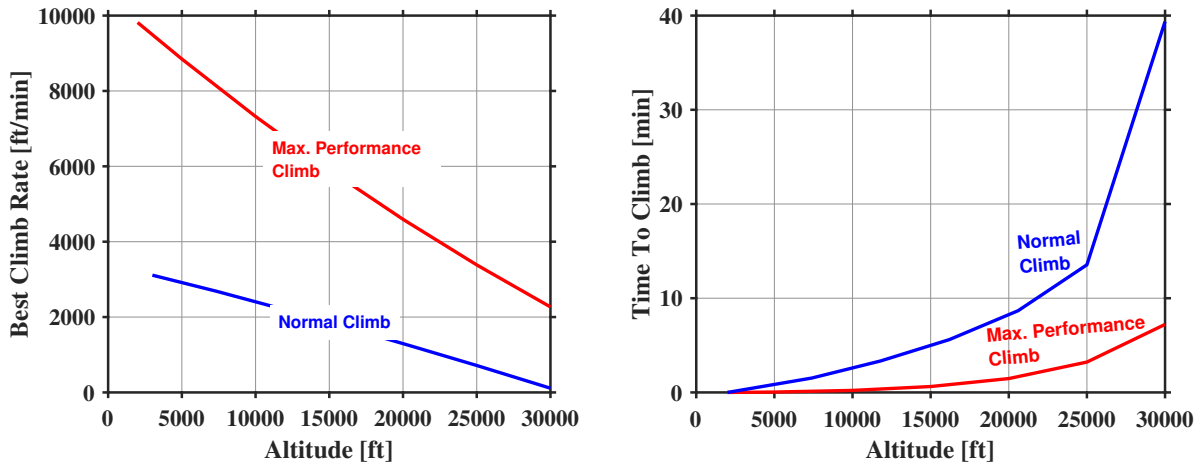


(a) Endurance vs. Velocity with 20 minutes reserves at several altitudes (b) Maximum endurance vs. altitude with 20 minutes reserves in mission conditions: atmospheric ISA, ground at 2k/85°F

Figure 13.9: Endurance Performance of *Arion*

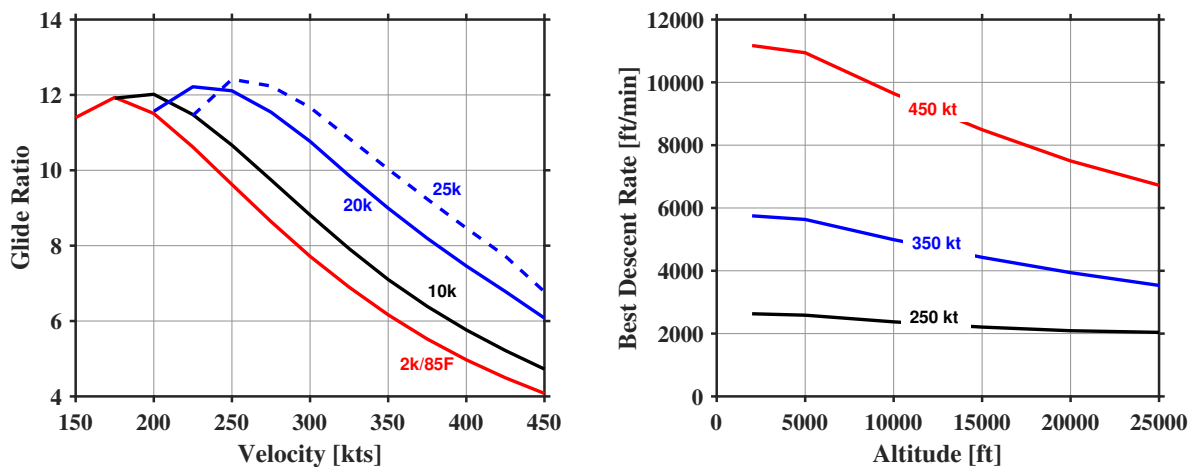
The glide ratio of *Arion* for all several altitudes is shown versus airspeed in Figure 13.11(a). The optimal glide ratio of just over 12 is obtainable at an airspeed between 170 to 250 kts, and it decreases with altitude. This airspeed will be flown in an emergency engine-out situation to maximize the distance toward a safe landing zone. While the VMS will provide optimal glide airspeed recommendations, aviators can also use a rule of thumb such as  $V_{glide} = 160 + 3h$  (where  $h$  is in thousand feet) if VMS power is lost to optimize their return. The descent rate for various airspeeds from 250 to 450 kt is shown in Figure 13.11(b). Slow descents can be accomplished at 250 kts for endurance or range missions, but the RFP mission will descend at 450 kt resulting in glide ratios of 7 to 4 as altitude decreases and descent rates as high as 11,000 ft/min (56 m/s). The faster descent rates will minimize the amount of time the aircraft is potentially exposed to hostile fire before reaching lower altitudes, minimizing enemy detection. The faster descent rate also minimizes the total mission time and fuel burn before the aircraft starts its high-speed, low-altitude penetration profile. Table 13.3 summarizes all the important velocities of *Arion* for the given mission.





(a) Best Climb Rate in feet per minute versus altitude in atmospheric ISA conditions, where ground is at 2k/85°F (b) Time to climb in feet per minute versus cruise altitude in atmospheric ISA conditions, where ground is at 2k85F. Mission altitude can be reached in under 3.5 minutes.

Figure 13.10: Climb Performance of *Arion*



(a) Glide ratio versus glide airspeed at several altitudes (b) Best rate of descent for 250, 350, and 450 kt glide speeds

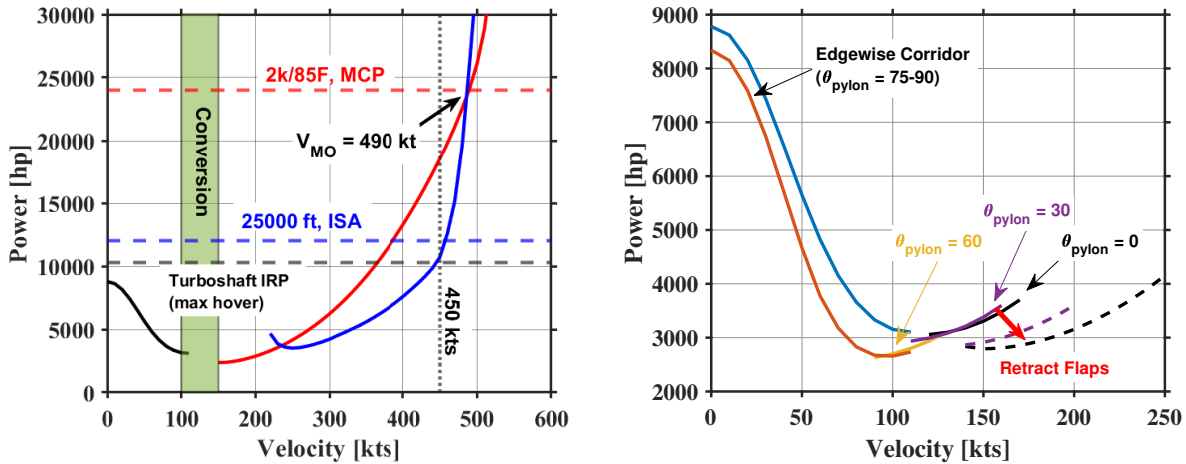
Figure 13.11: Descent Performance of *Arion*

The power profile as a function of airspeed is shown in Figure 13.12(a). Edgewise mode is shown with a black line, and maximum turboshaft hover power (IRP) is shown with a dashed black line. The blue and red lines correspond to airplane cruise mode at 25,000 ft ISA and 2,000 ft, 85°F, respectively. The dashed blue and red lines show maximum available power (MCP) in the cruise condition. The maximum operating speed is 490 kts which can be achieved with full power at a low altitude such as 2k/85°F conditions where engine power is maximized. This is not part of the RFP mission profile, but can be very useful for flight in highly contested environment. Figure 13.12(b) shows the power profile during the conversion sequence. Flight until 100 kts is conducted at pylon tilts from 75-90 degrees vertically with forward pylon tilt requiring slightly lower turboshaft power settings. Beyond 90 kts, the conversion sequence can be completed very quickly with pylon angle lowered as speed increases, and flaps retracted for reduced drag.



Table 13.3: Arion V-Speeds

Condition	Velocity @2k/85°F kts (km/hr)	Velocity @25k/ISA kts (km/hr)
Best range	170 (315)	250 (463)
Maneuvering Speed	308 (259)	472 (874)
Best Climb Performance	275 (509)	275 (509)
Best Endurance	140 (259)	230 (426)
Stall Speed without flaps	140 (259)	198 (367)
Stall speed with flaps	112 (207)	154 (285)
Max Operating	490 (907)	490 (907)
Never Exceed	565 (1046)	565 (1046)



(a) Power vs. velocity at 25,000ft/ISA and 2k/85°F (b) Power versus velocity during conversion. Solid lines: 40 degrees of flaps, Dashed lines: 0 degrees of flaps

Figure 13.12: Power profile versus airspeed

### 13.5 Conversion Sequence

The conversion sequence begins immediately when *Arion* transitions from hover to edgewise flight. The vehicle can be flown to conversion speed in pure edgewise flight using cyclics to maintain a nose-down pitch attitude or by tilting the rotor pylons. In either case, the pylon angle is not recommended to exceed 30 degrees until 80 kts and flight is largely edgewise. As the vehicle gains speed, the wings will offload the rotor, reducing rotor thrust and torque. Edgewise flight performance can be quantified using the metric  $L/D_e$  which is defined as:

$$\frac{L}{D_e} = \frac{L}{(P_i + P_o)/V} = \frac{L}{P/V - F_x} \tag{5}$$

$F_x$  is the propulsive force component generated by the rotor, and its contribution to power is removed from the calculation of rotor effective drag  $D_e$  which is defined as  $P/V - F_x$ .  $L/D_e$  is plotted versus advance ratio  $\mu$  in Figure 13.13.  $L/D_e$  reaches a maximum of 3.75 at an advance ratio of 0.275. Beyond that is well outside of the maximum edgewise speed the vehicle is rated for, and the rotor will experience very high advancing blade loads due to compressibility. Table 13.4 tabulates the breakdown of the  $L/D_e$  calculation.



The conversion corridor for the *Arion* is shown in Figure 13.14 for the cases of with and without flaps. For each pylon angle, the minimum speed is bounded by wing stall and fuselage pitch angle. The maximum speed is bounded by the advance ratio structural limit of 0.3 and advancing blade tip Mach numbers of 0.95. A caution range is defined where the aircraft pitch attitude is approaching wing stall. Pilots are advised to exercise caution in this region because of the small stall margin. The utilization of flaps during the conversion allows flight at significantly lower airspeeds for a given pylon angle; however, the 40° flap setting also imposes a structural airspeed limit of 160 kts. During normal operation, the Vehicle Management System (VMS) will automatically schedule the flap position during conversions to the setting that maximizes the margin to the nearest corridor boundary. The pilot may elect to manually control the flap setting if reduced drag is desired for accelerated conversion or emergency conditions.

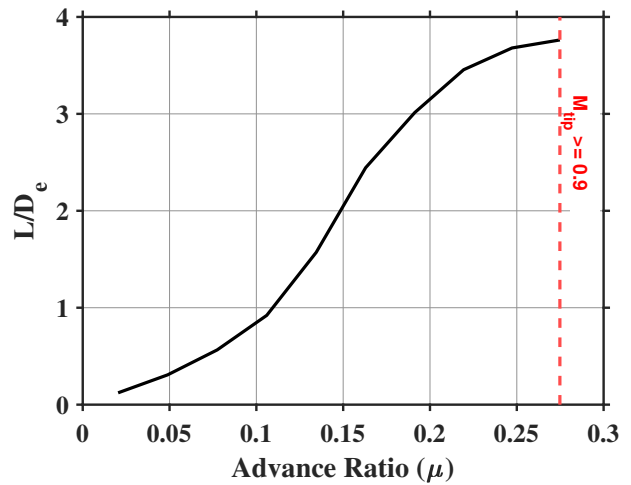
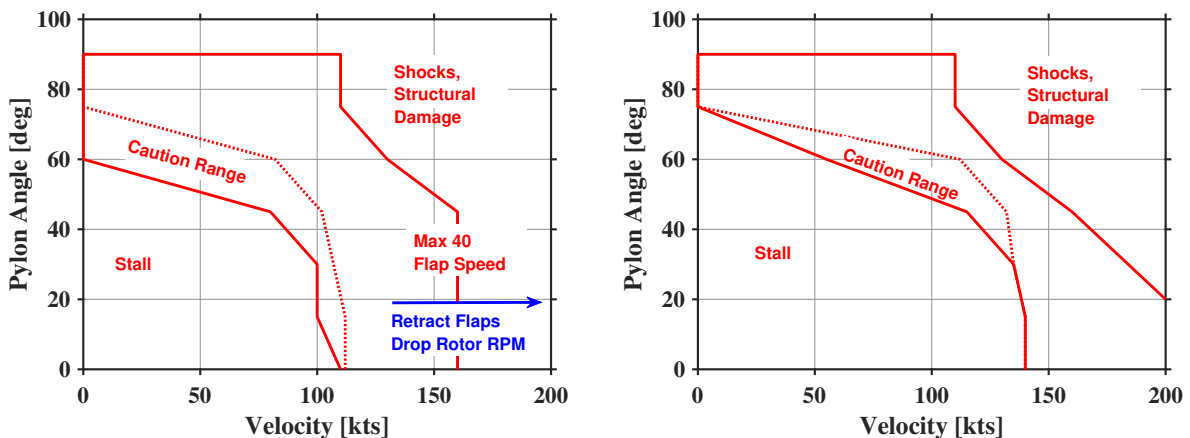


Figure 13.13: Rotor Lift-to-drag ratio ( $L/D_e$ ) variation with advance ratio. Flight beyond an advance ratio  $\mu = 0.275$  is restricted by the VMS to prevent shocks over the rotor blade



(a) Normal conversion corridor for *Arion* shows plenty of margin and a clear path to convert to forward flight. (b) Conversion corridor without flaps. A safe no-flap conversion can be performed with higher pitch angles and corridor is more narrow.

Figure 13.14: Conversion corridor for the *Arion* with full flaps and without flaps

Thrust sharing between the proprotors and turbofan engines during conversion is modulated by the VMS based on the pilot Thrust Control Lever (TCL) and TCL thumb switch inputs. In hover, TCL inputs will command a vertical climb rate with no thrust commanded to the turbofan. To initiate forward flight, the pilot rotates the pylons slightly forward to 85° to initiate the VMS logic to increase airspeed with turbofan thrust.

The VMS-commanded airspeed will follow a predefined, optimized profile that maintains a margin from both sides of the corridor. As the pilot continues to tilt the pylons forward, the VMS continues to maintain the center of the corridor. The speed and aggressiveness of the conversion will be dictated by the rate at which the pilot rotates the pylons, but the pylons will not be allowed to rotate outside of the conversion



Table 13.4: Edgewise Performance Equivalent Rotor Drag Buildup for a Single Rotor

Advance Ratio $\mu$	Velocity <i>kts (km/h)</i>	Lift <i>lb (kN)</i>	Propulsive Force $F_x$ <i>lb (kN)</i>	Torque <i>lbft (kNm)</i>	Hub Tilt <i>deg</i>	Rotor RPM	Rotor Power <i>hp (kW)</i>	Equiv. Drag $D_e$ <i>lb (kN)</i>	$L/D_e$ Ratio
0.0204	10 (18.5)	26,334 (117.1)	15.29 (0.06803)	85,948 (116.5)	0.0333	404.66	6,622 (4,938)	215,777 (959.8)	0.0122
0.0489	24 (44.4)	25,761 (114.6)	87.35 (0.389)	80,158 (108.7)	0.194	404.66	6,176 (4,605)	83,766 (372.6)	0.308
0.0775	38 (70.4)	24,754 (110.1)	216.4 (0.963)	66,654 (90.37)	0.500	404.66	5,136 (3,830)	43,825 (194.9)	0.565
0.106	52 (96.3)	23,386 (104.0)	390.5 (1.737)	53,341 (72.32)	0.960	404.66	4,110 (3,065)	25,368 (112.8)	0.922
0.134	66 (122.2)	21,703 (96.54)	609.8 (2.713)	37,888 (51.37)	1.61	404.66	2,919 (2,177)	13,809 (61.42)	1.57
0.163	80 (148.1)	19,889 (88.47)	855.3 (3.80)	28,631 (38.819)	2.46	404.66	2,206 (1,645)	8,139 (36.20)	2.44
0.191	93.8 (173.8)	18,119 (80.60)	1,116 (4.96)	26,636 (36.11)	3.52	404.66	2,052.2 (1,530)	6,012 (26.74)	3.01
0.219	107.6 (199.3)	16,510 (73.44)	1,384 (6.16)	26,493 (35.921)	4.77	404.66	2,041 (1,522)	4,797 (21.34)	3.44
0.247	121.3 (224.6)	15,383 (68.43)	1,657 (7.37)	28,249 (38.30)	6.14	404.66	2,177 (1,623)	4,189 (18.64)	3.67
0.275	134.8 (249.7)	14,688 (65.34)	1,951 (8.68)	31,481 (42.68)	7.55	404.66	2,426 (1,809)	3,912 (17.4)	3.75

corridor causing a stall or overstress condition. A maximum performance conversion from hover to forward flight can be accomplished in as little as 15 seconds with the augmented thrust capabilities from the turbofan engines managed by the VMS, allowing *Arion* to quickly egress highly contested areas after a troop or cargo insertion or pickup.

As the elevator gains effectiveness, aircraft pitch is phased in to control altitude, and proprotor thrust transitions to controlling airspeed along with the turbofan thrust. Before reaching critical Mach tip numbers on the rotor, the pilot initiates a reduction in the rotor RPM using the two-speed transmission described in Section 10.

Additional information about the control transitions during the conversion can be found in Section 15. At any time, the pilot may split the TCL into two halves to manually control the turbofan thrust independently of the proprotor thrust and pylon angle as shown in Figure 15.1.

## 13.6 Flight Envelope

The flight envelope in helicopter mode is bound by the conversion corridor and load factor limits of +3.5/-1.5. The flight envelope for the vehicle in airplane mode is shown in Figure 13.15 at cruise and high-speed penetration atmospheric conditions. Maneuvering speed is 304 kts at 2,000 ft (610 m) and 85°F (29°C) and 472 kts at 25,000 ft (7,620 m) ISA. The maximum dive speed of the vehicle is 565 kts, which could only be achieved in an extremely steep dive. The climb speed is below  $V_a$  at all altitudes, while the cruise speed  $V_{cr}$  is below  $V_a$  at cruising altitude but not during the high-speed penetration mission.

## 13.7 Mission Performance Data

Each segment of the RFP mission profile is outlined in Table 13.5. The mission starts with ten minutes of idle, followed by two minutes of hover-in-ground effect. Cruise-climb occurs at best climb performance, with a total elevation gain of 23,000 ft (7,010 m) in less than four minutes. Cruise-climb performance is highly dependent upon altitude, therefore to report average power used and available in the climb, power was integrated over the entire climb-cruise segment, and the average is listed in the table. Power available is lower in cruise at 25,000 ft (7,620 m) than in the low altitude penetration segment, however, the specific range is significantly higher at altitude. This is because low density at high altitude results in reduced



Table 13.5: Mission Performance Data

Mission Segment	Atmospheric Condition	Time min	Speed kt	Leg Start Weight lb (kg)	Leg end Weight lb (kg)	Fuel Used lb (kg)	Specific Range nm/(100lb) (kg/km)	Specific Endurance min/(100lb) (kg/hr)	Power Used hp (kW)	Power Available hp (kW)
IDLE	2,000 ft/85°F 609.6 m/29.4°C	10	0	48098 (2,1863)	47,949 (21,795)	149 (67.7)	0	6.71 (0.148)	IDLE	10,280 (7,666)
HIGE	2,000 ft/85°F 609.6m/29.4°C	2	0	47,949 (21,795)	47,825 (21,739)	124 (56.5)	0	1.61 (0.0354)	7,689 (5,734)	10,280 (7666)
Cruise-Climb	ISA <sup>1</sup>	3.8	275	47,825 (21,739)	47,319 (21,508)	506 (230)	3.41 (0.139)	0.744 (0.0164)	13,378 (9976) <sup>1</sup>	13,378 (9976) <sup>1</sup>
Cruise	25,000 ft/-30°F 7,620 m/-34.4°C	57.7	450	47,319 (21,508)	42,718 (19,417)	4,600 (2091)	9.41 (0.383)	1.25 (0.0276)	10,435 (7,781)	12,625 (9,414)
Descent	ISA <sup>2</sup>	2.3	450	42,718 (19,417)	42,703 (19,410)	15.3 (6.96)	113 (4.59)	15.0 (0.331)	IDLE	19,954 (14,880) <sup>2</sup>
High-Speed Penetration	2,000 ft/85°F 609.6 m/29.4°C	6.67	450	42,703 (19,410)	41,701 (18,955)	1,002 (455)	4.99 (0.203)	0.665 (0.0146)	18,318 (13,659)	27,563 (20,554)
HOGE	2,000 ft/85°F 609.6 m/29.4°C	2	0	41,701 (18,955)	41,602 (18,910)	99.3 (45.1)	0	2.01 (0.0443)	7,689 (5,734)	10,280 (7,666)
Cruise-Climb	ISA <sup>1</sup>	3.15	275	41,602 (18,910)	41,178 (18,717)	424 (193)	3.41 (0.139)	0.743 (0.0164)	13,378 (9976) <sup>1</sup>	13,378 (9,976) <sup>1</sup>
Cruise	25,000 ft/-30°F 7,620 m/-34.4°C	58.1	450	41,178 (18,717)	36,625 (16,648)	4,553 (2,070)	9.57 (0.390)	1.28 (0.0281)	10,239 (7,635)	12,625 (9,414)
Descent	ISA <sup>2</sup>	2.0	450	36,625 (16,648)	36,611 (16,641)	13.37 (6.08)	113 (4.59)	15.0 (0.331)	IDLE	19,954 (14,880) <sup>2</sup>
High-Speed Penetration	2,000 ft/85°F 609.6 m/29.4°C	6.67	450	36,611 (16,641)	35,614 (16,188)	997 (453)	5.01 (0.204)	0.668 (0.0147)	18,237 (13,599)	27,563 (20,554)
HOGE	2,000 ft/85°F 609.6 m/29.4°C	2	0	35,614 (16,188)	35,536 (16,152)	77.3 (35.1)	0	2.59 (0.0569)	4,786 (3,569)	10,280 (7,666)
Reserves @V <sub>BR</sub>	2,000ft/85°F 609.6m/29.4°C	20	170	35,536 (16,188)	35,267 (16,031)	269 (122)	21.1 (0.858)	7.43 (0.163)	1,666 (1,242)	27,563 (20,554)
Totals	N/A	176	371	48,098 (47,949)	35,267 (16,031)	12831 (5,832)	8.49 (0.346)	1.37 (0.0302)	N/A	N/A

turbofan performance, but improved efficiency.

Following the cruise segment, a glide descent at 450 kts down to 2,000 ft (610 m) is conducted freewheeling with engines idling. The proprotors provide extra drag, increasing the glide angle and making for a more aggressive dive. According to V-22 pilots the team spoke to, steep descents at high speeds are common in military flying, and may be necessary in a highly contested area. Furthermore, 450 kts is the same speed as the high-speed low-altitude penetration segment, making for a smooth transition from the descent without accelerating. Because power installed was sized to complete the cruise segment at high altitudes where density is low, engine performance is highest during the high-speed penetration segment, which is conducted at 2,000 ft (610 m) and 85°F (29°C). A 2-minute hover out of ground effect segment at the mid-mission point concludes

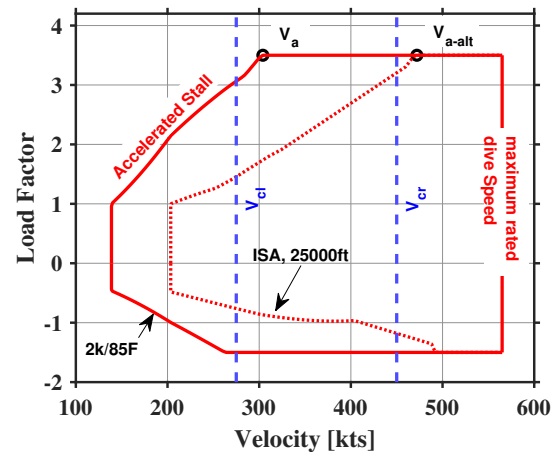


Figure 13.15: Full operation envelope



the mission's first leg. The second leg of the mission is a repetition of the first leg. Mission performance values for the second leg are also shown in Table 13.5. The power required and fuel burn rates for corresponding mission segments are slightly lower in the second leg of the mission than the first due to lower weight from fuel burn during the flight.

Note that the table shows a mission fuel burn of 12831 lb, however 13603 lb of fuel can be loaded to the vehicle allowing for an added 81 nm of range, or 40.5 nm to the Radius of Action (ROA).

## 14 Weight and Balance

### 14.1 Influence of CG Location

The center of gravity (CG) range ultimately places constraints in the design for the placement of equipment in the fuselage. The far rear turbofan engines need to be counterbalanced with the mass forward of the CG. While the RFP specifies the payload CG is centered in the cargo bay, some variation is allowed to enable the crew flexibility when loading cargo.

The placement of the engines, wing, and rotor was varied to select a CG location that would have at least Level 2 unaugmented handling qualities for all approved loading conditions. Additionally, the component placement was selected to have the CG closest to the rotor shaft when the payload and fuel level are at the maximum. The result is that the CG is furthest away from the rotor shafts when there is no fuel or payload. The CG and resulting unaugmented handling qualities improve as more weight is loaded onto the aircraft. Figure 14.2 shows the influence of the aircraft fuel level, payload weight, and payload CG in the cargo bay on the whole aircraft CG. The blue line is the CG variation with no payload on board. The red line and field are the CG variation with 2,500 lb (1,134 kg) payload, and the yellow line and field reflect a 5,000 lb (2,268 kg) payload.

The worst condition of zero fuel weight was considered in determining the allowable payload CG variation. The resulting allowable payload CG within the cargo bay is shown in Figure 14.1. The allowable shift in payload CG is most restrictive when there is a full 5000 lb (2268 kg) load, but the allowable range increases as the payload decreases. For a payload below 1,750 lb (794 kg) the payload CG can be all the way at the forward edge of the cargo bay. A payload of 250 lb (113 kg) or less can be placed anywhere in the cargo bay. This allows a single passenger to sit anywhere in the cabin without the worry of adverse effect on the aircraft CG.

The weight and balance properties of the *Arion* are tabulated in Table 14.1.

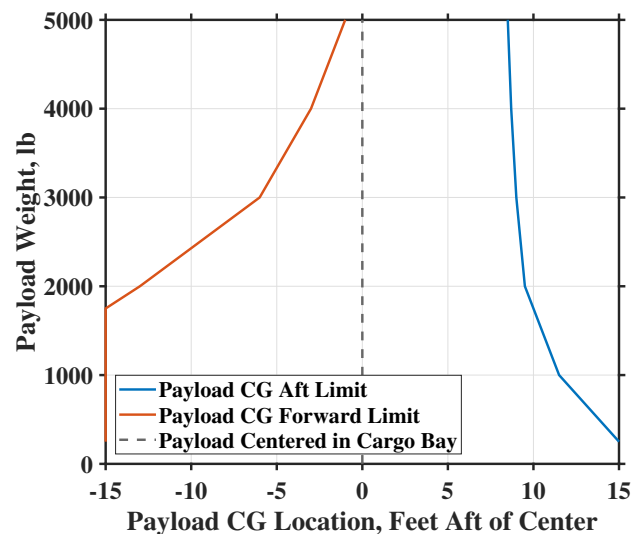


Figure 14.1: Allowable range of payload CG relative to the cargo bay center based on CG analysis with zero fuel weight.



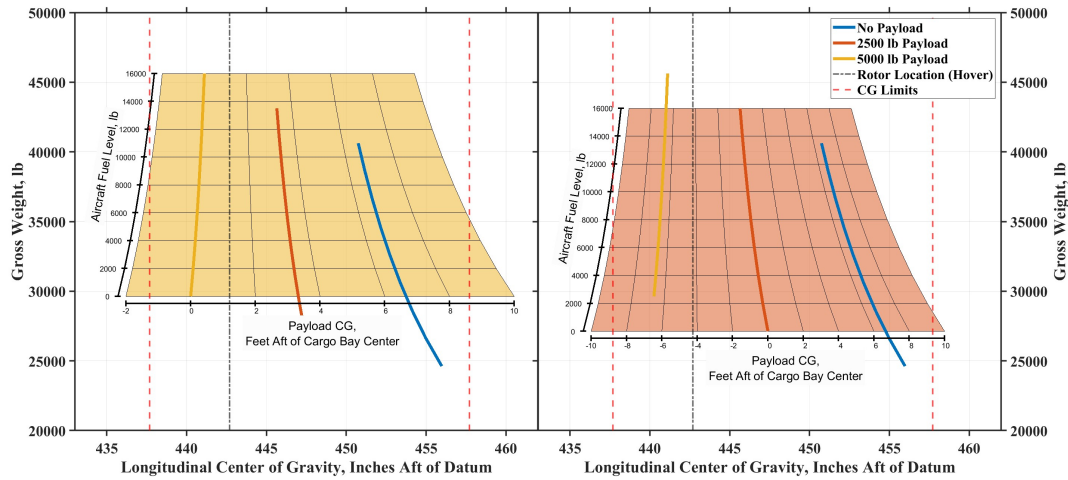


Figure 14.2: Aircraft CG variation within the allowable range due to payload weight (left is 5,000 lb and right is 2,500 lb), payload CG location within cargo bay (sub-axis abscissa), and aircraft fuel level (sub-axis ordinate).

## 15 Flight Dynamics and Controls

### 15.1 Control Strategy Overview

Multi-mode aircraft like *Arion* require a tailored solution when it comes to flight control design. Smartly scheduled automation is essential to optimizing the use of additional control axes without increasing the pilot workload. For the military pilot, the automation must not restrict the flexibility needed to fly the aircraft safely in a constantly evolving battlespace.

*Arion's* tilting side-by-side rotor configuration allows overspecified control of the four primary helicopter aircraft states (roll, pitch, yaw, and heave), allowing the control strategy to constrain additional elements of the aircraft state. Opposed lateral cyclic controls hover downwash angle to increase power margins. The fuselage roll axis and lateral translation are now independently controllable using combinations of lateral cyclic and differential collective pitch. The desired strategy is to have some roll with translation to cue the pilot to the aircraft state and reduce hub loads. Similarly, combinations of longitudinal cyclic and rotor tilt angle allow independent control of longitudinal translation and aircraft pitch. While rotor tilt could be controlled asymmetrically for an additional degree of freedom, it is ruled out from the design due to the risk of a failure condition with asymmetric rotor tilt causing unrecoverable out-of-control flight.

The turbofan engines provide an addition control implement to impose upon the aircraft state. With the turbofan thrust always pointed along the longitudinal axis of the aircraft, forward airspeed can now be developed from a hover prior to rotating the proprotor thrust vector away from vertical. The proprotors will continue to provide more vertical lift for the aircraft while the turbofan engines produce the thrust to accelerate. Unlike standard tiltrotor aircraft, *Arion* will accelerate to gain wing-borne lift prior to reducing proprotor lift, rather than the other way around. This helps ease the cumbersome balance between tilting the rotors too much or too little during takeoff and approach for the standard tiltrotor aircraft.

### 15.2 Cockpit Controls

Each of *Arion's* two pilots has a fully redundant set of aircraft flight controls shown in Figure 15.1. To the pilot, the control implementation will feel very similar to the current operational tiltrotor aircraft.



Table 14.1: Aircraft center of gravity with measurements made from the center of the nose.

Component	Weight (lb)	$x_{cg}$ (ft)	$y_{cg}$ (ft)	$z_{cg}$ (ft)	Weight (kg)	$x_{cg}$ (m)	$y_{cg}$ (m)	$z_{cg}$ (m)
<b>Rotor Group</b>	<b>3,225.4</b>	<b>-30.0</b>	0.0	<b>8.1</b>	<b>1,466.1</b>	<b>-4.3</b>	0.0	<b>2.8</b>
Blades	1,206.0	-28.6		8.1	546.9	-3.9		2.8
Hub & Spinner	2,022.2	-30.9		8.1	919.2	-4.6		2.8
<b>Wing Group</b>	<b>2,839.5</b>	<b>-33.6</b>		<b>7.0</b>	<b>1,290.7</b>	<b>-5.4</b>		<b>2.5</b>
Torque Box Structure	1,484.0	-35.4		8.6	674.5	-6.0		3.0
Flaperons & Fittings	901.0	-39.6		8.4	409.5	-7.3		2.9
Pylon Structure	454.5	-35.0		8.2	206.6	-5.9		2.9
<b>Fuselage Group</b>	<b>10,515.9</b>	<b>-18.9</b>		<b>-0.2</b>	<b>4,780.0</b>	<b>-0.9</b>		<b>0.3</b>
Fore Structure and Skin	1,665.4	-17.7		1.6	757.0	-0.6		0.8
Center Geodesic Fuselage	2,015.1	-30.2		1.7	916.0	-4.4		0.9
Wing & Landing Gear Attachment	1,908.9	-37.5		2.1	867.7	-6.6		1.0
Aft Structure and Skin	1,366.8	-46.6		2.4	621.3	-9.4		1.1
Landing Gear	1,573.0	-37.8		-1.7	715.0	-6.7		-0.2
Ramp Structure	1,986.6	-51.8		-0.2	903.0	-11.0		0.3
<b>Powerplant Group</b>	<b>7,309.6</b>	<b>-43.2</b>		<b>5.2</b>	<b>3,322.5</b>	<b>-8.3</b>		<b>1.9</b>
Turbofans	4,237.2	-62.0		9.6	1,926.0	-14.1		3.3
Turbofan Fittings	98.0	-59.4		7.6	44.5	-13.3		2.7
Turboshafts	2,204.4	-17.5		6.3	1,002.0	-0.5		2.3
Turboshaft Fittings	770.0	-28.6		4.3	350.0	-3.9		1.7
<b>Drive System Group</b>	<b>2,467.5</b>	<b>-30.9</b>		<b>4.8</b>	<b>1,121.6</b>	<b>-4.6</b>		<b>1.8</b>
Main Transmissions	1,821.6	-35.0		6.5	828.0	-5.9		2.3
Intermediate Gears & Crossshaft	96.8	-37.4		7.3	44.0	-6.6		2.6
Main Drive Shafts	95.9	-37.2		8.2	43.6	-6.5		2.9
Terp Two-Speed Transmissions	453.2	-46.0		8.2	206.0	-9.2		2.9
<b>Accessories Group</b>	<b>2,387.5</b>	<b>-22.3</b>		<b>1.5</b>	<b>1,085.2</b>	<b>-2.0</b>		<b>0.8</b>
Anti-icing	501.0	-34.6		6.7	227.7	-5.7		2.4
Hydraulics	299.2	-36.1		6.6	136.0	-6.2		2.4
Cockpit Controls	396.0	-6.3	3.4	180.0	2.9	1.4		
Avionics & Instruments	1,191.3	-2.8	3.1	541.5	4.0	1.3		
<b>Empty</b>	<b>28,745.4</b>	<b>-29.1</b>	<b>5.1</b>	<b>13,066.1</b>	<b>-6.2</b>	<b>1.9</b>		

This is enabled by high levels of automation that command the aircraft to the desired state based on the interpretation of the traditional cockpit controls. The resulting aircraft motion from each control input is contained in the following sections.

The pilot's right hand holds an active side stick. The active feedback in the stick cues the pilot on the aircraft state and helps guide the pilot during maneuvers. Increased stick forces will subtly guide the pilot to avoid stall or airframe over stress and over speed. Variable intensity vibration cues can alert the pilot to impending critical conditions, and stick bumps can call attention to actions that require immediate pilot input.

The pilot's left hand holds a thrust control lever (TCL). The thrust control lever is required to be an analog to both a collective in helicopter mode and a throttle in fixed-wing mode. It is advanced at an upward angle of 20 degrees to prevent control sense confusion between helicopter and airplane mode. The upward angle ensures that an upward arm motion increases altitude in a hover and a forward arm motion increases speed in cruise. The TCL is divided into two halves that normally fit ergonomically into one thrust control that is interpreted by the Vehicle Management System (VMS) to modulate the various engine power outputs. During emergency situations, the pilot can separate the position of each TCL half to independently command turbofan thrust with the left half and proprotor thrust with the right half. The right TCL half incorporates a spring-loaded, variable-rate thumb switch to modulate the rotor shaft tilt angle. At full forward tilt, an additional forward input on the thumb switch also commands the two-speed transmission to transition the rotor speed from hover speed to cruise speed, and vice versa.





Figure 15.1: Cockpit controls including active side stick, split-power thrust control lever, and foot pedals.

The pilot also has two-foot pedals that control the yaw axis in hover and cruise.

### 15.3 Control Mixing

In order for the relatively standard cockpit controls to manipulate all of *Arion's* control actuators, a high level of automation is required to understand the pilot's desire and distribute the inputs to the appropriate actuators. The fly-by-wire control strategy varies throughout the flight envelope as different controls are required to control flight in hover versus forward flight. control and navigation loop control laws will further augment the aircraft to provide additional stability and optimized control as discussed in a later section. A summary of the control mixing logic is presented in 15.1.

Table 15.1: Unaugmented Control Mixing Strategy

Control Input	$\delta\text{Lat}$	$\delta\text{Lon}$	$\delta\text{TCL}$	$\delta\text{Ped}$
Rotor	Lat. Cyclic and Diff. Collective <sup>†</sup>	Long. Cyclic <sup>†</sup>	Collective Pitch	Diff. Long. Cyclic <sup>†</sup>
Control Surfaces	Diff. Aileron	Elevator	–	Rudder
Turbofan	–	–	Thrust*	–

<sup>†</sup>Low speed only \*Phased in with forward rotor tilt

Starting from a hover, pedal inputs affect a yaw change through differential longitudinal cyclic. The opposing longitudinal tip path plane (TPP) and H-forces create an aircraft yawing moment. The reaction also creates opposed pitch moments on each rotor which will create a torsion on each wing that will cancel out in the fuselage.

Longitudinal stick inputs give each rotor the same longitudinal cyclic input. Similar to most helicopters, this input will create a pitching moment on the fuselage that tilts the entire aircraft body; however, this is not the desired control implementation for controlling airspeed. Rather, longitudinal cyclic inputs are better suited in the tiltrotor aircraft for small adjustments to pitch attitude while the rotor shafts tilt independently of the fuselage.



Lateral stick inputs provide a combination of lateral cyclic to each rotor and differential collective pitch. With the high roll moment of inertia of a tiltrotor, the moments from the lateral cyclic are supplemented with the differential thrust from each rotor. The two methods are further modulated by the VMS to make lateral translation possible with a moderate roll angle that provides feedback to the pilot and minimizes lateral hub loads.

TCL inputs in a hover modulate only the combined rotor collective pitch to increase and decrease the aircraft altitude. If the left TCL half is split from the right, the pilot can independently control the turbofan thrust, but that control method is only meant for emergency use. The TCL thumb switch is used to tilt the rotors forward and aft. Larger thumb switch inputs will increase the rate of tilt for the rotor shafts. The TCL thumb switch also indicates the pilot's desire to increase forward speed, and the VMS will schedule turbofan thrust to increase performance on the transition to forward flight.

As the aircraft gains speed and the rotor shafts tilt forward, several transitions take place. Traditional airplane controls are phased in with airspeed and rotor shaft tilt as the control surfaces gain effectiveness. At the same time, cyclic controls are phased out and active rotor flap control is left to maintain minimum TPP tilt to minimize hub loads in forward flight.

As the proprotor thrust becomes aligned with the turbofan thrust, the TCL modulates both simultaneously, favoring the proprotor thrust at slower speeds due to its increased efficiency and adding in turbofan thrust as required to achieve rapid acceleration and high-speed forward flight.

## 15.4 Aircraft Stability

### 15.4.1 Unaugmented Stability

*Arion's* flight dynamics were modeled in MATLAB using a non-linear simulation model with 48 aircraft states including rigid body position, Euler angles, speed, and angular rates, multi-blade rotor flapping, and a three-state Pitt-Peters inflow model for each rotor. The relevant parameters from the BEMT rotor code were reduced for input into the flight dynamics model. The model was successfully trimmed from 20 to 450 kts with varying rotor tilt angles and turbofan thrust settings. The trimmed model was linearized at various points in the envelope and an eigenanalysis was conducted of the residualized 6-degree-of-freedom model to assess the stability at that flight condition.

Initial assessments of *Arion's* original V-Tail configuration showed a phugoid mode that was very lightly damped at 450 kts, but slowing to 250 kts, the mode became oscillatory divergent with a time to double of just 2.7 sec. Additionally, the V-Tail spiral mode was divergent, but it had a much greater time to double of 103 sec.

Rather than continue to increase the size of the V-Tail at the expense of additional drag, a T-Tail configuration was modeled showing stability in all forward flight modes using airfoils of approximately the same size. The increased stability of the T-Tail configuration was a key reason for adopting the configuration on *Arion*. With the T-Tail, *Arion's* flight dynamics model has demonstrated forward flight stability with relative invariance due to changes in airspeed, altitude, and center of gravity (CG). Lateral and vertical CG shifts demonstrated stability when placed anywhere within the confines of the fuselage. Longitudinal center of gravity shifts demonstrated stability exceeding the limits imposed by the hover stability. The T-Tail configuration would also provide some mitigation of the pitch up with sideslip (PUWSS) phenomena seen in the V-22 as the rotor wake will no longer impinge on the horizontal stabilizer [43].

In a hover, *Arion's* longitudinal oscillation mode was divergent oscillatory with a time to double of 4.9 sec and a period of 9.4 sec. The frequency and damping ratio of this mode are just outside of the Level 2 specification for hover oscillations in ADS-33E, resulting in Level 3 handling qualities for the unaugmented aircraft in a hover [44]. Additionally, shifts in the longitudinal CG forward or aft in a hover worsen the



longitudinal oscillation dynamics resulting in shortened time to double. Handling the aircraft under these conditions would result in a high workload and the inability to perform additional tasks for the pilot.

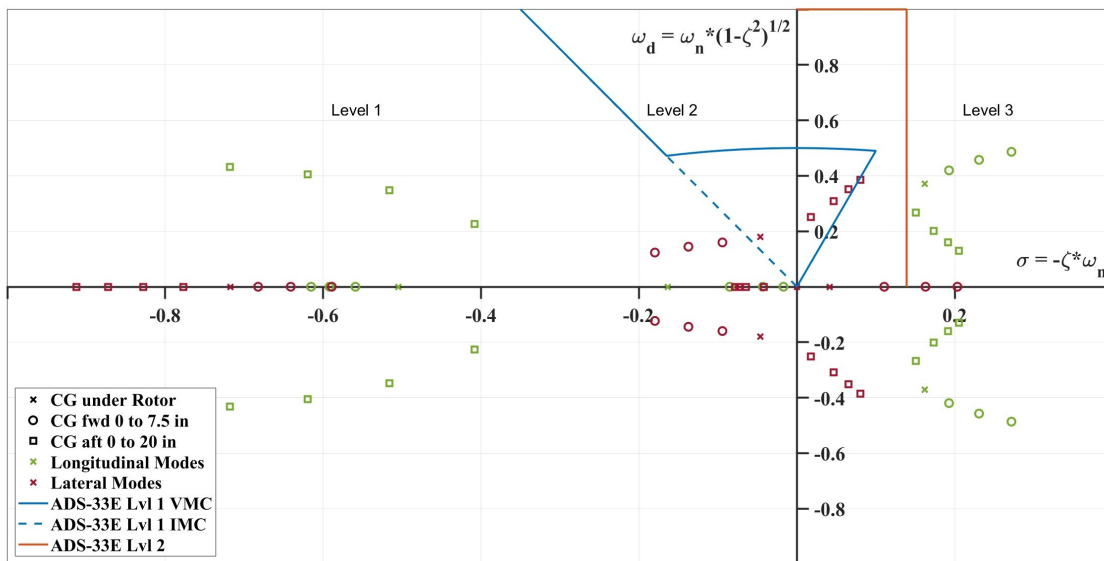


Figure 15.2: Unaugmented Hover Stability Modes. Red symbols are the longitudinal modes, and blue symbols are the lateral-directional modes. Squares reflect CG shifting forward up to 7.5 inches (19 cm) from the rotor shaft. Circles reflect the CG shifting aft up to 20 inches (51 cm) from the rotor shaft.

### 15.4.2 Augmented Stability

To address the poor innate longitudinal hover dynamics, electronic feedback control, particularly pitch rate damping, is considered essential to ensuring the aircraft can be safely operated. Because the failure of the pitch rate damping will result in Level 3 handling qualities, the feedback sensors and computers are designed with redundancy levels to provide for a mean probability of failure of less than  $2.5 \times 10^{-5}$  per flight hour as specified in ADS-33E [44]. The resulting hover stability eigenvalues are shown in Figure 15.3 with the addition of pitch rate damping to the model with electronic feedback control. Additional control and navigation loop augmentation is incorporated at the  $2.5 \times 10^{-3}$  failures per flight hour specification, since their failure will revert to the Level 2 handling qualities afforded by the more robust pitch rate damping system [44].

While all of *Arion's* flight control laws are software-defined, fly-by-wire systems, the system is still split into control loop and navigation loop systems to differentiate between features that increase the short-term rate stability (control loop) and features that enhance the long term flight path stability (navigation loop). Navigation loop inputs to the flight actuators are backdriven into the pilot's flight control inceptors to provide situational awareness of the aircraft maneuver, but control loop inputs are not. Additionally, control loop inputs are limited to about 10% control authority which allows them to be saturated at higher angular rates, providing the pilot with adequate attitude quickness if needed for a high gain maneuver.

The augmentation is incorporated using a dynamic inversion flight control model that effectively inverts the aircraft plant dynamics and allows the scheduling of the desired dynamics on each aircraft axis using a single set of gains to shape the input. The inverted plant dynamics will initially be based on lookup tables of aircraft state based on modeling of the reduced order, six degrees of freedom system which can be easily captured using standard aircraft attitude gyros and accelerometers. A multiple input, multiple output system inversion will ensure the relationships between all axes is captured. The plant will be updated



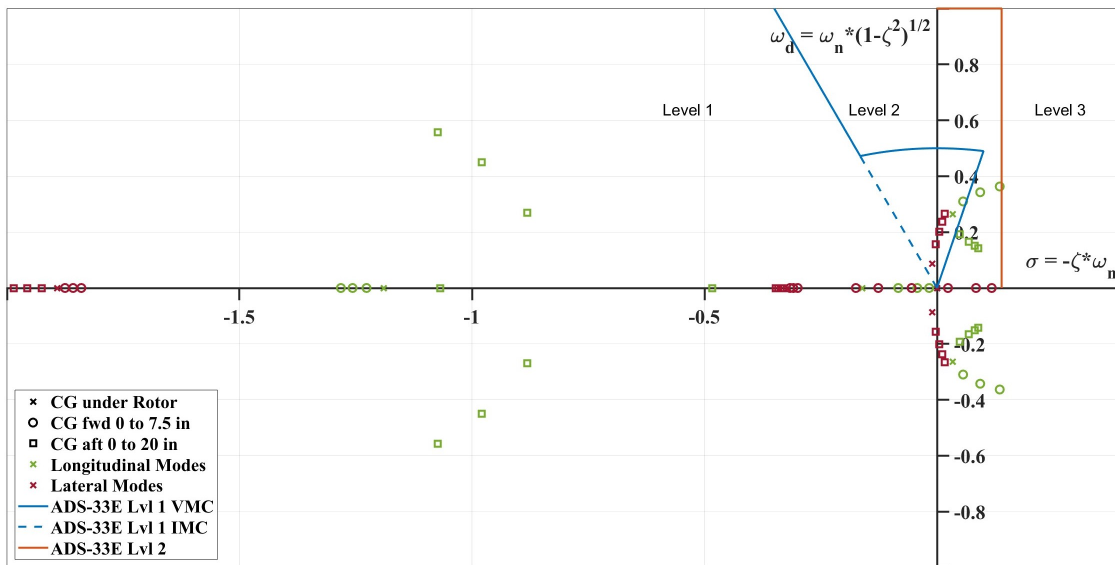


Figure 15.3: Hover Stability Modes with Pitch, Roll, and Yaw Rate Electronic Feedback Damping. Red symbols are the longitudinal modes, and blue symbols are the lateral-directional modes. Squares reflect CG shifting forward up to 7.5 inches (19 cm) from the rotor shaft. Circles reflect the CG shifting aft up to 20 inches (51 cm) from the rotor shaft.

during initial flight testing to ensure optimal plant inversion before release to the fleet operator.

While the Usable Cue Environment (UCE) cannot be fully known without sitting in the aircraft, it is anticipated that the large aircraft will face significant pilot field-of-view challenges. These challenges are addressed with several technologies that increase the pilot’s situational awareness, but the aircraft is still designed with response types required to meet Level 1 handling qualities for the UCE 3 environment and instrument meteorological conditions (IMC). The exact control strategies for each axis vary with airspeed and rotor shaft tilt angle between hover and cruise.

### 15.4.3 Stability Augmentation System - Control Loop

The control loop is further divided into an inner and outer loop.

In hover, the inner control loop of the stability augmentation system is designed to provide attitude command, attitude hold (ACAH) in the pitch and roll axes, rate command direction hold (RCDH) in the yaw axis, and rate command height hold (RCHH) in the vertical axis. The lateral and longitudinal inner loops are wrapped in a Translational Rate Command (TRC) outer control loop in a hover. The TRC dynamic inversion loops output the ideal pitch and roll attitude necessary to command the inner control loop. On the transition to forward flight, TRC outer loop from the lateral and longitudinal stick inputs is phased out.

The RCHH is only active for relatively small TCL inputs of  $\pm 15\%$ . Larger inputs revert to collective pitch command to ensure autorotation and maximum vertical climb profiles are still possible, but the collective pitch is additionally governed by the Engine and Rotor Governing functions provided by the FADECs.

As the aircraft transitions to forward flight, the longitudinal axis transitions to RCAH as the elevator gains effectiveness. The lateral axis remains in ACAH until the rotor shaft has been tilted full forward, then transitions to RCAH. The yaw axis transitions to a sideslip command, turn coordination response type. The TCL transitions to a thrust command between minimum and maximum available, managed by the Engine and Rotor Governing system.



As the traditional fixed-wing control surfaces gain effectiveness, the cyclic rotor controls are phased out and anti-flapping controls are phased in. Anti-flap controls are a feedback-based cyclic control system that null out any flapping caused by the aircraft state and aerodynamics to minimize hub loads and assist in the mitigation of proprotor whirl flutter.

#### 15.4.4 Automatic Flight Control System - Navigation Loop

Programmed around the stability augmentation system is the Automatic Flight Control System (AFCS). The AFCS provides longer-term flight path stability and nulls out steady state inputs by the stability augmentation system to return them to full 10% authority. The AFCS consists of a variety of features that minimize pilot workload throughout the flight envelope.

The AFCS provides position hold in a hover below 3 kts with no stick input. The position hold incorporates the hover position using a fused solution from the Global Positioning System (GPS) solution and from the location in the scene calculated by Landing Zone Situational Awareness, Guidance, and Evaluation (LZ-SAGE) system (discussed in Section 16). If the aircraft is trimmed in a translation above 5 kts, the position hold transitions to vector mode to provide a consistent track over the ground by minimizing cross-track error.

Similarly, in the vertical axis, the AFCS provides altitude hold when the vertical speed is less than 50 fpm (0.254 m/s) and there is no TCL input. The hold defaults to radar altitude (RADALT) when below 500 ft (152 m) AGL and barometric altitude (BARALT) when above, but can be selected otherwise by the pilot. The RADALT hold will follow rising and falling terrain at a constant AGL altitude, and the BARALT hold will follow lines of constant pressure altitude.

The yaw axis in a hover incorporates a heading hold feature when the yaw rate is below  $3^\circ/\text{sec}$ . The hold is based on the heading determined by the navigation system.

During the transition to forward flight, TCL inputs transition from vertical axis control to longitudinal speed control using a Speed Command, Speed Hold (SCSH) response type. The SCSH navigation loop commands a thrust level to the control loop to optimize the transition to the newly commanded speed using a combination of proprotor and turbofan thrust. Once at the desired speed, the Adaptive Digital Automated Pilotage Technology (ADAPT<sup>TM</sup>) program from Piasecki Aircraft Corporation performs a Fly-to-Optimal routine to optimize the overspecified flight controls to maximize speed if at full throttle and fuel efficiency in all cases [45]. The system can also make recommendations to the pilot for optimal altitudes and airspeeds to fly for various profiles, but will not deviate from the currently commanded airspeed or altitude to that end. The commanded speed range of the TCL will range from a minimum speed of 1.2 times the calculated stall speed to the maximum speed achievable for the given environmental conditions, but no more than the never exceed speed. Further reductions in airspeed cannot be commanded with the TCL without tilting the rotor shafts aft using the TCL thumb switch.

The longitudinal stick AFCS in forward flight is a pitch rate command, vertical speed hold response type. With the TCL Speed Hold, the aircraft will not change airspeeds for small changes in aircraft pitch where there is sufficient TCL authority to compensate. If the input is held and the pitch exceeds the TCL authority, the pilot will receive a bump force cue from the active stick, and the stick will transition to an ACAH response beyond the pitch corresponding to the TCL authority limit. The force gradient in the stick will continue to be linear until a pitch is reached which will eventually result in aircraft deceleration to the point of stall. Above the eventual stall pitch, the pilot must pull through a force detent, and then the force further increases with the square of displacement. This region of the control scheme may be desired by the pilot for energy management such as trading airspeed for altitude or turn radius, but holding the aircraft at that pitch will eventually lead to a stall condition. As the aircraft gets below 1.2 times the stall speed, additional cueing to the pilot will be provided including aural stall warnings, forward cyclic bumps,



and increasing intensity stick shaker. The pilot needs only release the stick to no force, and the active stick will return the nose to the maximum pitch attitude for 1.2 times stall with maximum power. The opposite will similarly occur for nose-down pitches to help prevent overspeed conditions. At no point will the pitch controller allow the aircraft to overstress the airframe due to the catastrophic effect of reduced structural integrity to the wing-proprotor dynamic system. This may occur at the expense of a vehicle overspeed condition.

Lateral stick inputs continue to operate as rate command in forward flight with similar increased control forces and cueing as the pilot nears the angle of bank limits.

The heading hold feature remains engaged until a lateral input in the stick or pedal indicates that a turn is desired. When the input ceases and the aircraft returns to straight and level flight, the heading hold will reengage.

#### 15.4.5 Engine and Rotor Governing

The engine and rotor RPM, torque, and collective pitch are additionally governed by an engine and rotor governing control loop to provide the thrust necessary to achieve the commanded inputs. The governing control loop is provided by two redundant Full Authority Digital Engine Controllers (FADEC) on each engine. The FADECs are commanded by the Vehicle Management System as part of the overall aircraft control. Each FADEC is equipped to monitor the status of the engine and the health of itself and its paired FADEC. In the event a faulty FADEC is detected, a disconnect command is issued. If both FADECs on an engine fail, the VMS reverts to backup engine control to provide basic governing for get-home capability.

### 15.5 Flight Simulation

*Arion* was modeled in X-Plane 12 using the native Plane Maker software. While not all of the control and navigation loop stability functions could be incorporated in the Plane Maker software, basic aircraft body angular rate damping was incorporated to assist the pilot in flying the aircraft. The aircraft was flown by a pilot who was able to provide feedback on the design and controllability of the aircraft. Overall, the simulated aircraft was easy to fly and trim in both a hover and in forward flight. Most feedback on flying the simulated aircraft had to do with the simulator setup. Poor peripheral vision cueing in the simulator made it difficult to get a feel for the aircraft drift in hover. This was alleviated greatly by flying the aircraft in the third person view where a very stable hover could be maintained. While motion will be easier to detect in the real aircraft with vestibular motion cues and better peripheral vision, the total field of view from the cockpit is still a major concern. The LZ-SAGE system will be designed to help the pilot orient the aircraft in the environment and provide in-the-loop control feedback to maintain a stable hover [46].

Additional pilot feedback was that the throttle was too sensitive which made it hard to set the precise setting for a hover without climbing or descending. This was corrected somewhat by making the response curve to be more sensitive at the bottom and top of the range and less sensitive in the middle ranges. On the actual aircraft, no adjustments should need to be made to the throttle response curve due to the VMS and FADEC management of the throttle for given TCL inputs and aircraft state.

The transition to forward flight was quick and powerful as the jet engines quickly accelerated the aircraft allowing the rotor shafts to be tilted forward very quickly without losing altitude. There was some increased workload with the longitudinal stick during the transition, but it was still successfully flown with relative ease. The conversion from forward flight back to a hover was more difficult and took some practice to manage the multiple longitudinal axis controls to maintain altitude during the conversion. The automated scheduling of turbofan thrust could not be modeled in X-Plane so there was significantly increased workload on the pilot to manage this thrust in addition to the rotor tilt, rotor collective, and longitudinal stick. This



complication is largely the reason why the transition and conversion process will be mostly managed by the VMS in the final aircraft. While the conversion to a hover took a few practice attempts, *Arion* could be safely flown to a hover and subsequent landing in X-Plane 12.

In forward flight, the aircraft was extremely easy to fly with a good level of precision. The biggest complaint was that the trim ball would frequently be out during maneuvers since the joystick twist axis was inadvertently actuated during pitch and roll maneuvers. For this reason, the actual aircraft will manipulate the yaw axis with foot pedals, not a twisting joystick. A series of stall maneuvers was flown and the aircraft showed favorable stall recovery characteristics, in that there appeared to be no immediate tendency to roll or spin, and the nose naturally dropped back to the horizon as the wings stalled, decreasing the wing AOA. The pilot was able to exercise the precise control needed to fly in tight formation with another model of *Arion* flown autonomously by the computer.

Overall, a full flight was able to be conducted between two landing areas with a full transition to forward flight and subsequent conversion to hover and safe landing in the X-Plane simulation environment.

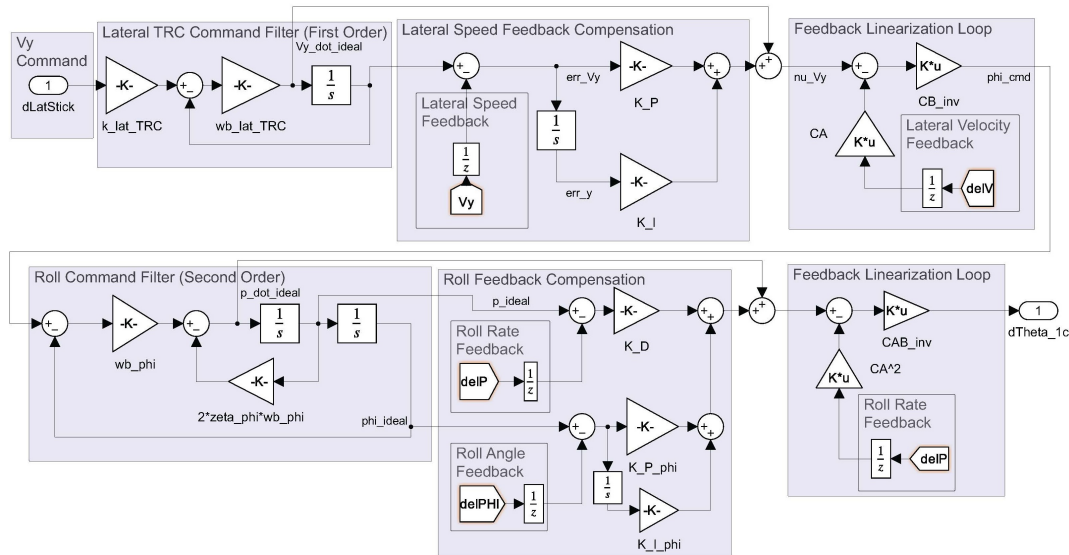


Figure 15.4: Example of TRC DI Inversion for Lateral Stick Inputs in a Hover

Additional modeling and simulation were conducted in MATLAB's Simulink environment. The Simulink environment was used to model Dynamic Inversion control loops to provide translational rate command (TRC) in the aircraft lateral and longitudinal axes, vertical rate command in the vertical axis, and rate command heading hold in the yaw axis. These models were verified with simulated flight control inputs to the model in Simulink. An overview of the Dynamic Inversion (DI) TRC model is shown for the decoupled lateral axis in Figure 15.4. The full DI implementation is a multi-input multi-output (MIMO) model that accounts for the coupled dynamics of the aircraft to provide precise control while minimizing undesirable cross-couplings.

## 16 Avionics System

*Arion* avionics architecture is designed to interface the pilot and crew with the aircraft to reduce workload and enable the best decisions for mission success. A variety of mission profiles and an ever-changing battlespace demand a high level of flexibility to handle any situation, but the flexibility must not be burdensome to the operator's workload. Information presented must be easily digestible and give a clear



understanding to the crew of the required steps to execute accordingly. Similarly, the pilot's ability to command the aircraft must be intuitive and minimize errors.

The Vehicle Management System (VMS) is the brains of *Arion* avionics system. The fully redundant system has two Vehicle Management Computers (VMC) that both continuously operate. One VMC operates as the primary while the other operates as a hot spare. Each VMC continuously monitors the output of the other for anomalies and issues a takeover command if necessary. The VMCs communicate primarily through dual-redundant MIL-STD-1553B data buses to communicate with the various avionics subsystems. An overview of the avionics architecture is shown in Figure 16.1.

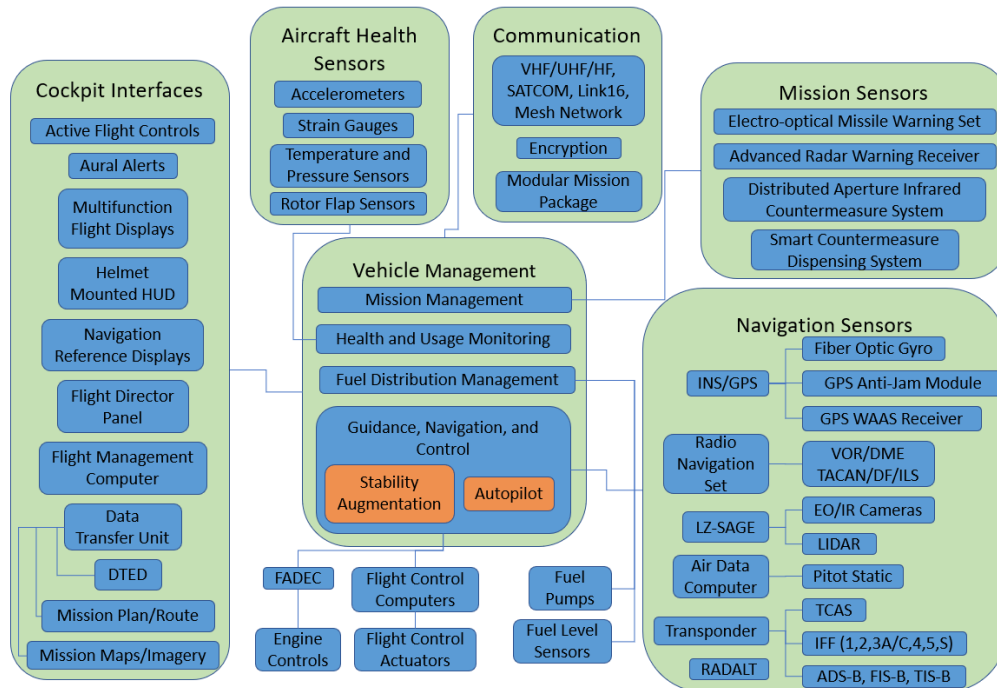


Figure 16.1: Avionics architecture of *Arion*

## 16.1 Guidance, Navigation, and Control

The VMC incorporates Guidance, Navigation, and Control (GNC) software for handling the aircraft flight path. The navigation solution is formed by inputs from the Inertial Navigation System/Global Position System (INS/GPS), digital terrain elevation data (DTED), radar altimeter (RADALT), air data computer (ADC), radio navigation set (RADNAV), transponder including Automatic Dependent Surveillance-Broadcast in and out (ADS-B), and Landing Zone Situational Awareness, Guidance, and Evaluation system (LZ-SAGE). The GNC interfaces with the pilot through the cockpit avionics suite and flight controls to understand the pilot's desired flight path. The GNC also interfaces with the Flight Control Computers (FCC) and Full Authority Digital Engine Controllers (FADEC) to provide inputs to the flight control actuators and engines, respectively.

### 16.1.1 Navigation

The navigation solution comes primarily from two redundant Inertial Navigation System/Global Position System (INS/GPS) navigators which create a fused position solution based on GPS signal and Fiber Optic Gyroscope (FOG) inertial measurements. The military GPS system incorporates Selective Availability, Anti-Spoofing Modules with support for P(Y) and M code GPS signals for the highest integrity and



accuracy. The INS provides the most accurate solution for short-term aircraft motion while the GPS signal is used to periodically synchronize INS solution with the global position. The INS/GPS can operate as a free inertial unit if GPS is lost or GPS only if desired. Heading measurements are provided by the system in true or magnetic. The GPS signal is augmented by the Wide Area Augmentation System (WAAS) and international equivalents for extremely accurate navigation within the National Airspace System and GPS instrument approaches with vertical guidance to qualified locations.

Digital terrain elevation data (DTED) and the radar altimeter (RADALT) interface with the INS/GPS solution to provide the low altitude warning system (LAWS) that notifies the pilot that the flight path is projected to collide with the ground with aural and visual cues that also give guidance on recovery from the adverse state such as, “Pull up” or “Power.” If there are no response or flight control inputs from the pilot, the ground collision avoidance system (GCAS) will attempt to make the required flight control inputs to recover the aircraft.

The air data computer (ADC) is a redundant system that provides inputs to the GNC based on pressure measurements taken from the pitot-static system. The nose-mounted pitot tubes and static ports remain clear of the propeller downwash with little to no forward airspeed allowing for more accurate measurements to be taken compared to most helicopters in the low-speed regime.

The radio navigation set (RADNAV) consists of a suite of radio antennas including Very High Frequency Omni-Directional Range (VOR), Distance Measuring Equipment (DME), Tactical Air Navigation (TACAN), Direction Finder (DF), and Instrument Landing System (ILS) glideslope, localizer, and marker beacons. The RADNAV suite enables flights in Instrument Meteorological Conditions (IMC) flown to minimum cloud ceilings and visibility throughout the world. Air-to-air TACAN also permits safe joinup of multiple aircraft in nighttime or moderate visibility conditions.

The transponder allows programming of military and civilian modes 1, 2, 3A/C, 4, 5, and S including incorporating with the Automatic Dependent Surveillance-Broadcast (ADS-B) in and out systems. The system also receives Flight Information System-Broadcast (FIS-B) and Traffic Information Service-Broadcast (TIS-B). FIS-B includes a subscription to a variety of live aviation weather products including Meteorological Aerodrome Reports (METARs), Terminal Area Forecasts (TAFs), winds aloft, Next Generation Weather Radar (NEXRAD) precipitation maps, and other aviation products. The crew has the capability to program or disable any of the transponder modes as required by the tactical picture. The traffic collision avoidance system (TCAS) also interfaces with the transponder to interrogate other aircraft to cue the pilot on safe maneuver areas when in close proximity to other aircraft.

All RADNAV and transponder modes use data isolation techniques in the GNC to prevent cyber threats from accessing systems or attempting takeover within the aircraft.

### 16.1.2 Landing Zone Situational Awareness, Guidance, and Evaluation

The Landing Zone Situational Awareness, Guidance, and Evaluation (LZ-SAGE) system is designed to be used in the terminal environment on prepared and unprepared surfaces to assist the crew in precisely positioning the aircraft even in the tightest of landing zones. The system is an integrated set of sensors that lie in the nose of the aircraft consisting of active LIDAR and passive IR and color cameras. On approach to the landing zone, the system builds a virtual scene of the area, aided by digital terrain elevation data (DTED) for initial acquisition. Imagery from the IR cameras on the initial approach persists on the 3D surfaces detected by the LIDAR sensors to give the operator a visual model of the aircraft in the scene, even once visibility drops due to degraded visual environments. Even in the presence of dust, sand, or fog, the obscurant penetrating LIDAR system continues to map the scene and identify obstacles as the aircraft nears the ground [47]. The mapped landing zone will also be evaluated by the system for areas that will permit a safe landing based on detected obstacles and slopes. The crew can manually fly to the



touchdown point or activate an autonomous landing to any of the recognized safe landing zones [46]. The system interfaces with the GNC to provide the guiding path to touchdown.

### 16.1.3 Cockpit Interface

The GNC interfaces with the pilot through the primary flight controls, multifunction flight displays (MFD), navigation reference displays (NRD), Flight Management Computers (FMC), and Flight Director Panel (FDP). The GNC understands the aircraft state through the navigation solution and interprets the desired flight state based on the primary flight controls and other commands issued through the MFDs and FMCs. The main instrument panel is depicted in Figure 16.2.



Figure 16.2: Cockpit Instrument Panel Overview

The GNC passes information to the various cockpit displays including aircraft attitude and heading, altitude, airspeed, groundspeed, winds, and various positional navigation information including LZ-SAGE scene depictions. The NRDs also display selected georeferenced charts or approach plates to increase situational awareness during navigation. Worldwide navigation waypoints, airport information, and local area charts can be uploaded to the aircraft on high-capacity data transfer devices for daily missions.

The FMCs are the primary data entry interface to the GNC for the pilot to input the desired route of flight. The GNC is coupled to the desired flight path using the FDP in the center portion of the cockpit instrument panel. The FDP can be used to command the GNC into programmed route mode, on-track override mode, or vector mode. Programmed Route mode follows the flight plan input to the FMC from launch to touchdown. On-track override mode flies the programmed route over the ground, but allows programming of alternate airspeed or altitude. Vector mode can be used to issue flight path commands not previously programmed into the FMC. The FMC also allows programming of inter-route delays for easy activation of holding patterns or optimized search patterns if conducting search and rescue operations.

### 16.1.4 Guidance and Control

The GNC determines the desired flight path and passes the required inputs to the Flight Control Computer (FCC). The redundant FCCs distribute the control commands to the flight control actuators throughout



the aircraft. The FCC also monitors the actuator positions and resultant aircraft state to ensure proper operation. If an actuator does not respond to a flight control input, or the aircraft response to a flight control input does not match the expected result, the FCC can secure an actuator and increase gains on redundant actuators for continued safe operation. In the event an entire control axis is lost, the FCC may activate Damage Tolerant Control laws in the GNC to overcome the loss [48]. For example, if rudder actuation is lost in forward flight, the proprotors can use differential collective and lateral cyclic to provide yaw control. Control failures in the rotor system may require rotor inputs to be locked out to neutral cyclic and collective pitch, but the aircraft may be safely recoverable with a running landing powered by the turbofan engines.

## 16.2 Communication

The communications system consists of the antennas, transmitters, receivers, and cockpit interfaces that enable voice communications on ultra-high frequency/very-high frequency radio channels (UHF/VHF), beyond-line-of-sight high frequency (HF), satellite communications (SATCOM), tactical datalinks such as Link 16 (L16), and short range, inter-aircraft mesh networks. Additional communication can be accomplished with image and text messages over L16 and inter-aircraft mesh networks. Internal communications systems also enable the crew to communicate throughout the aircraft. Modularly installed mission packages also enable airborne command and control elements to be installed in the aircraft cabin, for which there are additional antennas and radios allocated. Communication can be clear voice unencrypted or secured with military-grade, 256-bit Advanced Encryption Standard (AES-256).

## 16.3 Mission Management

The VMCs are also allocated with mission management software (MMS) that interfaces with the aircraft survivability sensors including electro-optical missile warning sets (MWS), advanced radar warning receivers (RWR), distributed aperture infrared countermeasure system (DAIRCM), and countermeasure dispensing systems (CMDS). The MWS detects point light sources characteristic of the rocket plumes of surface-to-air missiles, laser-guided munitions, or small arms fire. The RWR receives a variety of radio frequency signals and characterizes tracking and fire control radar systems that may represent a radar-based missile threat. When MWS or RWR detects a threat, the MMS smart defense system allocates countermeasures to counter the threat based on a database of specific and generic threat profiles uploaded to the aircraft. The CMDS dispenses chaff, flare, and other decoys that are designed to confuse the tracking algorithms of various known threats. The DAIRCM system provides additional advanced capabilities to defeat additional vehicle-launched and man-portable air-defense systems (MANPADS). The MMS also displays information on the threat to the crew including the threat axis, type of threat, and recommended maneuvers. Countermeasures can be set to dispense automatically, manually, or with aircrew approval depending on the threat environment and rules of engagement.

## 16.4 Health and Usage Monitoring System

*Arion* is equipped with a Health and Usage Monitoring System (HUMS) consisting of a variety of strain gauges, accelerometers, and other sensors throughout the vehicle that are monitored and recorded by the VMCs. The data from the sensors is accessible in flight by the crew for in-flight checkout and also downloadable post-flight for airframe lifecycle monitoring. The system will notify the crew real-time in flight if there is an exceedance that potentially compromises the structural integrity of the airframe requiring careful maneuvering to get home safely. During shutdown procedures, additional usage information will be displayed to the aircrew and ground maintenance crews for monitoring of the lifetime of limit cycle parts.



## 17 Manufacturing & Cost Analysis

### 17.1 Aircraft Purchase Price

*Arion's* purchase price cost was evaluated using the NDARC component parameterized model for cost estimation [10]. The high-fidelity model by Scott [49] estimates the aircraft purchase price as:

$$C_{AC} = \chi_{comp}(F_i c_{FA})$$

where  $\chi_{comp}$  is a technology factor, and  $F_i$  is an inflation factor to express the cost in 2023 U.S. dollars based on the consumer price index from the U.S. Bureau of Labor Statistics [50]. The technology factor of  $\chi_{comp} = 0.87$  accounts for calibration and industry factors for the U.S. Military [10]. The aircraft flyaway cost,  $c_{FA}$ , is based on the component level model cost estimate which estimates the unit price of the  $N_p$ -th aircraft of an  $N_q$  sized production lot [10].

For the first aircraft produced of a one aircraft lot, the aircraft purchase price is **\$116.5** million dollars; however, the average cost per aircraft for a 100 aircraft production lot is only **\$70.7** million dollars.

### 17.2 Maintenance Cost

The aircraft maintenance cost is estimated in dollars per flight hour based on a statistical relationship with aircraft flyaway cost and installed power [49]. The maintenance cost is adjusted by a technology factor and inflation to be presented in 2023 U.S. dollars as:

$$C_{maint} = \chi_{maint}(F_i c_{maint})$$

The maintenance cost is estimated to be **\$5,949** per flight hour.

### 17.3 Operational Cost

The annual operating cost,  $C_{OP}$ , is estimated based on operating expenses including maintenance and fuel expressed in cost per flight hour and manpower expressed in annual cost per aircraft. The annual operating cost is given by

$$C_{OP} = T_F(C_{maint} + C_{fuel}) + C_{MP}$$

where  $T_F$  is the annual flight hours per aircraft. The annual flight hours per aircraft assumes a quarter of the aircraft inventory will complete two RFP mission profiles on any given day equating to 456 flight hours per year per aircraft. Fuel cost is based on the 2023 Defense Logistics Agency Standard Fuel Prices [51].

The annual operating cost is estimated to be **\$4.55** million per aircraft. The cost per RFP mission is **\$24,942**. This mission cost equates to **\$9.98** per ton-nautical mile (**\$10.97/tonne-nm**) of payload for fully loaded cargo missions and **\$1.25** per troop-nautical mile for full capacity troop transport. The total life-cycle cost per aircraft including purchase price in a lot of 100 and annual operating costs over 20 years is **\$91.04** million.

## 18 Multi-Mission Capabilities

*Arion* is built for rapid insertion of cargo and troops into tight, contested zones requiring a fast aircraft with vertical landing capability, but the aircraft is also smartly equipped to accomplish a variety of other missions. Maximum range and endurance profiles as described in Section 13 can be utilized by a mission-trained crew to optimize the aircraft under a variety of conditions. At any time during the flight, the



aircraft avionics system will assist the pilot in obtaining these optimal parameters by giving recommended airspeed and altitude for maximum endurance and range. Additionally, the Vehicle Management System will balance the turbofan and turboshaft power at any steady flight condition to minimize fuel consumption. The diverse provisions enable the aircraft to adapt based on the crew's assessment of the mission. The varied capability ensures *Arion* use in a variety of wartime and peacetime missions.

## 18.1 Non-Combat Transport and Logistics

While *Arion's* configuration is built for speed, the aircraft also has the ability to extend its range capabilities. The hovering capabilities allow delivery and pickup of personnel and cargo from nearly anywhere. The long-range profiles of more than 2,500 nm (4,630 km) enable *Arion* to fly from Honolulu to Dublin with only two stops in Los Angeles and Bangor, Maine. Internally carried auxiliary fuel tanks can further increase the range, allowing the aircraft to self-deploy anywhere support is needed. The ability to carry standard palletized cargo means stopover delays will be minimized as gear can be pre-staged for quick loading. When paved runways are available, the aircraft can carry even more than the 5,000 lb (2268 kg) payload maximum for hovering takeoffs which means fewer trips and fewer aircraft will be needed to transport equipment over longer distances. While this capability can be used for basic logistics needs, the vertical landing capabilities and large cabin are ideal for humanitarian assistance and disaster relief. Similarly, medical evacuation can be accomplished with provisions for 12 litters, seating for 6 medical attendants, and power outlets for portable medical equipment. The autonomous flight modes and flight director will minimize pilot workload throughout the flight profile, minimizing fatigue and maximizing mission effectiveness, especially on long transit legs in both VMC and IMC. The well-equipped communications suite will permit commanders to make in-flight mission changes as necessary to support their forces. The navigation system's complement of internal and external navigation sources will enable crews to navigate without visual reference anywhere in the world. The onboard radar will further enhance IMC capabilities, helping crews identify severe weather areas. ADS-B and TCAS capabilities will enhance the crew's situational awareness and minimize risk of mid-air collision in densely trafficked airspace. Mission commanders will come to rely on *Arion* performance and flexibility to conduct non-combat transport missions.

## 18.2 Search and Rescue

*Arion* can also be used as a valuable asset in search and rescue (SAR) missions. When conducting searches, the long endurance profiles at moderate speeds will enable crews to cover significantly more ground than conventional SAR helicopters. The long-range capabilities also mean that *Arion* can conduct long searches farther from its home base. Programmable search and rescue patterns and automated flight will ensure every piece of land or sea is searched and allows the crew to focus more on searching than flying. The diverse sensor suite can assist the crew in their search with infrared and visual spectrum video, radar, and LIDAR, all of which can be configured to help find lost individuals or signs of aircraft wreckage. The communications suite will permit those sensors to be linked and sent live to other assets to assist the crew in monitoring multiple video feeds. Once the survivor is found, *Arion* transitions seamlessly to the rescue portion of the mission. Depending on the availability of assets, *Arion* can use its long endurance and adept communications suite to assume On-Scene Commander, or *Arion* can perform a rescue itself. Over land, the vertical landing capabilities make landing to effect a rescue the best and safest option. For overwater operations or if the terrain does not permit a landing, the rescue hoist can be lowered out of the rear cargo bay. While the disk loading is higher than most conventional helicopters at  $23 \text{ lb/ft}^2$ , *Arion* was designed with a large rotor area to minimize the amount of downwash while still being able to achieve 450 kts. Once the survivors are on board, the ample-sized cargo bay will allow trained medical personnel to be on board during rescue operations to provide first aid. If patients are non-ambulatory, provisions for up to 12 liters



are available in the cabin. While patients are stabilized, the aircraft's speed and range capability will allow transport to the most appropriate medical facility in minimum time. The vertical landing capability will again come into play when *Arion* can land directly at a Hospital, vice needing to meet an ambulance at an airfield. More lives will be saved with *Arion* conducting search and rescue operations.

### 18.3 Airborne Command and Control

*Arion* ability to fly high for long-duration missions makes it an optimal asset for airborne command and control. The cargo bay can be outfitted with modular control stations, powered by the aircraft's electrical system. The control stations can port directly into the aircraft's communication, navigation, and sensor suites to exercise complete control over the battlespace whether the focus is centered in the sea, air, or land. While the pilots fly and focus on the aircraft, highly qualified personnel can survey the environment and directly issue orders to assets over a wide geographic area with line-of-sight and over-the-horizon communications. Embarked commanders can have situational awareness of all their forces during critical situations to make the most informed decisions to optimally accomplish the mission. Even unmanned assets can be controlled to push low-cost surveillance assets further into enemy territory without additional risk to friendly forces. Battlespace decision makers will want to be on board *Arion* during essential missions for optimal command and control of their forces.

## 19 Summary

The University of Maryland Graduate Design Team designed *Arion*, a mixed-power tiltrotor capable of hover and high-speed forward flight at 450 kts. The design is enabled by optimized rotor aerodynamics and a two-speed transmission allowing the rotor to efficiently produce thrust at 450 kts. The rotor thrust is augmented by twin turbofan engines that provide the extra power needed to reach high speeds. The final vehicle meets all of the vehicle and operational requirements set forth in the Request for Proposal for a High-Speed Vertical Takeoff and Landing Aircraft for the 2023 Vertical Flight Society Design Competition. *Arion* is optimized for efficiency in both hover and forward flight to enable swift delivery of cargo and troops.

1. Variable speed proprotor with two-speed transmission allows for a 63% reduction in tip speed to achieve both excellent hover and cruise efficiencies:  $\eta_p = 0.685$  in cruise,  $FM = 0.813$  in hover.
2. Hingeless hub design prevents ground resonance and mitigates whirl flutter for high-speed flight.
3. Thin airfoil designed in-house for minimizing compressibility effects at the blade tip.
4. Large rotor diameter gives a maximum hover disk loading of  $23 \text{ lb}/\text{ft}^2$  ( $1,101 \text{ N}/\text{m}^2$ ).
5. High, fuselage-mounted engines and inlet barrier designs minimize FOD concerns in a hover.
6. Two high-bypass turbofan engines augment the thrust to reach 450 kts.
7. The cabin is reconfigurable at will to accommodate either 20 combat-loaded troops, 12 medical patients, or 5,000 lb (2,268 kg) of cargo.
8. Modern flight control laws reduce pilot workload throughout the flight envelope.
9. Advanced self-defense systems automatically detect and deploy countermeasures in high-threat environments.
10. State-of-the-art landing sensors detect obstacles through degraded visibility conditions for a safe landing.



## References

- [1] Johnson, W., Yeo, H., and C.W. Acree, J., “Performance of Advanced Heavy-Lift, High-Speed Rotorcraft Configurations,” *AHS International Forum on Rotorcraft Multidisciplinary Technology*, Seoul, Korea, October 2007.
- [2] Wilkerson, J., Schneider, J., and Bartie, K., “Technology needs for high-speed rotorcraft, volume 1,” Tech. rep., 1991.
- [3] Johnson, W., Yamauchi, G. K., and Watts, M. E., “Designs and Technology Requirements for Civil Heavy Lift Rotorcraft,” *AHS Vertical Lift Aircraft Design Conference*, San Francisco, California, January 18–20, 2005.
- [4] Maurya, S., Wang, X., and Chopra, I., “Wind Tunnel Test on a slowed Mach-Scaled Hingeless Rotor with Lift Compounding,” *Journal of the American Helicopter Society*, Vol. 66, No. 4, Oct. 2021, pp. 1–17.
- [5] Wang, X., Bauknecht, A., Maurya, S., and Chopra, I., “Slowed Hingeless Rotor Wind Tunnel Tests and Validation at High Advance Ratios,” *Journal of Aircraft*, Vol. 58, No. 1, Jan., pp. 153–166.
- [6] Maurya, S., Chopra, I., and Datta, A., “In Search of Extreme Limits of a Compound Helicopter in High Speed Flight,” *Proceedings of the Vertical Flight Society International 77th Annual Forum & Technology Display*, May 2021.
- [7] Kaplan, N., Patil, M., Chopra, I., and Datta, A., “Wind Tunnel Testing and Aeromechanics Predictions on Slowed Mach-scaled Thrust Compounding Rotorcraft with a Trailing Propeller,” *Proceedings of the Vertical Flight Society International 79th Annual Forum & Technology Display*, May 2023.
- [8] Matuska D, Dale A, L. P., “Wind Tunnel Test of a Variable-Diameter Tiltrotor (VDTR) Model,” NASA-CR 177629, 1994.
- [9] “Large Scale Wind Tunnel Investigation of a Folding Tilt Rotor,” NASA-CR NASA-CR-114464, 2015.
- [10] Johnson, W., “NDARC: NASA Design and Analysis of Rotorcraft,” NASA-TP 2015–21875, Apr. 2015.
- [11] Amri, H., Feil, R., Hajek, M., and Weigand, M., “Possibilities and difficulties for rotorcraft using variable transmission drive trains,” *CEAS Aeronaut Journal*, Vol. 7, 2016, pp. 333—344.
- [12] Roux, E., *Turbofan and Turbojet Engines Database Handbook*, Editions Elodie Roux, 2007.
- [13] Prouty, R. W., *Helicopter Performance, Stability, and Control*, Krieger Publishing Company, Inc., 1st ed., 1986.
- [14] Lewicki, D. G. and Stevens, M. A., “Testing of Two-Speed Transmission Configurations for Use in Rotorcraft,” NASA-TM 2015-218816, 2015.
- [15] Akinwale, A. and Datta, A., “High Speed Whirl Flutter Tests of the Maryland Tiltrotor Rig,” *Proceedings of the Vertical Flight Society International 79th Annual Forum & Technology Display*, May 2023.
- [16] Gul, S. and Yeo, H., “High-Speed Stability Predictions of Maryland Tiltrotor Rig and Parametric Study,” *Proceedings of the Vertical Flight Society International 79th Annual Forum & Technology Display*, May 2023.
- [17] Gul, S. and Datta, A., “Whirl Flutter Test of the Maryland Tiltrotor Rig: Prediction and Validation,” *AIAA SciTech 2022 Forum*, Jan 2022.
- [18] Harris, F., “Performance Analysis of Two Early NACA High Speed Propellers with Application to Civil tiltrotor Configurations,” NASA-CR 196702, August 1996.
- [19] Bauchau, O., “SectionBuilder Simulation Tools for Flexible Multibody Systems,” 2023.



- [20] Gul, S. and Datta, A., “Aeroelastic Loads and Stability of Swept-Tip Hingeless Tiltrotors toward High-Speed Instability-Free Cruise,” *Journal of the American Helicopter Society*, Vol. 68, No. 1, January 2023, pp. 1–18.
- [21] Gul, S. and Datta, A., “Development of an Aeromechanics Solver for Loads and Stability of Hingeless Tiltrotors,” *Journal of Aircraft*, Vol. 60, No. 1, January 2023, pp. 143–159.
- [22] The Boeing Company - Vertol Division, “V/STOL Tilt Rotor Aircraft Study - Volume II: Preliminary Design of Research Aircraft,” NASA CR 114438, 1972.
- [23] Patil, M. and Datta, A., “A Scalable Time-Parallel Solution of Periodic Rotor Dynamics in X3D,” *Journal of the American Helicopter Society*, Vol. 66, No. 4, October 2021, pp. 1–16.
- [24] Gaffey, T. M. and Wernicke, K. G., “In-Plane Out-of-Plane Flapping Prop-rotor Frequency Decoupling,” U.S. Patent 3,494,706, Feb. 10, 1970.
- [25] Maisel, M. D., Giulianetti, D. J., and Dugan, D. C., “The History of the XV-15 Tilt Rotor Research Aircraft: From Concept to Flight,” NASA SP- 2000-4517, 2000.
- [26] Glauert, H., “Theoretical Relationships for an Aerofoil with Hinged Flap,” ARC R and M no. 1095, Aeronautical Research Committee, April 1927.
- [27] Chappell, D. P., “2107. Methodology for Estimating Wing Weights for Conceptual Tilt-Rotor and Tilt-Wing Aircraft,” *51st Annual Conference, Hartford, Connecticut, May 18-20*, Society of Allied Weight Engineers, Inc., Society of Allied Weight Engineers, Inc., Hartford, Connecticut, 5/18/92 1992, p. 32.
- [28] Kassapoglou, C., *Design and Analysis of Composite Structures: With Applications to Aerospace Structures*, Aerospace Series, Wiley, 2011.
- [29] Rhodes, M. D. and Mikulas Jr, M., “Composite lattice structure,” Tech. rep., 1975.
- [30] Raymer, D. P., *Aircraft Design: A Conceptual Approach*, AIAA Education Series, AIAA, 3rd ed., 1999.
- [31] Amri, H., Feil, R., Hajek, M., and Weigand, M., “Possibilities and Difficulties for Rotorcraft using Variable Transmission Drive Trains,” *CEAS Aeronautical Journal*, Vol. 7, No. 2, March 2016, pp. 333–344.
- [32] Moore, R. E., “Helicopter Rotor Transmission Systems - US Patent 4,632,337,” 1986.
- [33] Karem Aircraft, “Rotorcraft Engine and Rotor Speed Synchronization - WO2009111705A1,” 2009.
- [34] Stevens, M. A., Lewicki, D. G., and Handschuh, R. F., “Concepts for Multi-Speed Rotorcraft Drive System - Status of Design and Testing at NASA GRC,” NASA-CP GRC-E-DAA-TN20879, 2015.
- [35] Okura, T., “Materials for Aircraft Engines,” ASEN 5063 Aircraft Propulsion Final Report, University of Colorado Boulder, Dec 17, 2015.
- [36] Parmanen, J., “A-weighted sound pressure level as a loudness/annoyance indicator for environmental sounds—Could it be improved?” *Applied Acoustics*, Vol. 68, No. 1, 2007, pp. 58–70.
- [37] El-Sayed, A., *Fundamentals of Aircraft and Rocket Propulsion*, Springer.
- [38] Jude, D., Lee, B., Jung, Y. S., Petermann, J., Govindarajan, B., and Baeder, J., “Application of a Heterogeneous CFD Framework Towards Simulating Complete Rotorcraft Configurations,” *American Helicopter Society, 74th Annual Forum Proceedings, Phoenix, Arizona, May 14-17, 2018*.
- [39] Chang, P. K., “Chapter XII - Control of Separation of Flow,” *Separation of Flow*, Pergamon Press, 1970, pp. 716–752.
- [40] Hoerner, S., *Fluid-Dynamic Drag*, Vol. 2, Sighard F. Hoerner, 1958.



- [41] Anderson, J., *Fundamentals of Aerodynamics*, McGraw-Hill series in aeronautical and aerospace engineering, McGraw-Hill Education, 2017.
- [42] McCroskey, W. J., Spalart, P. R., Laub, G. H., Maisel, M. D., and Maskew, B., “Airloads on Bluff Bodies, with Application to the Rotor-Induced Downloads on Tilt-Rotor Aircraft,” NASA-TM 84401, Sept. 1983.
- [43] Potsdam, M. and Silva, M., “Tilt Rotor Aeromechanics Phenomena in Low Speed Flight,” 07 2004, pp. 151–157.
- [44] “Handling Qualities Requirements for Military Rotorcraft, ADS-33E-PRF,” U.S. Army Aviation and Missile Command, Mar 21, 2000.
- [45] Nadell, S., Berger, T., DiJoseph, A., Huang, E., “Development, Simulation, and Flight Testing of Damage Tolerant Control Laws for the ADAPT<sup>TM</sup> Winged Compound Helicopter Scaled Demonstrator,” May 16–18, 2023.
- [46] Alexander, M., Borschchova, I., Carrothers, B., Comeau, P., Craig, G., Ellis, K., Gowanlock, D., Gubbels, A., “Landing Phase Analysis of the NRC Bell 412 Advanced Systems Research Aircraft in Supervised-Autonomous Flight Systems Configuration,” *79th Vertical Flight Society Annual Forum*, West Palm Beach, FL, May 16–18, 2023.
- [47] Trickey, E., Church, P., and Cao, X., “Characterization of the OPAL obscurant penetrating LiDar in various degraded visual environments,” Proc. SPIE 8738, Degraded Visual Environments: Enhanced, Synthetic, and External Vision Solutions 2013, 87370E, May 16 2013.
- [48] Berger, T., Gong, A., Horn, J., Bridges, D., Hagwood, D.G., Kuhn, N., “Piloted Simulation Evaluation of Damage Tolerant Control for a Coaxial Compound Helicopter,” *79th Vertical Flight Society Annual Forum*, West Palm Beach, FL, May 16–18, 2023.
- [49] Scott, R., Vegh, J.M., “Progress Toward a New Conceptual Assessment Tool for Aircraft Cost,” *76th Vertical Flight Society Annual Forum*, Virtual, Virginia, Oct 6–8, 2020.
- [50] “Consumer Price Index,” U.S. Department of Labor, Bureau of Labor Statistics, 2023. All Urban Consumers (CPI-U), U.S. city average, All items.
- [51] “Fiscal Year (FY) 2023 Standard Fuel Price Change,” Memorandum from the Under Secretary of Defense for Acquisition and Sustainment, Jan 25, 2023.

